Experimental Investigation of the Interaction between Purge and Main Annulus Flow upstream of a Guide Vane in a Low Pressure Turbine

Dissertation

Dipl.-Ing. Sebastian Schrewe

Fachgebiet Gasturbinen, Luft- und Raumfahrtantriebe
Technische Universität Darmstadt

Darmstadt, 2015

TECHNISCHE UNIVERSITÄT DARMSTADT

Experimental Investigation of the Interaction between Purge and Main Annulus Flow upstream of a Guide Vane in a Low Pressure Turbine

Am Fachbereich Maschinenbau
der Technischen Universität Darmstadt
zur
Erlangung des Grades eines Doktor-Ingenieurs (Dr.-Ing.)
genehmigte

D i s s e r t a t i o n

vorgelegt von

Dipl.-Ing. Sebastian Schrewe

aus Henstedt-Ulzburg

Berichterstatter:	Prof. Dr.-Ing. Heinz-Peter Schiffer
Mitberichterstatter:	Prof. Dr.-Ing. Hans-Jörg Bauer
Tag der Einreichung:	27. Januar 2014
Tag der mündlichen Prüfung:	23. April 2014

Darmstadt 2015
D 17

Acknowledgement

First of all, I would like to express my gratitude to my advisor Prof. Dr.-Ing. H.-P. Schiffer, head of the Institute of Gasturbines and Aerospace Propulsion at Technische Universität Darmstadt. He gave me the opportunity to work in an intercultural team during the EU project MAGPI. This project has given me the opportunity to work independently, take my own decisions and manage my own project, which has helped me to develop invaluable skills for the future.
In addition, I would like to thank Prof. Dr.-Ing. H.-J. Bauer from Karlsruhe Institute of Technology for the co-review of this thesis.
I also acknowledge the financial support by the European Commission within the Framework 6 Programme Research Project (MAGPI), AST5-CT-2006-030874 and the support of the industrial partners during this project.
Furthermore, I would like to thank all colleagues at the Institute of Gasturbines and Aerospace Propulsion for the help and guidance during technical discussions which contributed to this thesis. However, also the good athmosphere and many personal conversations assisted in the same extent to this work. Special thanks goes to all colleagues who supported me during rig operation and preparation. For the review of my thesis I thank Mr. Schmid, Mr. Rakenius and Mr. Werschnik. From these Mr. Schmid deserves further thanks for the numerical simulations which contributed to the general understanding of many flow phenomena.
Also I would like to thank Mr. Nolde and the whole team of the institute's machine shop. Without their support the operation of the LSTR would have been impossible. Similarly I thank Mrs. Wißmann and Mrs. Löhr for the administrative support.
Further gratitude belongs to all the students who supported this work during their time at the Institute. Without all their assistance during the preparation, accomplishment and the evaluation of the measurements, this thesis would have surely not been possible in this extent.
The most gratitude however goes to my girlfriend Dana. During the last five years she frequently had to subordinate her personal interests. Nevertheless, she always supported and encouraged me. Likewise I wish to thank my mother Eva and my grandparents Margarethe and Alfred. Without their support and patience during school, university and finally the work as a research assistant this thesis would never have been possible.

Abstract

In modern gas turbines or jet engines, the ingestion of hot gas through the hub-side gap between rotor and stator blades has to be prevented successfully in order to shield the turbine discs from high temperatures. For this purpose, compressor air is fed into the rotor-stator wheelspace. There it purges and hence seals the unavoidable gap between the rotor and the stator row which is referred to as the rim seal.

In general, this so-called purge flow has detrimental effects. On the one hand, it does not fully contribute to the thermodynamic cycle of the engine. On the other hand, it spoils the main flow aerodynamics when it re-enters into the turbine. To reduce these detrimental effects and minimise the necessary amount of purge flow, a detailed understanding of the interaction between purge and main annulus flow is necessary. For this purpose, this topic has been investigated by several projects.

Whereas in most of these projects the interaction between purge and main annulus flow has been investigated upstream of a rotor row in a high pressure turbine, in this thesis the purge flow injection upstream of the stator row of a low pressure turbine is examined. This aims to broaden the general understanding of the interaction between purge and main annulus flow. Furthermore, a comparison of the effects upstream of a rotor row and upstream of a stator row is carried out.

For this investigation numerous experiments have been conducted during the EU Project MAGPI using the Large Scale Turbine Rig (LSTR) at Technische Universität Darmstadt. This test rig is equipped with different measurement techniques, including pressure taps, 5-hole probes, PIV and a tracer gas system. In their combination these measurement techniques offer the possibility to study the purge flow induced effects in great detail.

The measurements reveal a significant influence of purge flow on the flow field within the main annulus and the rim seal. With increasing purge flow, a negative incidence develops at the stator row. This increases the crossflow within the passage and amplifies secondary flows. In addition to this amplification of secondary flows, which is generally similar to results observed for purge flow injection upstream of a rotor row, a significant influence of the purge flow delivery is observed. Especially in low pressure turbines, the purge flow is often supplied through discrete holes in the rotor drum. At sufficiently high pressure ratios, the purge flow may leave these

holes in the form of discrete jets. These so-called drive arm hole jets are examined to influence the flow field in the rim seal significantly in the current configuration. That is, they form a purge flow filled vortex in the rim seal, which suppresses the typical flow structure. In addition, these jets promote hot gas ingestion.
Overall, the method of the purge flow delivery is assessed to play a significant role on the effects caused by purge flow injection. Furthermore, the flow field measurements yield a detailed insight into the interaction between purge and main annulus flow.
Based on the results examined in this thesis, two different design proposals have been elaborated, which aim to reduce losses and hence increased the efficiency of the turbine.

Kurzzusammenfassung

In modernen Gasturbinen oder Flugzeugtriebwerken muss das Eintreten von heißen Gasen durch den nabenseitigen Spalt zwischen Rotorschaufeln und Statorschaufeln vermieden werden. Andernfalls kann es zu einer thermischen Überlastung der hochbelasteten Rotorscheiben kommen. Aus diesem Grund wird am Verdichter entnommene Luft durch diesen unvermeidbaren Spalt geblasen, um ihn gegenüber den heißen Gase abzusperren.
Diese sogenannte Sperrluft hat in der Regel nachteilige Effekte. Zum einen nimmt sie nicht vollständig am Kreisprozess teil. Zum anderen verändert sie die Aerodynamik der Turbine und führt in den meisten Fällen zu erhöhten Strömungsverlusten. Um diese Verluste zu reduzieren und den benötigten Sperrluftmassenstrom zu verringern, ist ein umfassendes Verständnis über die Interaktion zwischen Hauptstrom und Sperrluftstrom unvermeidbar. Aus diesem Grund wurden in den letzten Jahren zahlreiche Forschungsprojekte zu diesem Thema durchgeführt.
Während sich der Großteil dieser Untersuchungen auf die Sperrluftausblasung stromauf der Rotorreihe einer Hochdruckturbine konzentriert, wird in der vorliegenden Arbeit die Sperrluftausblasung stromauf der Statorreihe einer Niederdruckturbine experimentell untersucht. Dies erweitert zum einen das generelle Verständnis über die Sperrluft - Hauptstrom Interaktion. Zum anderen können die Effekte stromauf einer Statorreihe mit denen stromauf einer Rotorreihe verglichen werden.
Zu diesem Zweck wurden im Rahmen des EU Projektes MAGPI zahlreiche Versuche am „Large Scale Turbine Rig" (LSTR) der Technischen Universität Darmstadt durchgeführt. Dieser Prüfstand ist mit unterschiedlicher Messtechnik, wie statischen Druckmessstellen, Fünflochsonden, einem PIV System und einem Tracergas Messsystem ausgestattet. Dabei erlaubt besonders die Kombination dieser verschiedenen Messtechniken, die Sperrluft - Hauptstrom Interaktion im Detail zu untersuchen.
Die durchgeführten Messungen zeigen einen deutlichen Einfluss der Sperrluft auf die Turbinen- und die Radseitenraumströmung auf. Mit steigendem Sperrluftmassenstrom kommt es zu einer ausgeprägten Fehlanströmung der Statorschaufeln. Hierdurch wird die Querströmung in der Passage und damit die Ausbildung von Sekundärströmungen angefacht. Zusätzlich zu dieser Verstärkung der Sekundärströmungen, welche in ähnlicher Weise auch bei der Sperrluftausblasung stromauf

einer Rotorreihe auftritt, wurde ein deutlicher Einfluss durch die spezielle Art der Sperrluftzuführung festgestellt. So wird die Sperrluft in Niederdruckturbinen oft durch einzelne Bohrungen in der Rotortrommel zugeführt. Bei einem genügend hohen Druckverhältnis über diese Bohrungen tritt die Sperrluft in Form von diskreten Strahlen in den Radseitenraum ein. Diese sogenannten „Drive Arm Hole Jet" beeinflussen in der aktuellen Konfiguration die Strömung in der Radseitenraumdichtung. So bildet sich durch die Drive Arm Hole Jets ein diskreter Wirbel aus, der die Sperrluft in Umfangsrichtung durch die Radseitenraumdichtung transportiert und das generelle Strömungsfeld in dieser verändert. Des Weiteren begünstigen die Drive Arm Hole Jets den Heisgaseintritt. Zusammenfassend wurde festgestellt, dass die Art und Weise der Sperrlufteinbringung einen deutlichen Einfluss auf die Auswirkung der Sperrluft hat. Zusätzlich bieten die Ergebnisse der Strömungsfeldvermessungen einen detaillierten Einblick in die Sperrluft - Hauptstrom Interaktion.
Auf Grundlage der gewonnenen Erkenntnisse wurden schließlich zwei Vorschläge erarbeitet, die das Ziel verfolgen, Verluste durch die Sperrluft zu reduzieren und damit den Turbinenwirkungsgrad zu erhöhen.

Contents

Nomenclature

Symbols

A	m^2	Cross sectional area at MP01
C_x	m	Axial chord length
C_d	-	Discharge coefficient
C_p	-	Profile pressure coefficient
C_w	-	Non dimensional coolant flow; $\frac{\dot{m}_{coolant}}{r_0 \mu}$
G	-	Gap ratio; $\frac{s}{r_0}$
$G_{c,ax}$	-	Axial shroud clearance ratio; $\frac{s_{c,ax}}{r_0}$
$G_{c,rad}$	-	Radial shroud clearance ratio; $\frac{s_{c,rad}}{r_0}$
IR	-	Injection rate; $\frac{\dot{m}_{PF}}{\dot{m}_{MF}}$
J_e	-	Effective velocity ratio
J	-	Velocity ratio
K	-	Empirical constant
M	Nm	Torque
Ma	-	Mach number
P_{max}	-	Non dimensional pressure variation; $\frac{\rho \Delta p_{max} r_0^2}{\mu^2}$
Pr_t	-	Turbulent Prandtl Number
R	$J/kg\,K$	Gas Constant
Re_{MF}	-	Reynolds number of main annulus flow
$Re\Phi$	-	Rotational Reynolds number; $\frac{\rho \omega r_0^2}{\mu}$
Sc_t	-	Turbulent Schmidt Number
T	K	Temperature
U	m/s	Rotor rotational velocity
V	m/s	Velocity in absolute frame of reference
V'	m/s	RMS averaged fluctuation of the velocity around its mean value
W	m/s	Velocity in relative frame of reference
a	m/s	Sonic velocity
b	m	Inner radius of rotor or stator platform

c_p	$^{N\,m}/_{kg\,K}$	Specific heat
h	m	Height of main annulus
h	$^{N\,m}/_{kg}$	Enthalpy
i	-	Index for different purge flow entries
k_p	-	Platform pressure coefficient; $\frac{p-p_{av,1-8}}{q}$
$\dot{m}$	$^{kg}/_{s}$	Massflow
p	Pa	Pressure
q	Pa	Dynamic head at rotor hub velocity; $\frac{\rho\omega^2 r_{Hub}^2}{2}$
r	m	Radius
s	m	Wheelspace width
$s_{c,ax}$	m	Axial clearance of rim seal
$s_{c,rad}$	m	Radial clearance of rim seal
$s_{overlap}$	m	Axial overlap of rotor- and stator platform
x	-	Coordinate parallel to turbine axis
y	ppm	CO_2 concentration

Greek

Δp_{max}	Pa	Annulus pressure variation in circumferential direction
Δs	$^{J}/_{K}$	Entropy generation
α	°	Yaw angle
γ	°	Radial angle
γ	-	Ratio of specific heats
η_{aw}	-	Adiabatic cooling effectiveness
η_{CO_2}	-	CO_2 mixing concentration in main annulus
η_{is}	-	Isentropic turbine efficiency
η_{MAGPI}	-	Turbine efficiency definition used in MAGPI project
η_s	-	Sealing effectiveness
μ	$^{kg}/_{m\,s}$	Viscosity
ρ	$^{kg}/_{m^3}$	Density
σ	°	Angle between two mixed flow streams
ω	$^{1}/_{s}$	Angular velocity
ζ	-	Pressure loss coefficient

Subscripts

A	At point A
DA	Drive Arm
DP	Design Point
MF	Main flow
PF	Purge flow
WS	Value of the wheelspace
$bearing$	Value of turbine main bearing
$coolant$	Coolant flow
dyn	Dynamic quantity
ex	Value at exit plane
hub	At hub position
in	Value at inlet plane
jet	Value of the drive arm hole jet
min	Minimum necessary value to prevent ingestion
$measured$	Measured value
r	In radial direction
red	Reduced value
$shaft$	Value of turbine shaft
$suction$	velocity fluid is drawn into a pressure tap with
t	Total quantity
x	In axial direction
$x\theta$	In axial-circumferential direction
0	At outer disc position
θ	In circumferential direction
∞	Value of free stream conditions

Abbreviations

CCD	Charged Coupled Device
CFD	Computational Fluid Dynamics
CO_2	Carbon Dioxide
DP	Design Point
HPT	High Pressure Turbine
IATA	International Air Transport Association

ITP	Industria de Turbo Propulsores
LDA	Laser Doppler Anemometry
LE	Leading edge
LPT	Low Pressure Turbine
LSTR	Large Scale Turbine Rig
MAGPI	Main Annulus Gas Path Interactions
MP	Measurement plane
NGV	Nozzle Guide Vane
OP	Operating point of turbine
ODP	Off Design Point
PIV	Particle Image Velocimetry
PS	Pressure side
PS	Power Split Factor
RMS	Root Mean Square
R1, R2	Rotor row 1, Rotor row 2
SPAN	Rolls-Royce flow network solver
SS	Suction side
S1, S2	Stator row 1, Stator row 2
TE	Trailing Edge
WS	Wheelspace
5HP	Five-hole-probe
abs	Absolute frame of reference
ppm	parts per million
rel	Relative frame of reference

List of Figures

List of Tables

1 Introduction

From time immemorial, the human being has been fascinated by the possibility of flying. Outstanding pioneers such as Otto von Lilienthal with his gliders or Hans Joachim Pabst von Ohain with the invention of the jet engine helped to make this dream come true. Nowadays flying is a common mode of transportation and used by billions of passengers every year. However, whereas the aviation industry has established ever faster and further flying aircraft in its first years, the requirements have changed in the last decades: Today the demand for reliable, environmentally friendly, cost effective and quiet aircraft is greater than ever before.

The reason for this is on the one hand a continuous rise of the oil price in the last decades, which directly influences the airline operating costs. As today one third of these costs are spent on fuel and oil [35], there is a steady strive to reduce fuel consumption and rise the profitability of an airline. On the other hand, the global air traffic has doubled within the last 15 years and is expected to double again within the next 15 years according to a market forecast provided by Airbus [1]. To balance or at least limit the environmental impact of this rise in air traffic, more stringent emission standards have been introduced within the last decades. In conjunction with the steady strive for competitive products, these regulations have pushed the aviation industry forward to develop more economic and environmentally friendly aircraft. As a result of this, today aircraft consume 70% less fuel and are 75% quieter compared to the ones manufactured in the 1960s (see IATA [34]).

One main contributor for this improvement has been the development of more efficient jet engines. For this purpose engines with large bypass ratios, optimised components and new combustion technologies have been developed. Furthermore, the thermodynamic cycle of the engine has been optimised, leading to elevated compressor pressure ratios and increased turbine inlet temperatures. This has lead to turbine inlet temperatures that are beyond the melting point of the materials employed. For this reason, sophisticated cooling techniques for blades, vanes and endwalls are essential and have been established within the last decades of gas turbine development. In addition, the ingestion of hot gas through the hub-side gap between the rotor and stator rows into the machine's interior has to be prevented or at least reduced to a tolerable minimum. This is necessary since this so-called hot

gas ingestion can cause serious failures such as an overheating of the heavily loaded turbine discs, which in the worst case scenario might destroy the whole engine.

A turbine section with the unavoidable gaps between the rotor and stator rows is illustrated in Fig.1.1. In addition to the main annulus, which consists of the rotating rotor and the non-rotating stator rows, the so-called rotor-stator wheelspace is shown in this figure. This is the region underneath the blade platforms, which is enclosed by rotor discs and stationary parts beneath the stator vane that support the outer liner of the interstage seal. These interstage seals connect different wheelspaces and are necessary to reduce the flow that bypasses the main annulus underneath the stator. The gap region between the rotor and stator platform is referred to as rim seal and separates the wheelspace from the main annulus. Due to an axial and radial movement of the rotating and stationary components during engine operations, this rim seal has to ensure a sufficient clearance. This in turn allows hot gas ingestion to occur.

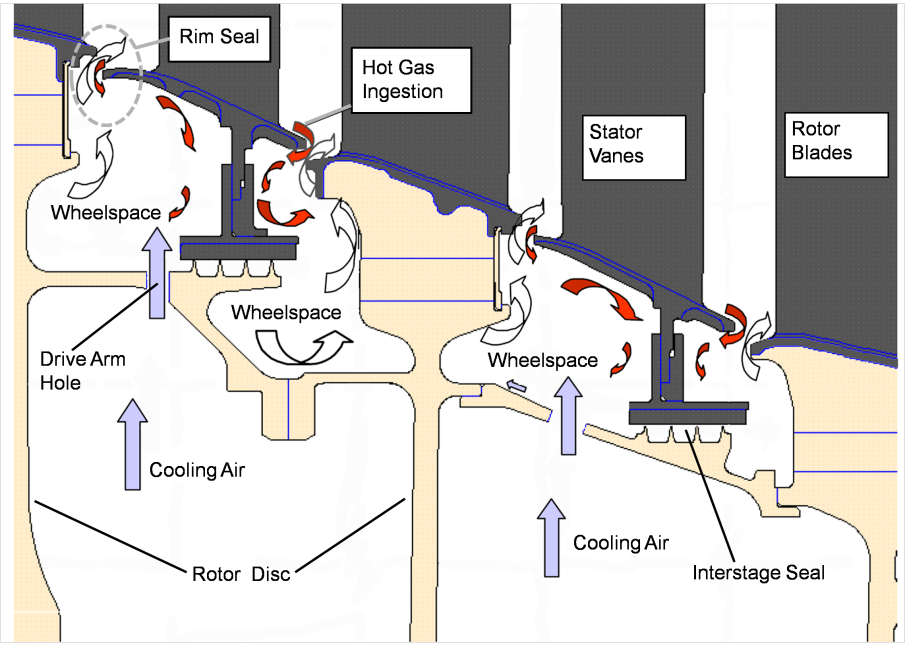

Figure 1.1: *Illustration of a rotor-stator wheelspace with adjacent blades; adapted from Dixon et al. [20]*

To prevent hot gas ingestion, which is illustrated in Fig. 1.1 by the red arrows, compressor bleed air is fed into the wheelspace in order to seal the gap between the rotor and the stator platform. In general, this so-called purge flow has detrimental effects. On the one hand, the "costly", because already compressed air bypasses the combustion chamber and does not fully contribute to the thermodynamic cycle of the engine. On the other hand, the purge flow interacts with the main annulus flow when it re-enters the turbine. This alters the boundary layer and flow field in the main annulus and usually leads to increased losses. For these reasons a reduction of purge flow is desired. For instance, Johnson et al. [42] state that a reduction of purge flow by 50% leads to an increase of the turbine efficiency by 0.5% and a reduction in specific fuel consumption by 0.9% (for a two stage turbine from the 1990s). However, even though a reduction of purge flow is always desired, in general there is a limit as the purge flow is also used to cool the rotor discs.

In order to reduce the necessary purge flow and its negative effects on the main flow aerodynamics, a thorough understanding of the flow mechanisms in the rotor-stator wheelspace, the rim seal and the main annulus is essential. In addition, it is important to understand the interaction between purge and main annulus flow, since it allows engineers to account for the purge flow injection during the design process of turbines. This in turn may lead to optimised turbine designs. For this reason, numerous investigations on the purge flow injection have been conducted in the last decades. A detailed literature review on this topic is provided in Chapter 2.2 of this thesis and reveals several effects, which are induced by the purge flow injection. However, while some effects are well explained, others still need further attention to gather additional information. For instance, most of the research focuses on configurations where the purge flow enters upstream of a rotor row. Only a few investigations have dealt with purge flow injection upstream of a stator row. To evaluate whether there is any difference between the purge flow injection upstream of a rotor and upstream of a stator row, the latter case should be examined in detail and compared with the first one. This has been done and is one part of this thesis.

In addition, there is little knowledge how the exact delivery of the purge flow influences the interaction between purge and main annulus flow. This is in particular the case for low pressure turbines, where the purge flow is often fed into the wheelspace through so-called drive arm holes that are located in the rotor drum (see Fig. 1.1). If the coolant flow is supplied with a sufficient high pressure difference across these holes, it leaves them in the form of discrete jets, as shown e.g. by Andreini et al. [2]. These drive arm hole jets are expected to have an influence on the interaction between purge and main annulus flow. For this reason, a configuration

in which the purge flow is delivered through discrete drive arm holes should be investigated to assess the potential effects of these drive arm hole jets. This has been done in the current thesis and forms the second part of this work.
To study the topics mentioned above and broaden the general understanding of the interaction between purge and main annulus flow, detailed flow field measurements have been conducted at the "**L**arge **S**cale **T**urbine **R**ig" (LSTR), which is an upscaled two stage research turbine set up at TU Darmstadt. Several different measurement techniques have been employed and provide in their combination a unique insight into the flow field that occurs within the main annulus and the rim seal. This experimental work has primarily been carried out within the European Commission founded project "**M**ain **A**nnulus **G**as **P**ath **I**nteractions" (MAGPI). This project was conducted between 2006 and 2011 and incorporated nine industrial partners and six university partners. Detailed information about this project can be found in Klingsporn [50], [49], Linker [55] and the MAGPI work contract [24]. In accordance to this work contract the project goals can be summarised as follows:

- A reduction of coolant and purge flow rates
- A general broadening of knowledge on the interaction between purge and main annulus flow and its effect on cavity heat transfer, spoiling and performance
- An improvement of turbine and compressor efficiency
- The generation of experimental results for the validation of numerical tools
- The creation of optimised design methods and CFD best practice guidelines
- A reduction of CO_2 emission and specific fuel consumption of up to 2%

In total four different technical work packages have been formed in this project which studied different topics. The results presented in this thesis are contributing to the second work package "Spoiling Effects of Sealing Flows on Turbine Performance".

1.1 Purpose and Motivation of this Thesis

The main purpose of this work can be summarised as:

- A broadening of the knowledge of the interaction between purge and main annulus flow

In particular, the following two questions are addressed:

- Are there general differences between purge flow injection upstream of a rotor row and upstream of a stator row?
- How does the purge flow delivery through discrete drive arm holes influence the interaction between purge and main annulus flow?

To answer these questions, detailed numerical or experimental data, which accounts for the purge flow injection, is essential. However, the availability of these detailed flow field measurements in the main annulus and especially in the rim seal region is restricted in the open literature. Thus, another purpose of this thesis is:

- To provide detailed experimental data in the main annulus and the rim seal at different purge flow rates in order to gather a better insight into the related flow mechanisms.

This experimental data can also be used for CFD validation as it was extensively done during the MAGPI project by the industrial partners of this project. As it has been shown by Zhou et al. [112] or Wang et al. [109], this validation is still necessary, since actual CFD models using periodic sectors are often inaccurate in the prediction of hot gas ingestion rates.

In relation to the presentation of experimental data, another ambition during the preparation of this work has been:

- The implementation and establishment of new measurement techniques at the LSTR.

This was necessary to obtain the requested experimental data and prepares the test rig for future research. The newly implemented PIV and gas concentration measurement system in particular play a significant role for future measurement campaigns. Even though not shown in this thesis, it was also desired to gather a comprehensive experience with the operation of the newly set up LSTR during the two years lasting measurement campaign.

Finally, the obtained results should be used to:

- Propose new design concepts for turbines with purge flow injection, offering advantages compared to the baseline design investigated in this thesis.

2 Theoretical Background and Literature Review

This chapter reviews the open literature on the following two topics:

- Secondary flows and loss mechanisms in turbomachines
- Purge flow injection between rotor and stator rows

This aims to provide a general summary of topics this thesis is based on. Afterwards, subjects that have not been studied in the open literature so far, are summarised to identify further research potential.

2.1 Secondary Flows and Loss Mechanisms in Turbomachines

In axial turbines losses occur due to viscous and pressure-induced effects. These losses can be separated into friction losses, secondary flow losses, gap losses, shock losses and cooling losses (see Henecke and Wörrlein [33]). According to Thole [106], the secondary flows in the first stage vanes of a modern turbine contribute to more than 30% of the total pressure loss through a turbine stage. Because of this significant influence on overall losses, secondary flows have been of major interest within the last decades of gas turbine development. A commonly used model of secondary flows in a linear cascade has been presented by Wang et al. [110] and is shown in Fig. 2.1. The development of individual vortices from this model is explained below. For more information the interested reader is referred to Sieverding [103], Langston [52] and Thaler et al. [105].

Horseshoe Vortex:
The horseshoe vortex develops ahead of the leading edge of the blade or vane. At this position the flow decelerates, leading in conjunction with the boundary layer at the endwall to a radial gradient in stagnation pressure. Due to this radial pressure gradient, the flow is deflected towards the endwall and a vortex develops, which is first oriented normal to a meridional plane. Caused by the existence of the blade, this vortex is split into two separate vortices, which are referred to as the suction side leg and the pressure side leg of the horseshoe vortex.

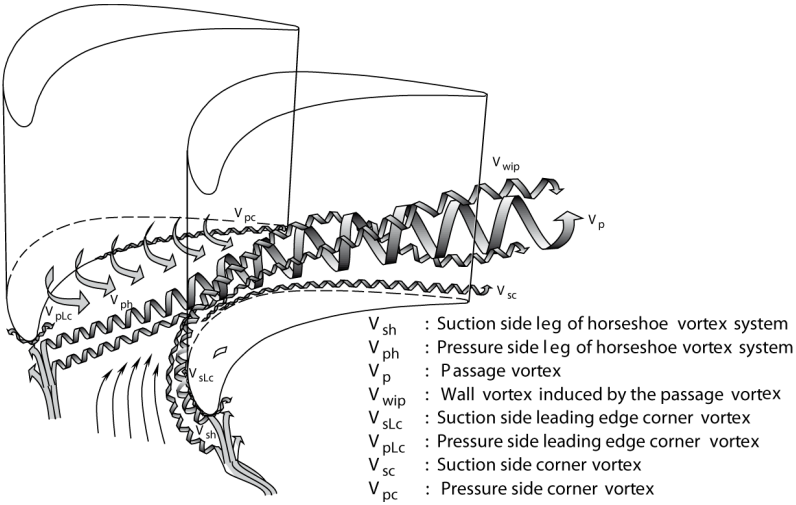

Figure 2.1: *Secondary flows in a linear turbine cascade; adapted from Wang et al. [110]*

Passage Vortex:
In the rotor or stator passage of a turbine the flow is turned. Due to the turning, a centrifugal force acts on the flow. In the main flow this centrifugal force is counteracted by the pressure gradient between the pressure and the suction side. However, approaching the endwalls, this centrifugal force disappears due to the boundary layer. The pressure gradient in contrast is still present. This leads to a crossflow of fluid at the endwall from the pressure to the suction side and drives the pressure side leg of the horseshoe vortex towards the suction side of the neighbouring blade. At the merging point of the pressure side leg of the horseshoe vortex and the suction side of the neighbouring blade, the vortex is lifted off from the endwall and called the passage vortex. It consists of the pressure side leg of the horseshoe vortex and an entrained part of the inlet boundary layer. According to the model presented by Wang, the suction side leg of the horseshoe vortex is turning slowly around the passage vortex.

Corner Vortex:
The corner vortices are found at the junction of the blade-profile and the endwalls. These are induced by the secondary flows described above. Due to the crossflow at the endwall, fluid moves from the pressure to the suction side. Similar to the horseshoe vortex, a new vortex develops when the crossflow hits the suction side

and creates a pressure gradient normal to the endwall. This vortex is referred to as the suction side corner vortex. The pressure side corner vortex originates due to the down-washed fluid at the pressure side, which hits the hub side endwall.

Trailing Edge Vortex:
The trailing edge vortex originates downstream of the blade row and is mainly driven by the existence of the passage vortices. On the suction side of the blades, the fluid moves towards midspan whereas it moves towards the hubside endwall at the pressure side. This causes a shear layer downstream of the blades, leading to the development of the trailing edge vortex. This vortex counterrotates to the passage vortex and is not presented in the model of Wang et al. in Fig. 2.1, but a suitable model is provided by Kawai et al. [46].

In addition to the described vortices, another group of vortices develops at the tip of a shroudless rotor blade. They are mainly caused by the pressure driven flow through the gap between the rotor blades and the casing. However, since they are not relevant for the present study, they are not described here.

2.2 Purge Flow Injection between Rotor and Stator Rows

On the topic of hub side purge flow injection in axial turbines, numerous research has been conducted within the last 40 years. To provide an insight into this topic, a summary of the research activities and their key findings is provided in the following chapters. For the sake of clarity, the research is divided into three different thematic areas, which are presented below.

2.2.1 Rotor-Stator Wheelspace Flow and Hot Gas Ingestion

To assess the basic flow field within a rotor-stator wheelspace, several research teams initially have studied simplified generic models. These models usually consist of a rotating disc, a stationary disc and a shroud or rim seal geometry (see Fig. 2.2). The first studies on such configurations neglect the main annulus flow (e.g. Bayley and Owen [4], Phadke and Owen [74],[75] or Chew et al. [13]), but lend themselves well to illustrate the flow field within a rotor-stator wheelspace. In addition, they are useful to investigate some fundamentals of hot gas ingestion.
Caused by friction at the rotating walls (rotor discs), fluid is accelerated within the boundary layer in circumferential direction and in turn is centrifuged radially

outwards (see e.g. Geis [28]). This is referred to as “disc pumping effect” and leads to a radial outflow of fluid at the rotor disc, which can expel fluid through the gap between the rotor and stator platform. In addition, a radial pressure gradient develops within the wheelspace, featuring a decreasing pressure radially inwards. Now, if more fluid is expelled through the gap between the rotor- and stator platform than coolant flow is delivered into the wheelspace, main annulus fluid is ingested at the stationary walls due to the negative pressure gradient and in order to preserve the conservation of mass. This kind of hot gas ingestion is referred to as “Rotationally Induced Ingress” in the literature (see e.g. Owen [64]) and is dominating at low pressure fluctuations or low Reynolds numbers in the main annulus. Figure 2.2 a illustrates the simplified flow field within a rotor-stator wheelspace for the case where hot gas ingestion occurs. A comprehensive overview on the flow field within rotor-stator systems and the corresponding describing equations is given in Owen and Rogers [66].

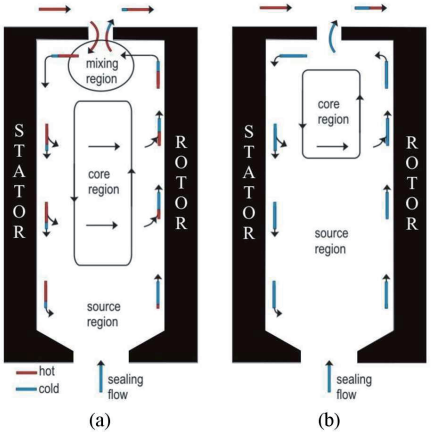

Figure 2.2: *Simplified illustration of the flow field within a rotor-stator wheelspace; according to Sangan et al. [94].*

Depending on the supplied coolant flow, hot gas ingestion can be reduced or even fully prevented. This leads to the flow field illustrated in Fig. 2.2 b, which still features outflow at the rotor disc and inflow at the stator wall. The delivered coolant flow is commonly specified in form of a nondimensional C_w value in the literature. In this case the coolant mass flow is nondimensionalised by the outer radius of the rotor disc r_0 and the dynamic viscosity of the fluid μ.

$$C_w = \frac{\dot{m}_{coolant}}{r_0 \mu} \tag{2.1}$$

Since the delivered coolant flow purges the rim seal, it is most often referred to as purge flow, but sometimes it is also called seal air as it seals the rim seal.

To determine hot gas ingestion experimentally, flow visualisation techniques using smoke are applied by Phadke and Owen [74], [75], [76], [77]. Furthermore, gas concentration measurements have become increasingly popular and have been applied by e.g. Daniels et al. [17], Feiereisen et al. [25], Lefrancois et al. [53], Zhou et al. [112] and Roy et al. [90]. For this purpose, the coolant flow is seeded with a tracer gas as e.g. CO_2 or N_2O and the sealing effectiveness η_s is measured at different sampling points within the wheelspace.

$$\eta_s = \frac{y_A - y_{MF}}{y_{PF} - y_{MF}} \tag{2.2}$$

This sealing effectiveness is a mixing concentration, which in principle determines to what extend the purge flow has been mixed out with main annulus fluid. For this purpose, the tracer gas concentration y is measured at the point of interest (A), within the delivered purge flow (PF) and in the main flow (MF) (see also Chapter 3.3.3 for a detailed description).

With increasing purge flow, the sealing effectiveness initially rises rapidly before it slowly approaches the value 1 at a certain purge flow (see e.g. Daniels et al. [17]). The latter value indicates that there is no hot gas ingestion detectable at the corresponding measurement point. The minimum purge flow necessary to prevent any hot gas ingestion is referred to as $C_{w,min}$. A significant influence on $C_{w,min}$ has, if main flow is neglected, the rotational Reynolds number Re_Φ of the rotor disc (see e.g. Bayley and Owen [4] or Phadke and Owen [75]). This number is mainly determined by the angular velocity ω and the outer radius r_0 of the rotor disc. Thus, there is a direct relationship between the necessary purge flow and the spool speed of the rotor disc.

$$Re_\Phi = \frac{\rho \omega r_0^2}{\mu} \tag{2.3}$$

In addition to the use of gas concentration measurements, the pressure difference between the wheelspace and the main annulus is often used to estimate whether hot gas ingestion occurs (e.g. in Bayley and Owen [4], Phadke and Owen [74], Dadkah et al. [16] and Chew et al. [13]). In this case it is assumed that no hot gas ingestion

occurs if the wall pressure within the wheelspace is above the main annulus pressure, whereas the latter one is sometimes replaced by ambient conditions if the main flow is not assessed. According to Phadke and Owen [75], [76], this method has some arbitrariness since the pressure varies in radial direction within the wheelspace. However they found a good agreement with other techniques using a pressure tap for the wheelspace pressure located at 97% of the hub radius.

To reduce the necessary purge flow, more complex rim seal geometries have been studied. These studies reveal the minimum necessary purge flow $C_{w,min}$ to depend, in addition to Re_{Φ}, on the rim seal geometry. For instance, Phadke and Owen [74] examine by the use of generic rim seal geometries that an axial overlap between the rotor- and the stator platform leads to a significant reduction of $C_{w,min}$. A further comparison of several different generic rim seal geometries and their ability to reduce the demand of purge flow is provided by e.g. Chew et al. [13].

Nowadays, in jet engines or gas turbines, there are often multiple overlapping rim seals used in addition to simple overlapping rim seal geometries (see Fig. 2.3). These multiple overlapping geometries have on the one hand the function to reduce the required purge flow. On the other hand, so called “knife edge seals” or “angel wings” are used to separate the wheelspace into different cavities. The objective here is in accordance to Montomoli et al. [60] to create a recirculation zone in the outer region of the wheelspace, which forms a barrier for the entering main flow and restricts the hot gas ingestion to a locally limited region. This effectively prevents the ingestion of hot gases into lower regions of the wheelspace (see e.g. also Feiereisen et al. [25], Bunker et al. [11] and Zhou et al. [112])

If the main annulus flow of the turbine is taken into account, a further hot gas ingestion mechanism occurs in addition to rotational induced ingress. This is primarily caused by the blade or vane induced pressure fluctuations in the main annulus and is referred to as “Externally Induced Ingress” (see Owen [65]). First studies on this topic have been carried out by Phadke und Owen [76], [77], initially without blades, but with a circumferential pressure variation in the main annulus. These studies reveal that $C_{w,min}$ is proportional to the Reynolds number in the main flow Re_{MF} once a certain value of this number is exceeded. The influence of Re_{Φ} in contrast is negligible at a certain value of Re_{MF}, so that $C_{w,min}$ is almost independent of the rotor speed. An experimental setup with rotor and stator blades in the main annulus was first studied by Green and Turner [32]. Compared to the case without blades, they find an increased purge flow rate in order to prevent hot gas ingestion, which is caused by the trailing edge wakes of the stator vanes and the potential field at the leading edge of the rotor blades. Both effects create pressure fluctuations in the rim seal region. This influence has been studied in more detail by Bohn

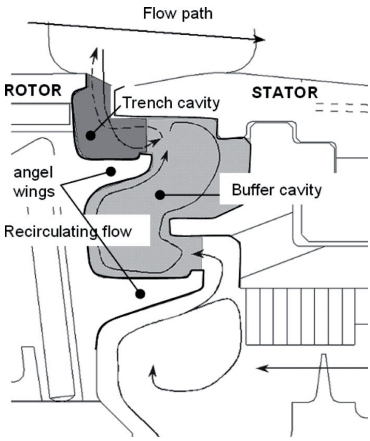

Figure 2.3: *Example of a multiple overlapping rim seal from Montomoli et al. [60]*

et al. [5] with the help of LDA measurements within the rim seal. They show an increase of hot gas ingestion upstream of the blade's leading edge, which is caused by the increased static pressure in this area. In the passage between two adjacent blades, they revealed in contrast outflow of purge flow due to the lower static main annulus pressure. Schematically, the described case with a combination of hot gas ingestion and egress of wheelspace fluid is illustrated in Fig. 2.4, which indicates ingress of main fluid by red arrows and egress of wheelspace fluid by blue arrows.

In addition to the illustrated effects of a single blade or vane row, the interaction between both further influences the hot gas ingestion (see e.g. Bohn et al. [5] or Wang et al. [109]). However, the arising flow structures also depend in accordance to Wang et al. [109] on the purge flow rate [109]. This makes a general statement and description difficult.

The influence of periodic pressure fluctuations in the main annulus can effectively be limited to the outer part of the wheelspace by the use of the already described multiple overlapping rim seal geometries shown in Fig. 2.3 (see e.g. Phadke and Owen [76], Zhou et al. [112] or Sangan et al. [92]).

In addition to rotationally and externally induced ingress as well as a combination of both, large scale flow structures in the wheelspace can influence the hot gas ingestion process according to e.g. Julien et al. [44]. These large scale flow structures travel in the direction of rotor rotation and have been detected in experimental studies by the help of instationary pressure transducers as well as in numerical

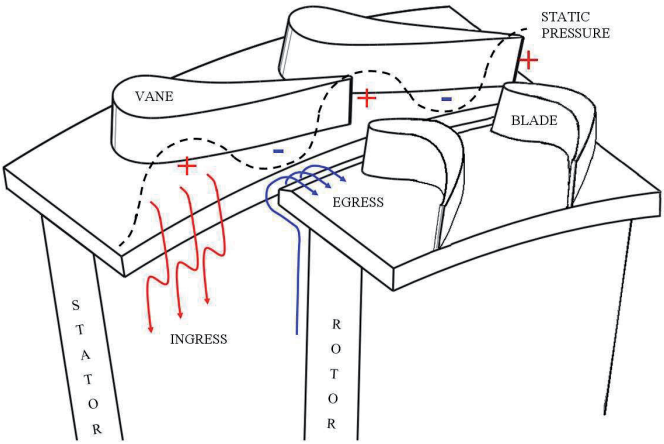

Figure 2.4: *Illustration of ingress and egress as well as the corresponding pressure distribution at the rim seal; according to Sangan et al. [94]*

studies (see Cao et al. [12], Jakoby et al. [36], Roy et al. [90], Julien et al. [44], Boutet-Blais et al. [8] and Wang et al. [109]). In these studies the large scale flow structures can neither be related to the frequencies of the rotor nor to any blade passing frequencies, but rather feature a frequency of 79-97% of the rotor speed. According to Julien et al. [44], Boutet-Blais et al. [8] and Wang et al. [109], the development of these large scale flow structures is significantly influenced by the purge flow rate and attenuates with increasing purge flow. In accordance to Jakoby et al. [36], these large scale flow structures can not be resolved numerically if only a periodic sector of rotor and stator blades is calculated. This fact is according to Jakoby et al. often responsible for an insufficient agreement between experimental and numerical data.
Another effect that influences hot gas ingestion is the turbulent transport of fluid at the overlapping regions of the blade and vane platforms (see Johnson et al. [42]).

In summary the following factors have an influence on the amount of hot gas ingestion:

- Delivered coolant (purge) mass flow
- Rotational Reynolds number of the disc (disc pumping effect)
- Geometry of the wheelspace and the rim seal

- Pressure fluctuations in the main annulus caused by blades and vanes
- Large scale flow structures in the wheelspace
- Turbulent transport mechanisms in the rim seal

2.2.2 Modelling of Hot Gas Ingestion

In addition to the knowledge of the basic flow field within a rotor-stator wheelspace and the hot gas ingestion mechanisms, engineers need robust models to assess the minimum required purge flow to prevent hot gas ingestion. Furthermore, analytic models are useful to understand relationships between purge flow delivery and hot gas ingestion.
For this purpose, important parameters of a wheelspace are presented in accordance to e.g. Sangan et al. [94] with the help of Fig. 2.5. In addition to the already defined rotational Reynolds number Re_Φ, these are the width of the wheelspace s, the outer radius of the wheelspace r_0, the axial seal clearance $s_{c,ax}$, the radial seal clearance $s_{c,rad}$ as well as the overlap between the rotor and stator platform $s_{overlap}$. Furthermore, the derived parameters G, $G_{c,ax}$ and $G_{c,rad}$ are of relevance.

$$G = \frac{s}{r_0}; \qquad G_{c,ax} = \frac{s_{c,ax}}{r_0}; \qquad G_{c,rad} = \frac{s_{c,rad}}{r_0} \tag{2.4}$$

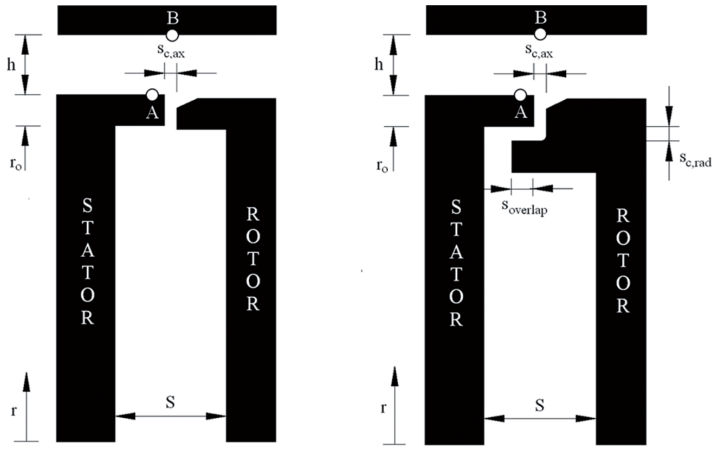

Figure 2.5: *Describing parameters of rotor-stator systems; adapted from Sangan et al. [94]*

Bayley and Owen [4] presented in 1970 a first correlation to assess the minimum required coolant flow to prevent hot gas ingestion. For this purpose, they set up a simplified equation of motion for the shrouded rotor-stator system. Using this model and the obtained experimental data, they found the following correlation for an axial clearance seal, if $G_{c,ax} \ll G$:

$$C_{w,min} = K G_{c,ax} Re_{\Phi} \tag{2.5}$$

The empirical constant K is defined as 0.61 on the basis of experimental data and depends on the rim seal geometry. As already mentioned in Chapter 2.2.1, $C_{w,min}$ primarily depends on the rotational Reynolds number of the rotor disc. In addition, the ratio between seal clearance and wheelspace radius has a direct influence on the necessary coolant flow whereas a narrow gap is beneficial. Even though Equation 2.5 is often used in the literature for other cases, such as externally induced ingress, it is according to Owen [64] only valid for rotationally induced ingress. Similar correlations for rotationally induced ingress have been presented by e.g. Chew et al. [13].
A first correlation for externally induced ingress has been proposed and compared with experimental data by Phadke and Owen [77]

$$C_{w,min} = 2\Pi K G_{c,ax} (P_{max})^{1/2} \qquad \text{using} \qquad P_{max} = \frac{\rho \Delta p_{max} r_0^2}{\mu^2} \tag{2.6}$$

In this equation Δp_{max} represents the maximum annulus pressure variation in circumferential direction, which depends on the main flow Reynolds number. The constant K has been determined by Phadke and Owen from their experimental data for an axial clearance seal with a value of 0.6. Additional values for K have been obtained by Bohn and Wolf [6] for other rim seal geometries.
In addition to these correlations, “Simple Orifice Models” are increasingly used to estimate the minimum required coolant flow $C_{w,min}$. For this purpose the rate of ingress and egress is assessed by means of the pressure difference across the rim seal. If the pressure distribution is known in the main flow and within the wheelspace, the required coolant flow rate can be calculated. To account for viscous losses, discharge coefficients C_d are used in these models. However, to determine these discharge coefficients, experimental data are in general required. An overview of different models is provided by Johnson et al. [43].
Owen [64], [65] solved the incompressible as well as compressible orifice equations analytically for rotationally induced ingress, externally induced ingress and

combined ingress. As simplification, he used a “saw tooth model” to approximate the periodic pressure fluctuation in the main flow. To account for viscous effects, discharge coefficients have been used for ingress and egress separately. The obtained analytical equations show the main parameters that influence the sealing effectiveness. Furthermore, these models can be used to extrapolate data from one geometry to a geometrically similar geometry with the help of only a few experimental or numerical data points (see Owen et al. [68], [67]). In this case the advantage is that the exact pressure distribution within the main flow or within the wheelspace is not necessarily required. In addition, the analytic models provide some general findings regarding hot gas ingestion. For example, it is shown that the maximum mass flow of ingested fluid is equivalent to 35% of $C_{w,min}$ if the discharge coefficients for in- and outflow are equal and if swirl within the main flow is neglected. Furthermore, a coolant flow of 50% $C_{w,min}$ leads already to a sealing effectiveness of 80%. A good agreement between the analytical models and experimental data is shown by Owen [64], [65] and Sangan et al. [94], [93].

2.2.3 The Interaction between Purge and Main Annulus Flow

In addition to the research on hot gas ingestion mechanisms and the flow field within the rotor-stator wheelspace, the interaction between purge and main annulus flow is an important field of research. For instance, it is known that the purge flow influences the hub side boundary layer when it enters into the main flow. Hence, it has the potential to influence the development of secondary flow structures, losses and the characteristics of a turbine. This section reviews the open literature which investigates the interaction between purge and main annulus flow.
In these investigations the mass flow through the rim seal is generally specified in terms of the percentage mass fraction of the main annuls flow. This rate is often referred to as injection rate IR, which shall also be used in this work. Only a few investigators use the dimensionless C_w value that has been defined in Chapter 2.2.1.

$$IR = \frac{\dot{m}_{PF}}{\dot{m}_{MF}} \tag{2.7}$$

One of the first studies investigating the influence of purge flow on the main flow aerodynamics has been performed by McLean et al. [58], [59]. They experimentally study the effect of purge flow injected downstream of the first NGV row of a high pressure turbine. Primarily a radial shift of the hub side passage vortex towards midspan is observed for increased purge flow. This shift of the hub side secondary

flow structures has also been observed by Schuepbach et al. [99], [100], Jenny et al. [37], [38], Reid et al. [88], Paniagua et al. [69] and Rakenius et al. [87].

Exemplarily, Fig. 2.6 shows the total pressure distribution and the circumferentially averaged yaw angle downstream of a rotor row for two different purge flow rates, whereas the purge flow is injected upstream of the rotor row. From both figures it can be examined that the hub side secondary flow structures have a larger radial extent and are shifted radially towards the channel's midspan in case IR is increased.

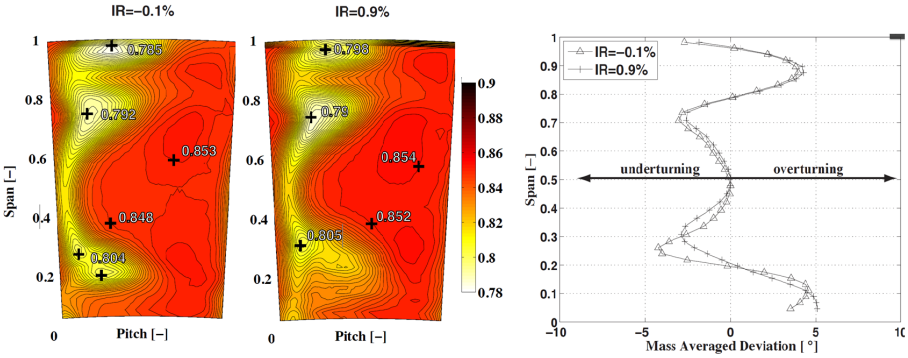

Figure 2.6: *Distribution of the total pressure (shown in the relative frame and based on the inlet total pressure) and the yaw angle downstream of a rotor row for two different purge flows; adapted from Schuepbach [98]*

Whereas McLean et al. [58], [59] observe only a shift of the secondary flow structures but no intensification, Paniagua et al. [69] and Reid et al. [88] also observe intensified secondary flows in terms of an increased under- and overturning. In contrast, Schuepbach et al. [99], [100] determine the peak intensity of the secondary flows to decrease in terms of vorticity. However, the area affected by secondary flows increases in size, leading to increased overall losses.

One explanation for the radial shift of the passage vortex is given by Schuepbach [98] for the geometry he investigated. He shows numerically that the purge flow enters the main flow in terms of discrete jets, which are located upstream of the suction side area of the rotor blade. These jets cause a blockage and hence deflect the main flow radially outwards. The jet itself is however deflected towards the hub. This causes two regions of counter rotating vorticity, which are first oriented normal to a meridional plane. When this additional vorticity is turned around the leading edge of the rotor row, new streamwise vortices are generated within the

rotor passage. These vortices first interact and further downstream merge with the passage vortex. Due to this interaction between the additional vortex and the passage vortex, the radial shift of the passage vortex can be explained. A further influence of the purge flow on secondary flow structures has been investigated by Gallier et al. [26], [27] with the help of PIV. They detect the formation of the horseshoe vortex at the leading edge of a rotor blade to be intensified by the egress of purge flow. In addition, they study the influence of stator wakes and the potential field of the rotor on the flow structure in the region of the rim seal and the leading edge of the rotor.

Another purge flow induced effect is the creation of a blockage in the main flow in the vicinity of the rim seal (see Paniagua et al. [69] and Schuepbach et al. [100]). As a result of this blockage, the static pressure rises upstream of the rim seal. This in turn leads to a deceleration and a re-distribution of the main flow radially outwards. Due to the deceleration of the flow, the velocity triangles change upstream of the rim seal. This can alter the degree of reaction of the turbine stage. For instance, Paniagua et al. [69] examine an increased degree of reaction of 11% if the purge flow rate is elevated from -0.5% to 1.5%.

If the flow within the rim seal is compared with the one in the mainflow, it suffers in general a deficit in axial velocity V_x as well as in circumferential velocity V_Θ (see e.g. Chilla et al. [14]). The deficit in V_Θ is caused by the fact that the circumferential velocity component is only applied by friction at the rotating walls and not by the turning of the vanes. This causes unequal velocity triangles between the main flow and the rim seal flow as illustrated in Figure 2.7.

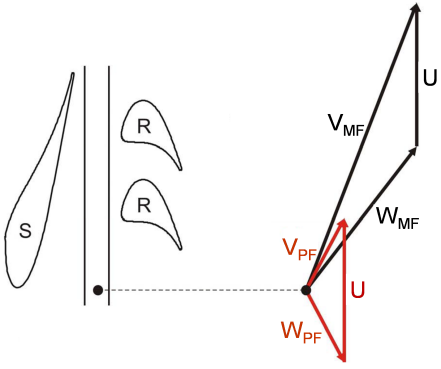

Figure 2.7: *Illustration of the velocity triangles in the vicinity of the rim seal; adapted from Chilla et al. [14]*

These unequal velocity triangles cause shear layers and hence mixing losses at the re-entry of the purge flow. These mixing losses are according to Gier et al. [30] and Ong et al. [63] the main contributors to the overall losses that occur due to purge flow injection. In addition to mixing losses, the shear layers promote the development of Kelvin-Helmholtz instabilities in the rim seal region, as described by Rabs et al. [83], [84], [85] and Chilla et al. [14].
In addition to the increased mixing losses, the altered velocity triangles lead to a negative incidence situation at the downstream blade row if the purge flow enters into the main annulus (see e.g. Jenny et al. [37], Reid et al. [88], Bouded et al. [7] or Zlatinov et al. [113]). As a consequence, the stagnation point moves towards the suction side of the blade and a decreased blade loading close to the hub side endwall is observed (see e.g. Denos and Paniagua [18] or Paniagua et al. [69]).
If in contrast main annulus flow enters through the rim seal into the wheelspace, it carries in accordance to Roy et al. [91] a high tangential velocity component (swirl) and thus influences the flow field within the rim seal and wheelspace, leading primarily to an increased swirl. To illustrate the effect of this, Fig. 2.8 shows the streamlines close to the rotor hub side endwall for different purge flow rates, which have been obtained by Popovic and Hodson [78] using numerical simulations. Additionally, the radial velocity component at the rim seal is shown, whereas negative values indicate ingestion and positive values egress.

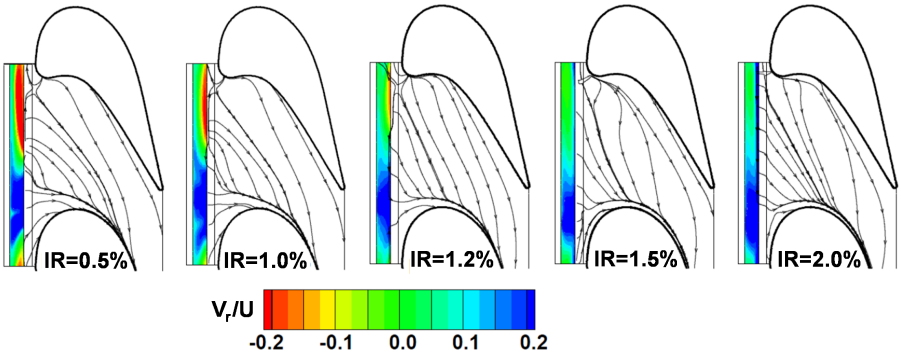

Figure 2.8: *Streamlines close to the rotor endwall and distribution of radial velocity within the rim seal (normalized by the rotor speed) at different purge flow rates; adapted from Popovic and Hodson [78]*

At low purge flow rates the ingestion of main annulus flow leads according to Popovic and Hodson [78] to a partial removal of the boundary layer. Moreover, the

ingested main flow mixes with the purge flow in the wheelspace and increases the swirl, as it has already been stated above. As a result of both effects, the crossflow within the blade passage is reduced and attaches further downstream at the blade's suction side. Overall, the detrimental effects of the purge flow are reduced due to the partial removal of the boundary layer and the aerodynamically favourable entry of the purge flow. This in turn leads only to moderate losses due to purge flow injection at low injection rates.

If the purge flow is increased ($IR > 1.1\%$), the hot gas ingestion and thus the removal of the boundary layer is reduced or completely avoided. In addition, the purge flow is now injected into the main flow with a reduced or even negative tangential velocity component, since less ingested main annulus flow, which owns a higher tangential velocity component, mixes with the purge flow in the wheelspace. This reduced tangential velocity promotes in accordance to Popovic and Hodson the crossflow within the passage and leads to an earlier attachment of the pressure side leg of the horseshoe vortex on the suction side surface of the blade. Caused by this, the passage vortex travels longer across the suction side surface of the blade and moves radially further outwards. Hence, this is another explanation for the radial migration of the secondary flow structure due to purge flow injection. In this purge flow range the losses are most sensitive to the purge flow rate.

Is the purge flow increased even further ($IR > 1.5\%$), the losses appear to be least sensitive to the purge flow rate. This can be explained in accordance to Popovic and Hodson by the fact that the purge flow enters the main flow with a high axial momentum. This re-energizes the inlet boundary layer and reduces the crossflow and hence the development of secondary flows within the passage.

According to Erickson et al. [23], Pau et al. [71] and Paniagua et al. [69], the main part of the purge flow enters into the passage vortex. Consequently, the cold fluid lifts off from the endwall, reducing a potential cooling of the hub side endwall significantly. This potential cooling of the platform has been investigated by e.g. Erickson et al. [23], [22]. Exemplarily, their results are shown in Fig. 2.9, which presents the measured adiabatic cooling effectiveness at the hub side endwall of a rotor blade at different purge flow rates. Due to the crossflow within the passage, the main part of the purge flow is swept to the suction side of the rotor blade. There it finally lifts off from the endwall and enters into the passage vortex. It can clearly be observed that the largest part of the endwall is not cooled by the purge flow, even if the purge flow rate is increased. Qualitatively, similar results have been shown by Suryanarayanan et al. [104] and Popovic und Hodson [78].

However, due to the entry of the purge flow into the passage vortex, there is the possibility to cool the suction side surface of the blade. As an example Fig. 2.10

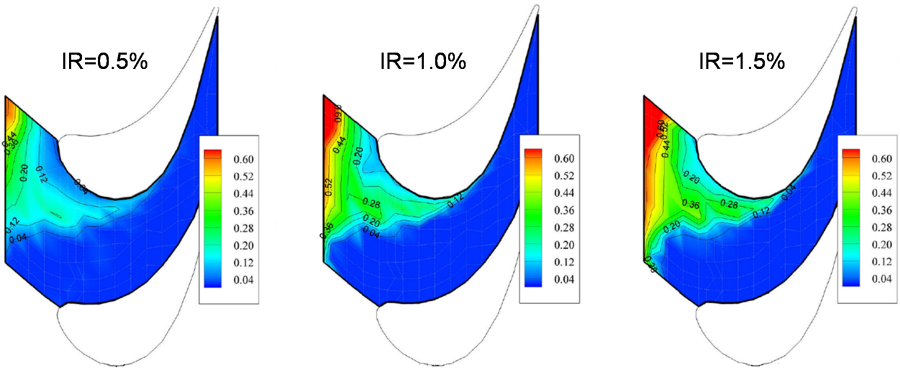

Figure 2.9: *The adiabatic cooling effectiveness at a rotor platform at different purge flow rates; adapted from Erickson et al. [23]*

shows the adiabatic cooling effectiveness downstream of the purge flow injection in a linear cascade, measured by Popovic und Hodson [78]. The increased cooling effectiveness of the suction side surface along the trajectory of the passage vortex is clearly visible. This suggests a potential cooling of the suction side surface, which according to Denos and Paniagua [18] should not be neglected during the design process of the blade. Nevertheless, it should be considered that the changed flow structure may also alter the heat transfer coefficient at the blade surface. For instance, Popovic and Hodson [78] observe in the area of the increased cooling effectiveness also an increased heat transfer coefficient. In their study, this increased heat transfer coefficient balances the advantage of the colder endwall temperature almost completely, so that the averaged net heat flux is nearly unchanged.

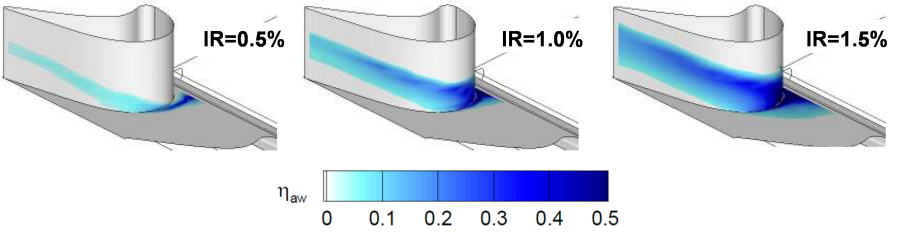

Figure 2.10: *Influence of the hub side purge flow injection on the adiabatic cooling effectiveness at the suction side of a rotor blade; adapted from Popovic and Hodson [78]*

In general, the previously mentioned effects, such as the intensified secondary flows, lead to detrimental effects and result in increased losses and a decreased turbine efficiency. For instance, Schuepbach et al. [99] measure an efficiency decrease of 0.7% in a 1 $\frac{1}{2}$ stage subsonic axial turbine if the purge flow rate is increased by 1%. Reid et al. [88] determine for a purge flow rate of 2% an efficiency drop of 1.05% with respect to the case without purge flow. In a numerical study Pyliouras [82] has shown an efficiency deficit of 0.4%-0.5% in a low Mach number 1 $\frac{1}{2}$ stage turbine test rig and an efficiency decrease of 0.15% per 1% of delivered purge flow in the Rolls-Royce E3E Core3/2 high pressure, high Mach number turbine (also subsonic). Rakenius et al. [87] measured in a 1 $\frac{1}{2}$ stage subsonic turbine an efficiency drop of 0.65% per 1% purge flow for an axisymmetric endwall design.
An exception are transonic turbines, featuring a shock system at the trailing edge of the vane. In this case, not only the secondary flow structures are altered by the purge flow injection but also the shock systems. For instance, Pau et al. [71], [70] found an increased turbine efficiency of 1.04% if the purge flow rate is increased from -1% to +0.8%. They explain this with a modification of the trailing edge shock system, leading to reduced shock losses.

A detailed loss breakdown into different loss sources is presented by Gier et al. [30]. For this purpose, the geometry of a low pressure turbine has been simulated numerically, with and without cavities. With cavity, hot gas is ingested upstream of the stator row, fed through the interstage labyrinth seal under the stator and is finally discharged back into the main flow upstream of the next rotor row. Even though there is no external cooling fluid delivered into the cavity, a comparison of the two cases is suitable to study the different loss mechanisms. In addition, it allows to identify the losses that occur purely due to the presence of the rotor-stator wheelspace even though there is no external purge flow applied. The following cavity related losses are summarized by Gier et al. for the investigated low pressure turbine. In addition, the relative fraction of each loss is provided by Gier et al.

- Subsequent row losses; 12,5% of the losses
- Mixing losses; 47,5% of the losses
- Bypass losses; 18,8% of the losses
- Step losses; 18,8% of the posses
- Windage losses; 2,5% of the losses

The “Subsequent row losses” include the already described losses caused by the altered incidence situation as well as the changed secondary flow structures within

the downstream vane row. The most dominant losses are the mixing losses originating from the shear layers between the purge and the main annulus flow. This is in analogy to the observations given by Reid et al. [88] and Ong et al. [63], who also identify these losses to be dominant. The bypass losses are caused by the fluid leaking through the interstage seal. This fluid is not turned in the vane, but experiences approximately the same pressure drop. The magnitude of these bypass losses primarily depends on the radial clearance of the interstage seal. The step losses are accounting for Carnot-like losses caused by the sudden increase in cross sectional area of the main annulus at the rim seals. The windage losses are caused by additional friction at the rotating discs within the wheelspace but are of minor relevance.

To reduce the mixing losses between the main and the purge flow, the latter one can be delivered with a pre-swirl into the direction of rotor rotation (for purge flow injection upstream of a rotor row). Hereby, the detrimental effect of purge flow injection is partly compensated. For instance Ong et al. [63] show that the variation of the inlet swirl from 0° to 70° results in an efficiency gain of 0.75%. Qualitatively, similar observations have been presented by Girgis et al. [31] and Reid et al. [88]. This pre-swirled delivery of the purge flow is found frequently in the first stage of a high pressure turbine using so-called pre-swirl nozzles. However, the main reason for the implementation of these nozzles is the possibility to reduce the total temperature within the relative-frame of reference and thus improve the cooling of the rotor discs and blades (see e.g. Bräunling [9], Bricaud et al. [10]). Mahle [56] studies numerically the effect of a turning device in the wheelspace of a low pressure turbine. This device reduces the discrepancy of the flow direction between the main and the purge flow. For a three stage low pressure turbine, this feature generates an efficiency increase of 0.1%.

Besides the use of pre-swirled purge flow, an optimised rim seal geometry can reduce the losses caused by purge flow injection. For this purpose, Schuler et al. [102], [101] as well as Popovic and Hodson [79], [80] study the influence of different rim seal geometries in linear cascades. Their experimental and numerical results reveal that an improved design of the rim seal geometry is able to reduce the losses that are induced by the purge flow. However, it needs to be considered that the sealing effectiveness is also influenced by the rim seal geometry. Nevertheless, Popovic and Hodson [80] develope a geometry which reduces, in comparison to geometries that are representative of current industrial practice, the losses caused by purge flow injection and maintains the sealing effectiveness (for IR $>$ 0.75%). Erickson et al. [23], [22] demonstrate furthermore that a proper rim seal geometry allows in addition to improve the cooling effectiveness at the rotor platform.

Schuepbach et al. [100], Jenny et al. [38] and Rakenius et al. [87] examined the possibility to reduce the sensitivity of turbine efficiency to purge flow using non-axisymmetric endwall designs. A first design tested by Schuepbach et al. [100] is based on a design philosophy, which uses an optimisation algorithm to reduce the secondary kinetic energy within the passage. This design leads to an efficiency increase of approx. 1% compared to the baseline configuration using cylindrical endwalls. However, it increases the sensitivity to purge flow from 0.6% to 1.2% per percent purge flow. A second endwall design was tested using a design philosophy that reduces the cross passage pressure variation at the vane exit. Using this design philosopy, the sensitivity of turbine efficiency to purge flow was only slightly worse than the baseline configuration, resulting in a 0.7% efficiency drop per percent purge flow injection. Nevertheless, the efficiency without purge flow increases by 0.3% compared to the baseline configuration, resulting in an overall efficiency increase. Jenny et al. [38] study a non-axisymmetric endwall design that is employed up to the leading edge of the rotor platform. This design shows an increased turbine efficiency as well as a reduced sensitivity to purge flow. Rakenius et al. [87] also compares a non-profiled rotor endwall with a profiled endwall and assesses a reduced efficiency sensitivity to purge flow injection by about 40%.

2.3 Conclusion and Suggestion of Further Possible Research Activities

Summarising the literature review in Chapter 2.2, it can be stated that a number of effects, induced by the presence of purge flow, have already been elaborated and described by many authors in the open literature. For instance, the basic flow field within the rotor-stator wheelspace is known. There are methods available to estimate the necessary purge flow to prevent hot gas ingestion and it is basically known how the purge flow interacts with the main annulus flow.

While some effects caused by the purge flow injection are well explained in the literature, some other effects still need further attention to gather additional information. For example the development of the large scale flow structures within the rotor-stator wheelspace, described in Chapter 2.2.1, is not yet fully understood. In addition, it has to be mentioned that most of the research dealing with the interaction of purge and main flow is performed at rigs with different rim seal and cavity geometries as well as turbine characteristics. For this reason a general transfer of losses and flow features from one to another rim seal or turbine design is if at all very difficult (as it has similarly been stated by Pyliouras [82]). This implies that additional numerical and/or experimental tests are still necessary to

broaden the general understanding of the interaction between purge and main flow. However, the already obtained results and correlations can be used as a guideline during the design process of new turbines.

In addition, the literature study reveals that most of the research on the interaction between purge and main flow investigates configurations where the purge flow enters into the main flow upstream of a rotor row. This is quite obvious as the temperature is in general higher upstream of a rotor row than at downstream positions. Hence, hot gas ingestion is more severe at this position and needs to be prevented successfully. However, some of the downstream rotor-stator gaps also need to be purged to prevent hot gas ingestion or at least reduce it to a tolerable amount. For this reason, not only the purge flow upstream of a rotor row but also the one upstream of a stator row should be studied in detail.

A few studies regarding this topic have been performed during the MAGPI project at the University of Sussex and are summarized by Dixon et al. [20]. Howsoever, the primary objectives of these studies are on heat transfer and an optimised cooling flow distribution within the wheelspace. The interaction of purge and main annulus flow is of secondary concern and only studied numerically. Likewise, Okita et al. [62] and Balasubramanian et al. [3] investigated configurations where the purge flow enters the main flow upstream of a stator row. As the Sussex team, they have not studied the influence of purge flow on the main annulus aerodynamics in detail. The influence of purge flow on the main flow upstream of a guide vane has been studied numerically by Montomoli et al. [60] and Gier et al. [30], however only for a fixed purge flow rate or without the supply of external coolant flow. Schuler et al. [102], [101] have studied the influence of purge flow on the main annulus flow, but only in a linear cascade, so that the influence of the rotor disc and blades on the purge flow is not represented. Most recently, Linker [55] has assessed the purge flow injection upstream of a stator row in a predecessor work of this thesis. However, he has altered the purge flow simultaneously upstream of the rotor and the stator row, so that a decoupled effect of the stator row is hard to assess. Furthermore, only two different purge flow rates are assessed.

To illustrate the basic difference between purge flow that enters upstream of a rotor and upstream of a stator row, the velocity triangles of main flow and purge flow are shown at both locations in Fig. 2.11. In this figure, the purge flow is represented in green colour and the main flow in red colour. The absolute velocities are shown by solid arrows whereas the ones in the relative system are shown dashed. The velocity triangles of the purge flow are shown for three different cases in order to explain several injection conditions. For the reference case, marked with **A**, it is assumed that the circumferential velocity of the purge flow corresponds to 50% of

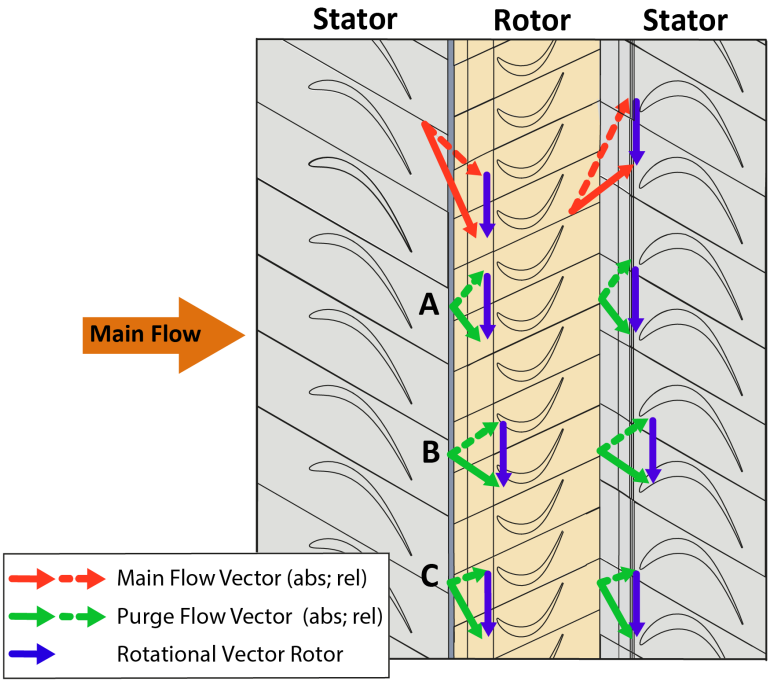

Figure 2.11: *Illustration of purge flow injection upstream and downstream of a rotor row for different conditions; A: Reference case, B: Increased axial velocity of purge flow, C: Increased swirl of purge purge flow; adapted from Schrewe et al. [97]*

the rotor speed at hub radius. The axial velocity of the purge flow is assumed to be 50% of the main flow axial velocity. Analysing the purge flow injection in the absolute frame of reference, it can be observed that the difference in flow direction between purge and main annulus flow is increased upstream of the stator row. As the mixing losses are primary dependent on the difference in flow direction and magnitude in the absolute frame of reference, higher mixing losses can be assumed upstream of a stator row. However, this depends strongly on the actual velocity triangles in the considered turbine.

To analyse the incidence situation at the blades and vanes, the velocities in the rotor relative frame need to be investigated upstream of the rotor, whereas the absolute ones need to be examined upstream of the stator. If the velocity vector of the purge flow is assessed, the following effects are obtained: Both, the blade and vane

row experience a negative incidence due to the presence of purge flow in the near endwall region. If the axial velocity of the purge flow is increased, as indicated by the velocity triangle marked with **B** in Fig. 2.11, the negative incidence is reduced upstream of the rotor and the stator row. However, if in contrast the circumferential velocity of the purge flow and hence its swirl is increased, the incidence at the rotor is decreased, whereas it is increased at the stator row (see velocity triangle marked with **C**). This suggests that the results obtained upstream of a rotor row might not be analogue to the ones upstream of a stator row.

Another subject which has not been studied in detail in the open literature so far is the effect of different purge flow delivery methods on the interaction between purge and main annulus flow. According to the turbine stage, there are different possibilities to feed purge flow into the rotor-stator wheelspace. These are particularly pronounced between the front cavity of the high pressure turbine and the one upstream of a stator row in a low pressure turbine. To illustrate this, Fig. 2.12 shows exemplarily on the left hand side the coolant supply upstream of the first rotor row in a high pressure turbine. In this case, the coolant is fed into the wheelspace from the stationary system using labyrinth seals, pre-swirl nozzles or other supply holes and slots. A large fraction of the supplied coolant is drawn into the rotor blades where it is used for internal and film cooling purposes. The swirl within the wheelspace is influenced by friction at the walls, the coolant mass flow, the pre-swirl system and the labyrinth seals as well as the wheelspace and rim seal geometry.

In contrast, the coolant supply upstream of the vane row in a low pressure turbine is illustrated in a schematic manner on the right hand side in Fig. 2.12. In this case, the coolant flow is often supplied through holes or slots located in rotating components. Hence, the coolant flow is fed into the wheelspace with a circumferential velocity component in rotor rotational direction.

If the coolant flow is fed through discrete drive arm holes as illustrated in Fig. 2.12, it may enter the wheelspace in form of jets, as shown by Andreini et al. [2]. Depending on the position of the holes and the momentum of these jets, it seems possible that these jets influence the flow field within the rim seal and the main flow. A first indication that these “drive arm hole jets” are able to influence the flow field within the main annulus and possibly the rim seal has been provided in a predecessor work by Linker [55]. Using the same turbine configuration as in this thesis, he examines regions of underturning that are periodic with the drive arm holes. Exemplarily, Fig. 2.13 shows the rotor relative yaw angle downstream of the stator row, whereas the purge flow is injected through discrete drive arm holes upstream of this vane row. Clearly, the drive arm hole periodic regions of underturning are visible within the lower channel height. However, in addition to these results there are to the

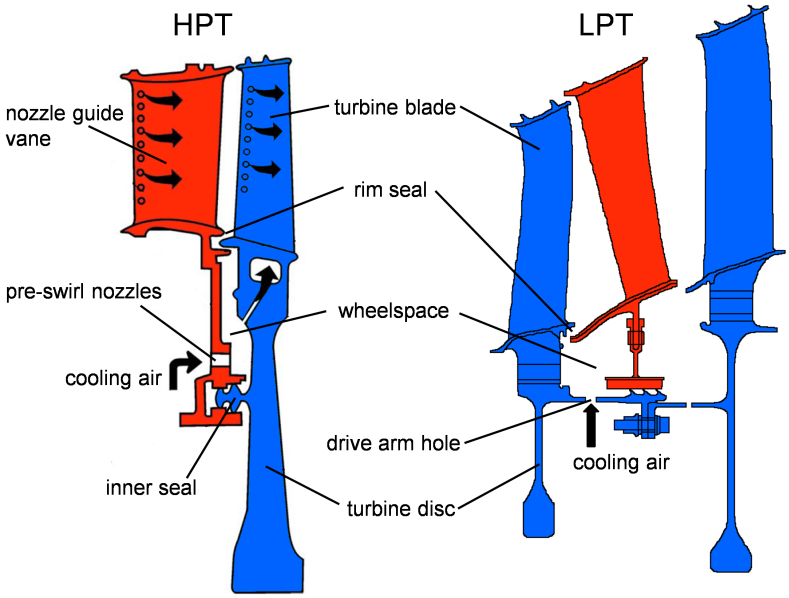

Figure 2.12: Supply of wheelspace coolant flow at different positions in the turbine; left: Upstream of the first rotor row of a HPT, right: Upstream of a stator row of a LPT, adapted from Owen [64] and The Jet Engine [89]

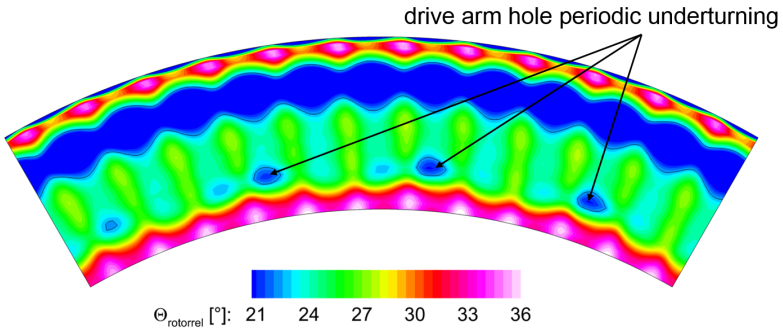

Figure 2.13: Potential effect of drive arm hole jets in the main flow of a turbine; adapted from Linker [55]

author's knowledge no experimental investigations available which study the effect of these drive arm hole jets on the interaction between purge and main flow in detail. Hence, this influence should be part of the research on the interaction between purge and main annulus flow upstream of a stator row, as it has also been proposed by Linker [55].
For this purpose, the penetration depth of the drive arm hole jets should be altered in addition to the injection ratio IR. A parameter to describe the penetration depth of a jet is the effective velocity ratio J_e, which is typically used in technical applications where a jet penetrates into a free stream (see "Jet in Crossflow" phenomenon reviewed e.g. by Margason [57]). According to Margason, it is defined as the square root of the momentum ratio between the entering jet and the freestream. Applying it to the situation in the wheelspace, the following equation is assessed:

$$J_e = \left(\frac{\rho_{jet} \, {W_{jet}}^2}{\rho_{WS} \, {W_{WS}}^2} \right)^{1/2} \tag{2.8}$$

In this equation the velocity of the jet W_{jet} and the flow in the wheelspace W_{ws} are rotor relative values, since the drive arm hole jets are located in the relative frame of reference. The velocity of the wheelspace W_{WS} is assumed to be dominated by the circumferential velocity in the wheelspace.

3 Experimental Setup and Measurement Methods

To investigate the interaction between purge and main annulus flow upstream of a stator row, the Large Scale Turbine Rig (LSTR) has been used as a test facility. In this chapter this test rig, its typical characteristics and the applied measurement techniques are described.

3.1 The Large Scale Turbine Rig

The LSTR is an upscaled, two stage low Mach number research turbine operating at engine representative Reynolds numbers. Based on the height of the first NGV row, the scale is approx. 3 times the size of a BR700 family engine from Rolls-Royce. This dimension of the test rig is one of its main advantages and allows to insert aerodynamic probes into regions which are hardly accessible by probes in unscaled turbines. In addition, the influence of intrusive measurement techniques is reduced since the percentage blockage of the main flow is in general smaller. Another advantage of the test rig is its capability to provide up to 20% of the main flow as secondary air for several purposes as e.g. purge flow injection or film cooling of blades or vanes. All this makes it an appropriate test rig for the current investigation. However, as the rig is operated at cold conditions, it was not possible to account for the density difference between purge and main flow.

A detailed description of the LSTR, its design philosophy, characteristics and control system is provided by Linker [55], however its salient features are presented below. For this purpose, Fig. 3.1 illustrates the general layout of the test rig, which is basically set up in a closed loop configuration. The main flow is provided by a KK&K compressor driven by a Siemens 970 kW AC drive. It delivers a maximum pressure ratio of 1.8 and a maximum mass flow of 21 kg/s, which is metered by a Venturi pipe downstream of the blower. To ensure a homogeneous flow at the inlet of the turbine, a settling chamber consisting of several screens and flow straighteners is located upstream of the turbine. Downstream of the turbine an exhaust casing turns

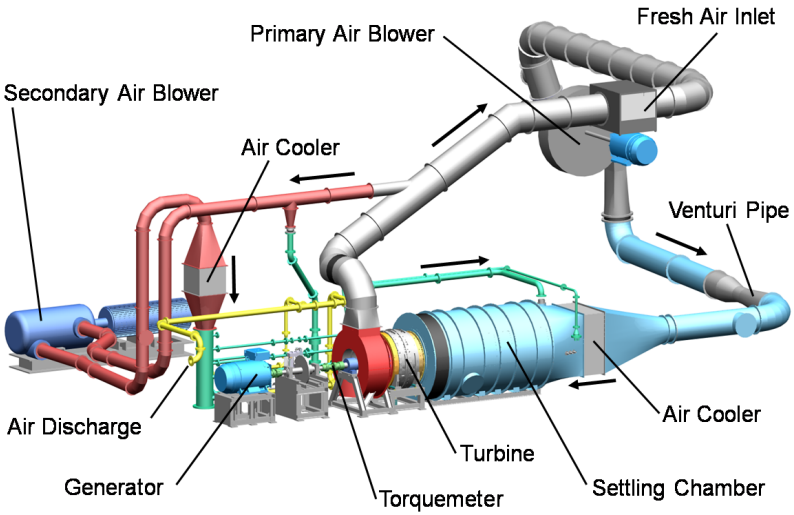

Figure 3.1: *General layout of the LSTR*

the flow by 90° before it is guided back to the primary air blower. The energy of the turbine is absorbed by an electric generator. To measure the shaft torque of the turbine, a torquemeter is situated between the main bearing and the generator. To control the mass flow of the primary air blower and the spool speed of the turbine, PI or PID controllers are used in conjunction with Loher Dynavert T frequency converters. These frequency converters also recover the shaft power absorbed by the generator and feed it back to the primary air blower in order to reduce energy consumption. To avoid a continuous heating of the flow, a water driven heat exchanger is installed upstream of the settling chamber, capable to extract a heat flow of 360 kW. This heat exchanger is also used to control the turbine inlet temperature. For this purpose its water flow rate is continuously regulated by a PID controller.

The purge flow is provided by a Continental Industries 151B compressor, which delivers a maximum mass flow of 4.8 kg/s and a maximum pressure ratio of 2.2. The temperature of the purge flow is adjusted by a second water driven heat exchanger. Downstream of this heat exchanger, the flow is divided into several pipes (green colour in Fig. 3.1). The mass flow within these pipes is measured by orifices and adjusted by ball valves using PID controllers. Finally, these pipes deliver the purge

flow through a core pipe within the settling chamber into the different rotor-stator wheelspaces of the turbine. An overview of the rig's main data is given in Table 3.1.

Table 3.1: *Main data of the LSTR*

Max. spool speed [rpm]	1500
Max. pressure ratio primary blower [-]	1.8
Max. mass flow main annulus [kg/s]	21
Max. mass flow secondary air [kg/s]	4.8
Max. shaft power [kW]	540
Max. shaft torque [N]	3400
Outer diameter main annulus [mm]	1136
Inner diameter main annulus [mm]	868

To illustrate the flow within the turbine and the wheelspaces, Fig. 3.2 shows a cross sectional view of the turbine. In this figure the stator vanes are shown in blue and the rotor blades are shown in orange. All stationary parts such as the outer casing and the hub side inlet cone are illustrated in grey colour. The rotating parts, except of the rotor blades, are skin coloured. The purge flow enters into the turbine's interiour via two different pipe systems, labelled with coolant flow 1 and coolant flow 2 in Fig. 3.2. Coolant flow 1 provides primarily the purge flow into the S1R1 wheelspace. Coolant flow 2 primarily delivers the purge flow into a subcavity, which in turn feeds the R1S2 wheelspace through 24 discrete drive arm holes.

Due to the existence of rotating and non-rotating parts, the different cavities are interconnected by labyrinth seals. These labyrinth seals allow for a flow between the different wheelspaces. For instance, there is some flow between the S1R1 wheelspace and the subcavity, which depends primarily on the pressure difference between these two cavities. Furthermore, some fluid is transferred across the labyrinth seal underneath the second stator vane from the R1S2 wheelspace to the S2R2 wheelspace. Since the massflow through the labyrinth seal could not be measured, it was predicted by the industrial partner Rolls-Royce using the flow network solver model SPAN.

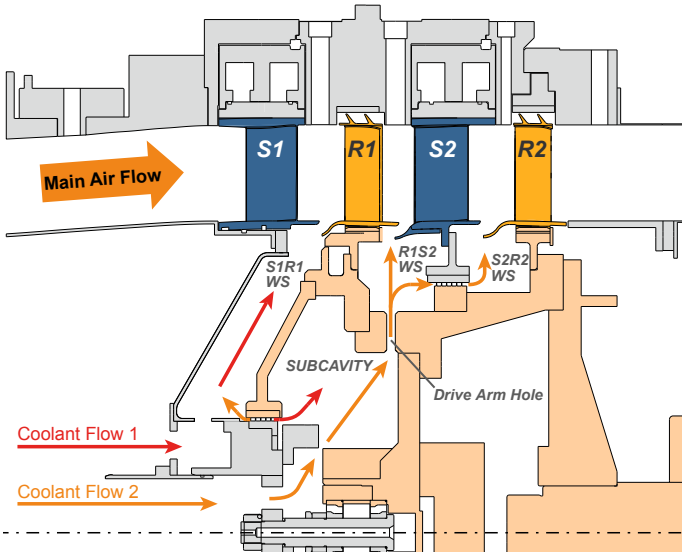

Figure 3.2: *Illustration of different flow paths in the LSTR; adapted from Schrewe et al. [96]*

3.2 Geometry and Characteristics of Blading and Wheelspace

The blading studied in this thesis was designed during the MAGPI project by the industrial partner ITP from Spain and is referred to as the MAGPI blading in the following. The blading is representative of a modern low pressure turbine and consists of 48 stator vanes and 72 shrouded rotor blades in each row. Since the LSTR had originally been designed to be representative of a high pressure turbine with typically low aspect ratio airfoils, a compromise was found by the industrial partners between the aspect ratio and the blade to vane spacing for the low pressure turbine blades, which usually feature a higher aspect ratio. This leads to airfoils with a smaller than realistic aspect ratio, however it was ensured by means of CFD calculations that the hub- and tipside secondary flow structures do not interact with each other. The profile of stator 2 at 50% channel height coincides with the one studied by Schuler et al. [102] [101] in a linear cascade during the MAGPI project. The endwalls of blades and vanes are axisymmetric and the purge flow was not taken into account during the aerodynamic design process of the blading. Some typical characteristics of the blading are provided in Table 3.2, in which the Reynolds number is calculated with airfoil outlet conditions

Table 3.2: Parameters of the MAGPI blades, according to Schrewe et al. [97]

	Stator 1	Rotor 1	Stator 2	Rotor 2
No. of blades	48	72	48	72
Aspect Ratio [-]	1.77	2.77	1.77	2.66
Hub/Tip Ratio [-]	1.31	1.31	1.31	1.31
Turning [°]	65.2	101.8	101.4	106.1
Re [10^5]	5.4	3.5	5.8	4.1

and the suction side profile length of the blade or vane. The blades are made from cast plastic material to facilitate the manufacturing and reduce the costs compared to metal blades. A geometric measurement of the blades revealed tolerances to be less than 0.5% of the channel height. At the hub all platform wedge face gaps are filled with silicon material to avoid any flow through these gaps. The front part of the stator 2 platform is exchangeable to study different rim seal geometries (see Fig. 3.4). Yet, in this thesis only a baseline geometry is studied.

Even though the full design philosophy of the blades has not been disclosed by ITP for reasons of confidentiality, one feature of the blades is presented to support the understanding of the results presented in Chapter 6. For this purpose, the front part of stator 2 is shown in detail in Fig. 3.3. In this figure it gets obvious that the leading edge of the vane is straight across the entire channel height with exception of the hub region, where it is bent towards the pressure side. This makes it difficult to define the exact position of the leading edge at several channel heights. For simplicity the position of the leading edge used in this work is defined to be the one at 50% channel height, indicated by the red line in Fig. 3.3.

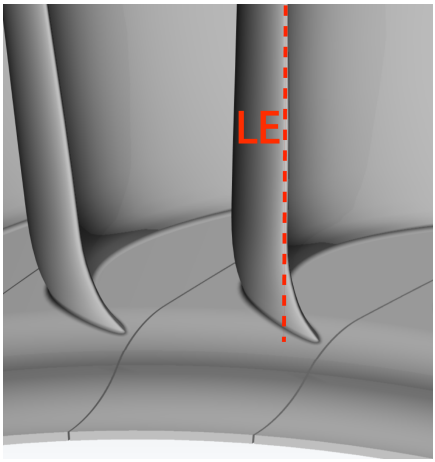

Figure 3.3: Leading edge geometry S2

The general layout of the rim seal and the wheelspace is illustrated in Fig. 3.4. The rim seal was designed by ITP to be representative for rim seal geometries of typical low pressure turbines and features an axial overlap between the rotor platform and the stator platform.

The geometry of the wheelspace originates primarily from the re-use of a preliminary LSTR setup. As it has already been mentioned, the purge flow is delivered into the wheelspace through 24 discrete drive arm holes. These drive arm holes are placed right under the rim seal. This yields a geometry in which the possible effect of the drive arm holes jets is assumed to be maximum in the rim seal region.

The drive arm hole geometry is exchangeable by means of inserts assembled within larger diameter holes. These inserts can be exchanged without disassembling the blades and vanes of the test rig, avoiding geometry changes within the mainflow of the turbine. A description of the drive arm hole diameters used is provided in Chapter 4.2.

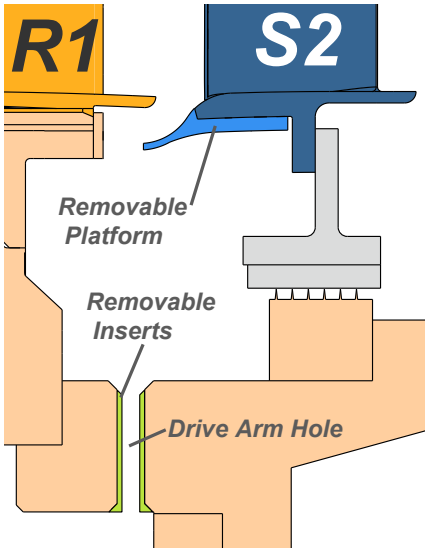

Figure 3.4: *Geometry of R1S2 wheelspace*

3.3 Instrumentation and Measurement Techniques

To examine the interaction between purge flow and main annulus flow, the LSTR is extensively instrumented. An overview of the different measurement techniques and their positions is summarized here, whereas a detailed description is provided in the following sections. However, first of all the used coordinate system is shown in Fig. 3.5, which also depicts the angle and velocity definition. In this coordinate system, the X-axis is parallel to the turbine axis. The tangential velocity component V_θ and the yaw angle γ yield positive values into the opposite direction of rotor rotation.

Next, Fig. 3.6 illustrates the location of the different measurement planes and positions in the rig, whereas their main purpose is described in the following:
In order to measure the inflow conditions of the turbine, two total pressure and two total temperature rakes are installed at MP01, which is located upstream of the first NGV row. Each of these rakes houses 10 kiel type pitot tubes or thermocouples in radial direction (see Linker [55] for more details). To check the homogeneity of the inflow, these rakes can be traversed in circumferential direction. In addition to the rakes, static pressure taps are located at the hub and the casing at MP01.

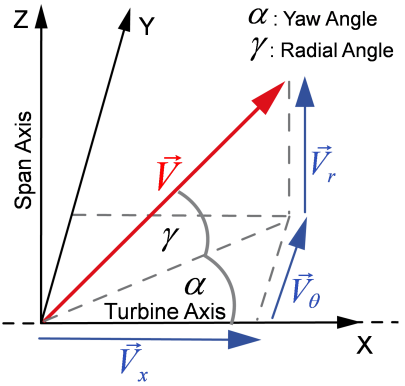

Figure 3.5: *Definition of coordinate system, flow angles and velocity components*

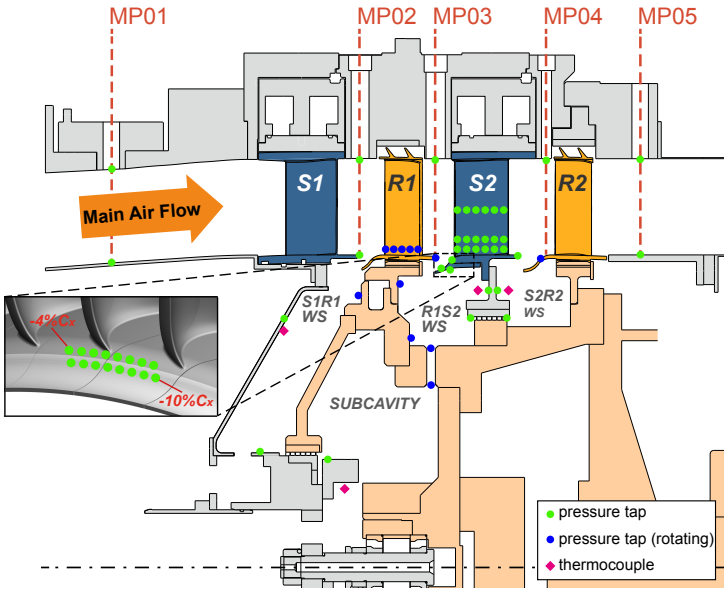

Figure 3.6: *Measurement planes and positions; adapted from Schrewe et al. [97]*

To assess the flow field between the four blade rows, 5-hole-probes have been used at MP02, MP03 and MP04. MP02 is located downstream of the first stator row. MP03 is located downstream of the first rotor row, but slightly upstream of the rim seal and MP04 is located downstream of the second stator row. The exact position of the measurement planes is provided in Tab. 3.3 as a fraction of the axial rotor or stator chord length C_x.

In addition to these discrete measurement planes in the main flow, an endoscopic PIV system allows to measure the flow field in detail at and within the rim seal. A detailed description of this measurement system is provided in Chapter 3.3.2.

However, since not only the flow field but also the propagation of the purge flow in the main annulus is of interest, sampling probes can be traversed in addition at MP03 and MP04. These probes are part of a gas concentration measurement system, which is explained in detail in Chapter 3.3.3 and allows for a tracking of the purge flow. As an alternative, temperature probes are available at MP03 and MP04, which can be used to track the purge flow if a sufficiently high difference in temperature between the two streams can be adjusted.

To assess the influence of the purge flow on the flow field within the second stator row, the vane's profile pressure distribution is measured at 5%, 20% and 50% channel height using static pressure taps with 0.5mm in diameter. At the suction side, 8 pressure taps are located at each of the three channel heights, whereas at the suction side 6 taps are present. In addition, circumferential rows of pressure taps are located at the stator 2 platform, 4% and 10% C_x upstream of the leading edge and 5% C_x downstream of the trailing edge. At each of these positions 8 taps are distributed across one vane pitch (see Fig. 3.6).

Table 3.3: *Position of the measurement planes; presented as a fraction of axial chord length (adapted from Pueblas et al. [81]).*

	$x/C_{x,S1}$	$x/C_{x,R1}$	$x/C_{x,S2}$	$x/C_{x,R2}$
MP01	3.23 ←			
MP02	→ 0.3	0.83 ←		
MP03		→ 0.46	0.35 ←	
MP04			→ 0.69	0.24 ←
MP05				→ 1.47
	←: upstream LE		→: downstream TE	

Downstream of the turbine at MP05, there are 4 total pressure and 1 total temperature rakes. Analogous to MP01 each of these rakes houses 10 kiel-type pitot tubes or thermocouples in radial direction. Together with the rakes at the inlet, the measured massflow and the torque of the shaft, these rakes are used to determine the turbine efficiency (see Chapter 5.1 for more details).

Besides the instrumentation in the main annulus, some information about the flow field within the wheelspaces is desired to study the interaction between rim seal and main annulus flow in more detail. Therefore, several pressure taps and thermocouples are located within the rotor-stator wheelspace. Their qualitative location is illustrated in Fig. 3.6. The pressure taps within the rotating frame are indicated by blue circles, whereas the ones at stationary walls are indicated in green colour. The position of the thermocouples is indicated by the rhombs. Each of the pressure taps and thermocouples is present three times in circumferential direction to assess the uniformity of the flow. In addition to their primary purpose, the non-rotating pressure taps in the wheelspace can be used with the gas concentration system to assess the sealing effectiveness, as described in Chapter 3.3.3.

3.3.1 5-Hole-Probes

Five-hole-probes are pneumatic probes used to determine the time averaged total pressure, static pressure and the flow direction at a discrete point. These values are derived from the pressure distribution at 5 different pressure tubes, which are arranged pyramidal or spherical at the probe head. In order to correlate the pressure distribution with the flow field, a calibration of the 5-hole-probe is necessary. This is usually done in a free stream wind tunnel for different flow angles and velocities. The five hole probes used at the LSTR have a cobra head with a diameter of 1.7mm and a pyramidal geometry. A picture of them is shown in Fig. A.2 in Appendix A.1.2. The calibration of the probes was carried out at the Institute's free stream wind tunnel. This calibration ranges ±30° in pitch and yaw angle and from Ma = 0.1 to 0.24 in free stream velocity. Calibration polynomial of 9th order have been used to correlate the measured data with the one obtained during the calibration. For the pressure measurements Netscanner 9816 modules from Pressure Systems with a range of 34.5 kPa and a maximum uncertainty of 17 Pa were used.

To measure the flow field over one or more passages, custom made traversing units are used. These traverse the 5-hole-probes in radial direction and rotate them around their axis. Instead of traversing the 5-hole-probes also in circumferential direction, both stator rows can be traversed in this direction by up to three passages.

A picture of the traversing units assembled at the turbine is presented in Fig. A.2 in Appendix A.1.2.

Two passages are measured per purge flow rate with a resolution of 39 radial and 31 circumferential points. The measurement grid is shown in Figure 3.7, in which the black lines at the top and bottom indicate the location of the casing and the hub side endwall. A refinement of the measurement grid within the lower 50% channel height is applied since the major effects are expected within this region. During the commissioning of the 5-hole-probes, a grid refinement study was carried out, which reveals the shown grid to resolve all relevant flow features. To save measurement time, the three 5-hole-probes have been traversed simultaneously. Further information about 5-hole-probes can be found in Nitsche [61].

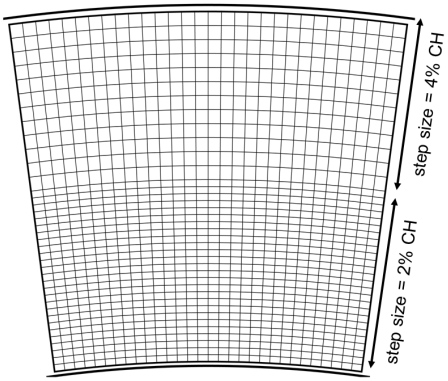

Figure 3.7: *Measurement grid of 5HP*

3.3.2 The PIV System

As already mentioned, an endoscopic PIV system is used to measure the flow field in the rim seal environment. For this measurement technique the flow is seeded with small oil particles, which are supposed to follow the flow within the turbine almost ideally. These particles are illuminated with a laser light sheet at two instants within a short period. During these illuminations two pictures are taken. Afterwards, the displacement of particle groups is calculated using a cross correlation technique. With the knowledge of the time between the pictures and geometrical constraints, the velocity and flow direction is finally examined. An advantage of the system is its capability to measure the flow field at a whole planar surface without traversing a probe. Furthermore phase locked results can be assessed. This allows in comparison to 5-hole-probes to assess the flow field at a fixed rotor or drive arm hole position. Detailed information about this measurement technique and the post processing methods are provided by e.g. Raffel et al. [86].

A drawback of a typical PIV system is the need for optical access, which is very restricted at the LSTR due to the thick turbine casing. To overcome this problem the laser light sheet is inserted with an endoscope and the pictures are taken with a

borescope. This approach has successfully been implemented at another research facility of the GLR and is described in detail by Kegalj and Schiffer [48]. A schematic installation of this technique at a turbine is illustrated in Fig. 3.8 for two different setups.

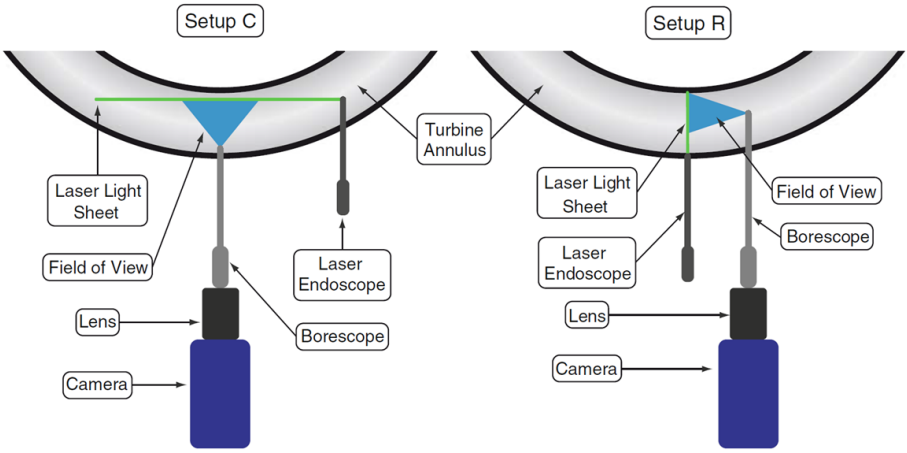

Figure 3.8: *Illustration of endoscopic PIV setups; according to Kegalj and Schiffer [48]*

The setup C uses a light sheet in axial-circumferential direction and is primarily used to measure the axial velocity V_x and the circumferential velocity V_θ. To gather in addition the radial velocity V_r, the setup R is utilised which features a light sheet in axial-radial direction. In both setups the view of the camera is perpendicular to the laser light sheet.

In the current work, a PIV system acquired from LaVison GmbH has been used. It uses a double pulsed Litron Nano L200-15 PIV Nd:Yag laser with a maximum repetition rate of 15 Hz and a maximum power of 200mJ per pulse. The used camera is a LaVision Imager Pro X 2 M CCD camera. The laser endoscope for the setup C is from ILA GmbH, whereas the one for setup R is from LaVision GmbH. The first one features a light sheet that leaves perpendicular to the endoscope axis. The borescopes are from Karl Storz GmbH featuring a viewing direction of 0° for setup C and 90° for setup R. For setup R, a 105mm macro lens is used, whereas for setup C a 85mm macro lens is used. The seeding is delivered separately into main and purge flow using two PivPart40 seeding generators from PIVTEC GmbH, providing seeding particles of approximately $1\mu m$ in diameter.

The camera with lens and borescope as well as the endoscope with light sheet optics are mounted on a grooved plate, which itself is mounted on a traversing unit (see Fig. 3.9). To avoid a contamination of the optics with seeding particles, filtered air is guided around the optics using custom made purging devices. These purging devices guarantee an almost contamination-free operation of the optics for a duration of several hours. In addition to their primary purpose of shielding the optics, the purging devices are used to fixate, stiffen and guide the endoscope and borescope on the grooved plate with the help of custom made fasteners. The grooved plate is mounted at a rigid measurement tower which houses the rest of the PIV system such as the laser, the power supply and the timing unit. The laser is connected to the light sheet optics of the endoscope using an articulated laser guiding arm. A schematic assembly of the whole system is shown in Fig. 3.9, whereas pictures can be found in Appendix A.1.3.

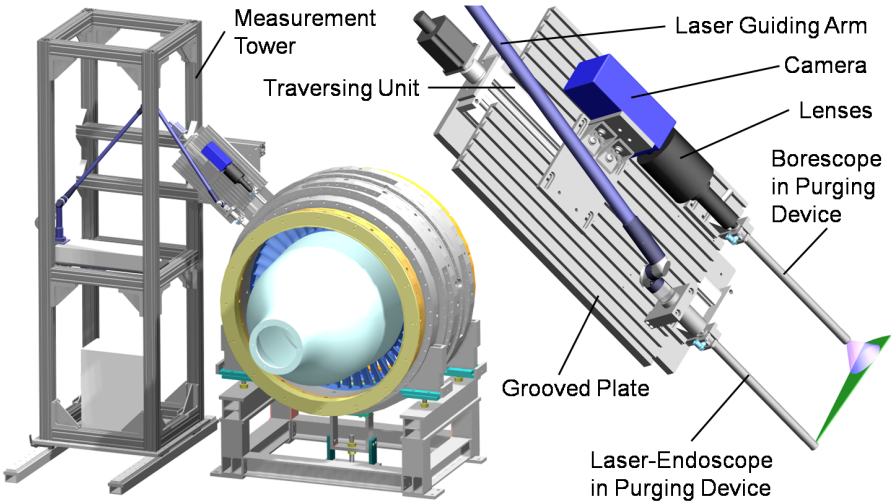

Figure 3.9: *PIV measurement tower at the LSTR*

For the measurements, the endoscope and borescope are inserted into the main flow through parallel holes in the casing by traversing the grooved plate with a stepper motor. The exact position is measured using the incremental encoder of the stepper motor and a micro switch.
The resulting propagation of the light sheet within the main annulus is exemplarily illustrated for setup C in Fig. 3.10 for two different measurement positions. The

light sheet is green coloured and the area visible with the camera is indicated by the red rectangle. On the left hand side of the figure, a situation is illustrated where the flow field within the main flow is measured. On the right hand side of Fig. 3.10 a situation is shown, in which the flow field within the rim seal is measured. In the latter situation, a part of the laser light sheet is truncated by the rotor platform, but the area within the rim seal is illuminated and measurements are feasible. However, at some channel heights, especially if the light sheet is too close to the endwall, reflections are strong and prohibit measurements. In general, it gets obvious from Fig. 3.10 that only a part of a passage can be measured with a single frame. To measure the whole passage, the stator and rotor rows are traversed together step by step by 2.5° and pictures are taken at each situation. This allows to assemble one stator pitch from three different measurement series. A whole periodic sector made up of 2 vanes, 3 rotor blades and 1 drive arm hole can accordingly be assembled from 6 different stator positions. To adjust the position of the rotor a photo-sensor has been used in conjunction with the timing unit of the PIV system.

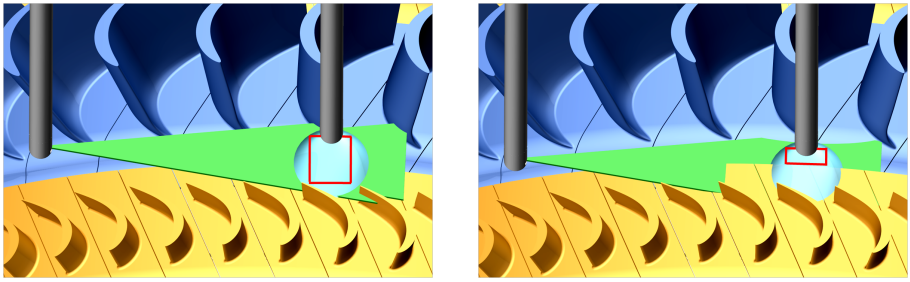

(a) *Measurement area within the main annulus*

(b) *Measurement area within the rim seal*

Figure 3.10: *Illustration of light sheet and visible area; setup C*

During the MAGPI project, measurements at **13%**, 7.2%, **3.3%**, **-2%** and -6.5% relative channel height have been conducted, whereas only the results for the positions in bold are discussed in this thesis. For all of these measurements planes, different rotor positions were measured in order to examine the influence of the rotor-stator relative positions on the interaction between purge and main annulus flow. For this purpose, the rotor was moved in 0.5° increments between the different measurement series using a trigger signal and different delay times. Ten different positions yield one rotor pitch and have been measured in the case that one stator

passage is measured. If a full periodic sector is measured, 15 different positions have been measured. The latter case ensures that the potential effect of the drive arm hole jets can be measured over the whole pitch of a stator vane.

To correlate the measured particle shift with the actual geometry of the test rig, a calibration is necessary. For this purpose, usually a calibration target with an array of points is located congruent with the light sheet at the measurement plane. With the help of the known point to point distance a geometric calibration of the pictures is possible, which also corrects image distortions due to lenses and the borescope. However, due to accessibility reasons it is not possible in the current setup to place a calibration target directly at the measurement plane. Instead, the calibration is done outside of the turbine. Afterwards, the calibrated system is inserted into the turbine without any geometry changes. During the commissioning of the test rig, this method was approved to be feasible. However, since the laser guiding arm is not ideal a slight displacement of the light sheet position can not be avoided as the whole system is moved into the turbine. The commissioning test revealed this shift to be less than 1% in channel height. This is in the order of the light sheet thickness and does not change the calibration significantly.

Another more relevant error induced by endoscopic PIV is the perspective error, which shall be explained here (similar to Raffel et al. [86]). For this purpose, Fig. 3.11 shows the schematic setup of a PIV system including the light sheet, a lens and the CCD sensor. For a better illustration of the error the thickness of the light sheet is shown larger than in reality. Within the light sheet the position of a particle is shown for two time instants, indicated with X_1 and X_2. The displacement in x-direction between the two positions is indicated by the blue vector. However,

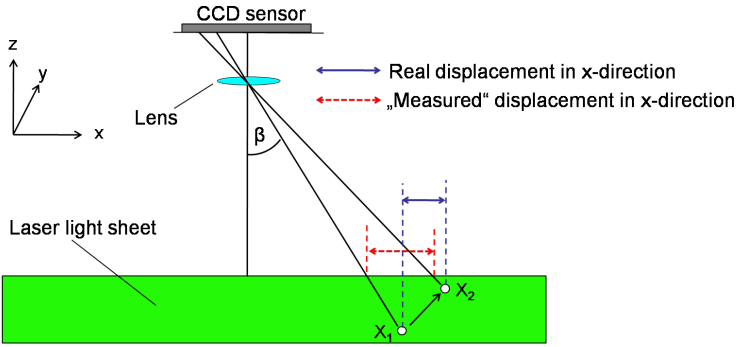

Figure 3.11: *Schematic explanation of the perspective error, adapted from Raffel et al. [86]*

the displacement observed at the CCD camera is related to the red vector and a magnification factor. If the viewing angle β is large, the difference between the real and the measured particle displacement can be significant, as illustrated in Fig 3.11. This is known as the perspective error. It is particularly large in the current setup since the distance from the borescopes to the light sheet is small to gather a sufficient light intensity. For this reason, only 2/3 of the width of a single frame is used in the current investigations in order to reduce the perspective error.

The perspective error can be corrected if the exact geometry of the experimental setup and the velocity perpendicular to the light sheet is known. However even if this is not possible, the flow structure is in general not changed significantly by the perspective error as shown by Raffel et al. [86].

3.3.3 The Gas Concentration System

If the purge flow is seeded with a tracer gas of similar properties, its propagation in the main flow can be assessed by tracking this gas with a sampling probe and a gas analyser. Furthermore, these measurements allow to assess the sealing effectiveness within the rotor-stator wheelspace and the potential cooling effect of the purge flow at the stator 2 endwall and profile, as it will be shown below. For this reason, gas concentration measurements were conducted at the LSTR to enhance the investigation of the interaction between purge and main annulus flow. As tracer gas, CO_2 was used since it is non-toxic in the used concentration, non-reactive, non-explosive and can easily been purchased.

For these measurements a steady difference of the CO_2 concentration in the purge flow and the main flow is necessary. While the elevated CO_2 concentration in the purge flow can be achieved by an injection of pure CO_2, the generation of a steady CO_2 concentration in the mainflow is more complex. Due to the closed loop design of the test rig, any injection of CO_2 leads to a continuous rise of the CO_2 concentration in the whole system. To overcome this problem, the LSTR is redesigned to a “partly open” configuration. In this configuration, a part of the main flow is drawn out of the test rig using the secondary air blower (yellow pipes in Fig. 3.1). Simultaneously, fresh air is sucked into the test rig upstream of the primary air blower. Now, if the mass of exhausted CO_2 is equal to the mass of CO_2 seeded into the purge flow, a stationary CO_2 concentration in the main and the purge flow is achieved, featuring a sufficient difference to carry out measurements. With this difference in CO_2 concentration, a mixing concentration η_{CO_2} can be assessed at a desired measurement point. This mixing concentration refers the

measured CO_2 concentration y to the concentration within the purge flow and the one within the main annulus, upstream of the purge flow injection. It simply states whether only main annulus fluid ($\eta_{CO_2} = 0$), only purge flow ($\eta_{CO_2} = 1$) or a mixture of both ($0 < \eta_{CO_2} < 1$) is present.

$$\eta_{CO_2} = \frac{y - y_{MF}}{y_{PF} - y_{MF}} \tag{3.1}$$

Is the mixing concentration measured with a sampling probe downstream of the stator at MP04, it can be used to "visualise" the propagation of the purge flow in the main annulus and hence allows a tracking of the purge flow. Similarly, the static pressure taps at the vane and platform can be used to extract a small proportion of fluid in order to "visualise" the propagation of the purge flow along the surface.
Even though this visualisation of the purge flow propagation is the primary interest in this work, the mixing concentration can also be used to assess the potential cooling of the vanes. If the following restrictions are met,

- Incompressible flow
- Constant fluid properties
- Ideal gas
- Newtonian fluid
- Inertness of the mixed gases
- Negligible volume forces
- Thermo diffusion (Soret effect) and thermal diffusion (Dufour effect) are neglected

the Reynolds averaged transport equations for temperature and mass fraction (=concentration) are similar (see Jung [45], Eckert [21] or Lerch [54]). This so-called "analogy between heat transfer and mass transfer" is often used in film cooling applications. It yields that the adiabatic film cooling effectiveness η_{aw} can be obtained from concentration measurements, if the adiabatic wall is replaced by an impermeable wall and the following two restrictions are satisfied: First the turbulent transport mechanisms need to be dominant in relation to the molecular transport mechanisms, what is however accepted for typical film cooling configurations according to Jung [45]. Second, the turbulent Prandtl number Pr_t has to be equal to the turbulent Schmidt number Sc_t. As stated by Eckert [21] and Jischa [40], this is also met in general applications. This leads to the following relationship, which

links the adiabatic film cooling effectiveness η_{aw} to the above mentioned mixing concentration η_{CO_2}, measured at the wall:

$$\eta_{aw} = \frac{T_{aw} - T_{MF}}{T_{coolant} - T_{MF}} \quad \widehat{=} \quad \eta_{CO_2} = \frac{y_{wall} - y_{MF}}{y_{PF} - y_{MF}} \tag{3.2}$$

In the current configuration it is assumed that the transport mechanisms in the rim seal environment and the nearby blade surface are also dominated by turbulent transport mechanisms. Therefore, it seems reasonable to apply the analogy between heat and mass transfer also to rim seal flows. A verification of this has recently been carried out by Boutet-Blais et al. [8] and yields in general good results. This finally provides the possibility to assess the adiabatic cooling effectiveness η_{aw} at the surface of the stator by gas concentration measurements, as it has already been done by Popovic and Hodson [78] in a linear cascade. As η_{aw} allows in addition to the "visualisation" of the purge flow propagation a quantification of its cooling potential, this value is used during the discussion of the results obtained at the surface of the vanes. As there is no film cooling applied in the current configuration, η_{aw} is just referred to as the adiabatic cooling effectiveness to avoid any confusion with film cooling experiments.

If the mixing concentration is measured in the rotor-stator wheelspace using the local pressure taps, it can be used to assess the amount of ingested main flow. It is in this case congruent to the sealing effectiveness η_s, which is typically utilised in the open literature to determine the rate of hot gas ingestion (see Chapter 2.2.1). For this reason, η_s is used instead of η_{CO_2} during the discussion of the results in the wheelspace in order to maintain the established notation.

To measure η_{CO_2}, η_{aw} or η_s, the coolant flow 2 in Fig. 3.2 is seeded with CO_2 in a way that a concentration of approximately 15000ppm is obtained. The concentration of the annulus fluid is adjusted to a value of approximately 3000ppm by controlling the exchanged mass flow. The CO_2 concentration is measured with a four channel Emerson X-Stream gas analyser. These four channels allow to measure at two desired measurement points and at the reference within the purge flow and the main flow simultaneously. To measure the reference concentration of the main flow, fluid is extracted from one of the total pressure rakes at MP01. To assure that the main flow is fully mixed out with the injected fresh air at this position, the homogeneity of the CO_2 distribution was checked beforehand in radial and circumferential direction. Yet, no significant inhomogeneity was found, so that the measured concentration at MP01 is representative of the main annulus. The reference concentration of the purge flow is measured in the subcavity and/or the delivery pipes using static pressure taps, whereas the unseeded flow across the

labyrinth seal from the S1R1 wheelspace into the subcavity is taken into account. To measure the CO_2 concentration in the main flow at MP04, a sampling probe is used which shares its measurement grid with the 5-hole-probes. This allows to correlate the results from the gas concentration measurements with the measured flow field. In order to reduce measurement time and CO_2 consumption, a probe with two heads was used (see Fig. A.2 in Appendix A.1.2). To account for the delay time needed to purge the connection tubes, filters and analyser, a sufficient waiting time is taken into account prior to each measurement, which was assessed from step response tests (for both, sampling probe and pressure taps).
A possible error during the assessment of η_{aw} and η_s may arise from the fact that a small proportion of the fluid close to the wall is extracted through the pressure taps at the surface. Hereby, also fluid that is located further away from the wall may be drawn into the measurement system, leading to a measured concentration that is not representative of the one at the wall. This effect has been studied by Pederson [72], who investigated the influence of the suction rate $V_{suction}/V_\infty$, the fluid is extracted with. He concludes from experiments at a flat plate, that the allowable suction rate to determine true values depends strongly on the flow field. Whereas for some cases $V_{suction}/V_\infty = 0.5$ leads to accurate results, other cases with separation zones require very small suction rates in the order of $V_{suction}/V_\infty = 0.03$. For this reason, the only possibility to check whether a falsification of the results occurs in the current configuration is to carry out experiments with a variation of the suction rate. This has been done by an adjustment of the gas analyser through-flow to different values and a comparison of the different results. Since there is no significant difference detectable (see Figure A.5 of Appendix A.3), it can be concluded that the extraction of fluid does not influence the results.

3.4 Numerical Simulation of the Experimental Setup

Even though the main objective of this work is to investigate the interaction between purge and main annulus flow experimentally, in parallel numerical simulations have been performed by the MAGPI partners and Gregor Schmid, a colleague at the Institute of Gas Turbines and Aerospace Propulsion. During the discussion of the experimental results, some of these numerical results will be shown to improve the understanding of the observed effects. A description of the computational setup including the mesh generation, flow models and validation results is presented in Schmid et al. [95]. All numerical results shown in this thesis are taken from the simulations described in this publication.

4 Rig Operation and Test Matrix

In order to study the interaction between the purge and the main annulus flow, experiments have been carried out for different purge flow rates and drive arm hole diameters. In this chapter an overview of the different test cases and the basic approach of the rig operation is presented.

4.1 Rig Operation

During the operation of the LSTR, the turbine inlet and purge flow temperature is adjusted continuously to 40°C using water driven heat exchangers. However, the pressure in the system varies during rig operation and especially between different measurement days due to changes in ambient conditions. To account for such changes, the Reynolds or Mach number is in general kept constant in test rigs, whereas the choice depends primarily on the question whether viscous or compressible effects are of major interest. Even though the LSTR is operated at subsonic conditions, it was decided to keep the Mach number constant. The reason for this is that a variation of the Mach number would alter the velocity triangles and thus the loading of the blades, as shown by Linker [55]. Since the loading of the blades influences the flow field and the losses generated in the turbine, any change should be avoided during rig operation. This is done by a continuous control and adjustment of the reduced mass flow $\dot{m}_{red}$ and the reduced spool speed n_{red}. These values are defined according to Henecke and Wörrlein [33] as follows:

$$\dot{m}_{red} = \frac{\dot{m}\sqrt{R\,T_t}}{A\,p_t}; \qquad n_{red} = \frac{n}{\sqrt{R\,T_t}} \tag{4.1}$$

A drawback of this method is a change of the Reynolds number during different rig runs. However, this change is small and should not alter the ratio between inertial and viscous forces significantly as the Reynolds number is at sufficiently high, engine representative values ($Re_{MF} > 300.000$).
During rig operation, $\dot{m}_{red}$ and n_{red} are assessed at the inlet of the turbine. This means that the inflow conditions at the first stage are not changed between different purge flow rates. In contrast, the operating point of the second stage is

altered slightly due to the increased mass flow downstream of the R1S2 rim seal. However, this change is revealed to have a small effect on the results, as shown in Chapter 6.1.1 exemplarily by measurements of turbine efficiency.

4.2 Test Matrix

During the MAGPI project, experiments have been carried out for the design point (DP) and an off-design point (ODP) of the turbine, whereas in this thesis only results for the design point are presented. At this point, the purge flow upstream of the second stator row has been varied in seven steps, ranging from an ingestion case of $IR = -0.28\%$ to an egress case of $IR = 1.5\%$. A particular purge flow rate is the one at IR = 0.3%, as it is according to the industrial partner ITP representative of a low pressure turbine. The higher values are known to be in excess of engine representative values for low pressure turbines, but are useful to investigate the effects of the purge flow in more detail. Furthermore, they are in the range of values used in common high pressure turbines and thus allow for a comparison with other test cases presented in the open literature. In addition to the varied purge flow upstream of the second stator row, a constant purge flow was supplied upstream of the first and the second rotor row. This was set to $IR = 0.5\%$ upstream of rotor 1 and to $IR = 0.3\%$ upstream of rotor 2.
All the injection rates have first been tested for the so-called baseline drive arm hole configuration, featuring a hole diameter of 8.5mm. This diameter was specified by the MAGPI partners according to the following compromise: On the one hand, design restrictions of the rig and an adequate interchangeability of the drive arm hole inserts, which are described in Chapter 3.2, has been taken into account. On the other hand, the velocity ratio between the drive arm hole jets and the wheelspace flow shall be in the range of engine representative values for the engine representative purge flow rate. Furthermore, it was checked by the use of preliminary CFD calculations that a sufficiently high penetration depth of the drive arm hole jets is present to influence the flow field within the rim seal. But, this was primarily ensured by the choice of the comparably high injection rates.
To velocity ratio between the drive arm hole jets and the wheelspace flow can be defined by the following equation:

$$J = \frac{W_{jet}}{W_{WS}} \tag{4.2}$$

This equation corresponds to the effective velocity ratio J_e, which has been presented in Equation 2.8, if the density of the drive arm hole fluid and the wheelspace fluid

are assumed to be equal. For this reason, it is one of the main parameters that influences the penetration depth and the trajectory of the drive arm hole jets.
To calculate J, the jet velocity can be taken from the Rolls-Royce flow network solver SPAN. However, due to a lack of data for the velocity of the fluid in the wheelspace, an assumption is necessary for this value. For this purpose, it is assumed that the fluid within the wheelspace rotates at approximately half the rotor speed in circumferential direction. This is a common assumption in the open literature (see e.g. Chilla et al. [14]) which simplifies Equation 4.2 to the Equation 4.3, in which r_{DA} is the outer radius of the drive arm.

$$J = \frac{W_{jet}}{0.5\,\omega\,r_{DA}} \tag{4.3}$$

For this simplified equation it needs to be mentioned that the latter assumption of the wheelspace velocity is rather imprecise because the tangential velocity and hence the swirl in the wheelspace is influenced by the injection rate itself. Also the assumption of a constant density in the wheelspace and the delivered coolant flow is not perfectly fulfilled, especially for the highest injection rate, but the error is expected to be less than 8%. Nevertheless, due to a lack of more precise data, Equation 4.3 is used to assess the velocity ratio. Furthermore, this definition has been used during the MAGPI project by the industrial partners to compare the velocity ratio of the current configuration with engine representative values.
An overview of the injection rates tested is provided in Table 4.1, in which the values of mass flow and spool speed are referenced to ISA inlet conditions. For completeness, also the drive arm hole velocity ratio J is provided, whereas the latter one is indicated for the baseline configuration by $J\varnothing\ 8.5\ mm$. For each purge flow rate in Table 4.1, all measurement techniques presented in Chapter 3.3 have been applied with two exceptions: The gas concentration measurements have not been carried out for the smallest IR, since in this case no external fluid enters into the wheelspace that can be seeded with CO_2. The PIV measurements have only been carried out for the injection rates indicated in bold because of a limited availability of the PIV system. For the same reason a full periodic sector, consisting of 2 stator vanes, 3 rotor blades and one drive arm hole, has only been measured for IR = 0.3% and IR = 1.5%.
To assess the influence of drive arm hole jets on the flow field within the main flow and wheelspace independent from the purge flow rate, a second measurement campaign has been carried out. For this purpose, the velocity ratio and hence the penetration depth of the drive arm hole jets is changed, but the overall injection rate is kept equal to the baseline configuration. This allows to study solely the

Table 4.1: *Overview of the operation point and the tested purge flow rates upstream of S2 for the baseline drive arm hole configuration with 8.5mm diameter and the second measurement campaign with 11.6mm diameter*

OP	$\dot{m}_{ISA}$	n_{ISA}	IR	$J\varnothing$ 8.5 mm	$J\varnothing$ 11.6 mm
			-0.28 %	0.1	0.1
			-0.1 %	1.5	0.8
			0.3 %	4.4	2.4
DP	13,7 kg/s	741 rpm	0.5 %	5.8	3.2
			0.75 %	7.5	4.2
			1 %	9.0	5.1
			1.5 %	11.6	6.9

influence of the drive arm hole jets. As an influence of the drive arm hole jets is already present for the baseline configuration, the velocity ratio has been reduced by increasing the drive arm hole diameter. This yields in addition values of the velocity ratio, which are closer to engine representative values for the higher injection rates. Taking the geometrical constraints of the rig into account, the average drive arm hole diameter [1] of the second measurement campaign was set to 11.6mm, which reduces the velocity ratio by about 40-46%. The drive arm hole velocity ratio ratios $J\varnothing$ 11.6 mm for this second measurement campaign are presented on the right hand side of Table 4.1.

For this second measurement campaign no PIV has been conducted. Nevertheless, a large number of CO_2, 5-hole-probe, pressure and efficiency measurements have been carried out which allow to assess the influence of the change in drive arm hole diameter.

[1] 21 of the 24 drive arm hole inserts were removed, leading to a hole diameter of 12mm. However, 3 of the 24 inserts could not be removed due to instrumentation issues and were kept at 8.5mm. This leads to an area averaged diameter of 11.6mm which was used for the SPAN calculations and the assessment of the velocity ratio.

5 Data Evaluation Methods and Measurement Errors

This chapter specifies the definitions used for the presentation of the results. This allows to examine the results without too many equations and is intended to improve the readability of this thesis. In special cases also the post-processing of the data and their physical meaning is explained. All the fluid properties necessary to assess the results are taken from the VDI Wärmeatlas [108]. If feasible, also the errors of the different measurement techniques are provided.

5.1 Determination of Turbine Efficiency

To evaluate the turbine efficiency, the purge flow needs to be taken into account. The most straightforward method to do this is to use the first law of thermodynamics and compare the real process with the isentropic process. This yields for an adiabatic turbine the following equation in which the isentropic condition is indicated by a bar over the symbol. This definition assumes for the isentropic process in the denominator that each flow "i" is expanded separately from its inlet condition to the mixed out exit condition of the turbine.

$$\eta_{is} = \frac{\sum_i (\dot{m}_{in(i)} h_{t,in(i)}) - (\dot{m}_{ex} h_{t,ex})}{\sum_i (\dot{m}_{in(i)} h_{t,in(i)}) - (\dot{m}_{ex} \bar{h}_{t,ex})} \tag{5.1}$$

Replacing the nominator by the measured shaft power, assuming an ideal gas and using isentropic relations in the denominator, the equation can be re-written to:

$$\eta_{is} = \frac{M_{shaft}\,\omega}{\sum_i (\dot{m}_{in(i)} c_p T_{t,in(i)} [1 - (\frac{p_{t,ex}}{p_{t,in(i)}})^{\frac{R}{c_p}}]} \tag{5.2}$$

A drawback of this efficiency definition is the necessity to know the total pressure of the purge flows at the specified control volume. However, in the test rig only

the static pressure at the stationary walls in the rotor-stator wheelspace is available and can be used as an inlet condition. As it will be shown in Chapter 6.1.3, the static pressure in the R1S2 wheelspace decreases with increasing purge flow due to increased tangential velocities within the wheelspace. The total pressure in contrast is assumed to be approximately constant. This leads to the fact that the efficiency calculation using the measured static pressures as an inlet condition would underestimate the efficiency drop due to the purge flow injection.
To overcome this problem of the unknown purge flow delivery pressure, the MAGPI partners have employed the following efficiency definition:

$$\eta_{MAGPI} = \frac{M_{shaft}\ \omega}{c_p \left(\dot{m}_{eff}\, T_{t,eff}\right)\left[1 - \left(\frac{p_{t,MP05}}{p_{t,MP01}}\right)^{\frac{R}{c_p}}\right]} \tag{5.3}$$

using

$$\dot{m}_{eff}\, T_{t,eff} = \dot{m}_{MP01} T_{t,MP01} + PS\left(\dot{m}_{S1R1}\, T_{t,S1R1} + \dot{m}_{R1S2} T_{t,R1S2}\right) \tag{5.4}$$

This definition assumes that the purge flow is injected into the main annulus at approximately the total pressure of the main flow at the same axial position, but accounts for the actual purge flow temperature. For this purpose, a power split factor PS is used which defines the fraction of the rotor 2 power in relation to the overall turbine power. It has been assessed by the industrial partners to be 0.5 using CFD simulations. In Equation 5.3, it is also assumed that the purge flow injection downstream of a stator row does not contribute to the work extraction in the subsequent rotor row, as it is frequently postulated (see e.g. Kurzke [51]). Even though this assumption is debatable and depends on the definition of the ideal process, it is not relevant in the current work since these purge flows are kept constant and the efficiency changes are presented relative to each other.
All in all, the efficiency definition given in Equation 5.3 seems to provide more realistic values and also agrees better with numerical results. For this reason it is used in this thesis. Nevertheless, for completeness the values calculated with Equation 5.2 are presented for the interested reader in Appendix A.2.
To examine the turbine efficiency with Equation 5.3, the total temperature and total pressure at the inlet and exit of the turbine are measured using rakes at MP01 and MP05 (see Section. 3.3). According to Cumpsty and Horlock [15], a mass flow averaging of total temperature and a work averaging of total pressure would be appropriate to assess representative values at the inlet and the exit. However, due to a lack of measured static pressures within the main annulus at MP01 and MP05,

this is not possible without any assumptions of the static pressure distribution. For this reason, all values of total temperature and pressure have been area averaged. For the measured shaft torque M_{shaft} a correction is necessary because the main bearing of the test rig is located between the turbine and the torquemeter and thus influences the torque measurements. This is done by the use of experimental data which have been obtained during the commissioning of the LSTR. During these tests the rig has been driven without rotor blades and the outer casing of the turbine for various spool speeds and bearing temperatures. In this case the measured shaft torque represents the bearing losses and the windage losses of the discs at the present spool speed and bearing temperature. For the efficiency measurements, this value is added to the measured torque, whereas the actual bearing temperature and spool speed is taken into account. This finally corrects for the bearing losses and determines the torque without windage losses. The latter case is often beneficial for a comparison with numerical data as these usually do not include all the rotor discs in their numerical domain. Axial forces due to the rotor are not compensated for by this approach and are therefore neglected.

$$M_{shaft} = M_{measured} + M_{windage} + M_{bearing} \tag{5.5}$$

Using a Gaussian error propagation method, the absolute accuracy of the efficiency measurements is assessed to 1.3% for the design point of the MAGPI configuration (for details see Linker [55]).

5.2 Evaluation of Aerodynamic- and Loss Related Coefficients

In this section, the aerodynamic- and loss related coefficients are defined. These parameters are primarily obtained from the 5-hole-probes, static pressure taps at the surface of stator 2, or a combination of both.

5.2.1 Mach Number

Even though the flow within the main annulus can be assumed incompressible, the Mach number is used in the present work to emphasize the “velocity” obtained from the five-hole-probe measurements. The reason for this is that the Mach number can be calculated solely from 5-hole-probe data and omits the necessity of temperature measurements, which have not been carried out for all purge flow rates and measurement planes. In this thesis, it is calculated according to Eqn. 5.6, using the ideal gas law. The expression is only valid in case of incompressible flow.

$$Ma = \frac{V}{a} = \sqrt{\frac{2p_{dyn}}{\rho}} \frac{1}{\sqrt{\gamma R T_s}} = \sqrt{\frac{2p_{dyn}}{p_s \gamma}} \tag{5.6}$$

5.2.2 Pressure Loss Coefficient

To quantify the losses in total pressure across the second stator row a pressure loss coefficient ζ is defined. This value uses the total and dynamic pressure at 50% channel height upstream of the stator vane at MP03 as a reference value to assess and nondimensionalise the measured losses:

$$\zeta = \frac{p_{t,MP03} - p_{t,MP04}}{p_{dyn,MP03}} \tag{5.7}$$

Due to the missing information of the purge flow delivery pressure at the exit of the rim seal, a change in this value is not taken into account and the pressure loss coefficient is just calculated between MP03 and MP04.

5.2.3 Profile Pressure Distribution

The profile pressure distribution at the stator 2 vane is presented in this work using a pressure coefficient C_p, defined as:

$$C_p = \frac{p_s - p_{s,MP03}}{p_{dyn,MP03}} \tag{5.8}$$

The reference static pressure $p_{s,MP03}$ and dynamic pressure $p_{dyn,MP03}$ are taken upstream of the vane at MP03. As it will be shown in Chapter 6.1.2, the flow field at this measurement plane is already influenced by the purge flow injection, especially close to the hub. This possibly influences the C_p distribution, even though there might be no change in the flow across the vane. To eliminate this effect, the reference values to nondimensionalise the pressure are taken at 27% channel height. At this channel height there is almost no change in the reference values between different purge flow rates (see e.g. Mach number distribution in Fig. 6.2). This gives the advantage that the C_p value yields purely the change in vane loading, originating from the altered flow field at different purge flow rates.

5.2.4 Platform Pressure Distribution

The platform pressure distribution at the stator 2 is defined by the coefficient k_p.

$$k_p = \frac{p - p_{av,1-8}}{q} \qquad using \qquad q = \frac{\rho \omega^2 r_{Hub}^2}{2} \tag{5.9}$$

This coefficient plots the pressure with respect to the mean value of the 8 pressure taps located at the same axial location. Afterwards, the pressure is non-dimensionalised by the "dynamic pressure" built with the hub speed of the rotor [1], as it is also done by Johnson et al. [41]. This definition allows to measure the steady-state pressure variations that are caused for example by blockage effects of the stator 2 leading edge. Both, the amplitude of the pressure variation as well as the phase angle with respect to e.g. the leading edge position can be observed.

5.3 Evaluation of Data from the Gas Concentration Measurements

As explained in Chapter 3.3.3, gas concentration measurements are used to determine the mixing concentration η_{CO2} at MP04. In addition, the adiabatic cooling effectiveness at the surface of stator 2 and the sealing effectiveness within the wheelspace are assessed. Since these parameters have already been defined in Chapter 3.3.3, only the measurement accuracy is stated here. This depends on the measurement location, because gas analyser channels with different measurement ranges have been used at different positions in the turbine. This allows to reduce the measurement error at locations with low CO_2 concentrations. Using a Gaussian error propagation method, the measurement accuracy of η_{CO2}, measured at MP04, is assessed to be 1.4%. The error for η_{aw} and η_s is assessed to be max. 2.8%.

5.4 Evaluation of Data from the PIV Measurements

The processing of the PIV data is carried out with the software DaVis 7.2 from LaVison GmbH using a cross correlation technique. A multi pass correlation ranging from a window size of 128 x 128 pixel to 64 x 64 pixels is applied with an overlap of 75%. The latter window size ensures 10-15 particles per interrogation window, which is in accordance to Keane [47] a sufficient number to get reliable results. If

[1] This is the dynamic pressure at the hub side endwall at the upstream measurement plane

not stated otherwise, 750 double frames have been recorded and postprocessed. This number has been determined during the commissioning of the rig to get reliable results. No peak locking effect could be observed.

A major issue during the post-processing are reflections at the endwall. The platform wedge face gaps between single blades have been filled with white silicon material. This leads to strong reflections in this area. In addition, a very thin layer of silicon has been spread all over the platforms during assembly. Even though the blades have been cleaned carefully afterwards, some small irregularly distributed spots of silicon material are still present at the platforms and alter their position during rig operation. This leads to additional reflections, which are similar in size and structure compared to the signal gathered from the seeding particles. All in all, these reflections disturb the processing of the data and lead to false vectors.

To overcome this problem, an average image has been generated from the 750 images and is subtracted from each single image. This reduces reflections significantly. In addition, masks have been applied in the area of remaining reflections by visual inspection. For the PIV setup with a light sheet in circumferential direction (setup C), a further filter has been applied if measurements in the main annulus are evaluated. This filter ignores vectors possessing a circumferential velocity component V_θ larger than 93% of the rotor speed in rotor rotational direction. These vectors are caused primarily by silicon spots that move in congruence with the rotor and thus need to be ignored. This is illustrated in Fig. 5.1 which shows the rotor at two different time instants, indicated by the red and the black shape. The movement of a seeding particle is illustrated by the blue vector whereas the displacement of a silicon spot is illustrated by the red vector. It is obvious that the vectors originating from silicon spots can be filtered out by the criterion given above. Nevertheless several tests have been carried out to check whether the filter has any influence on the general flow field, but no significant influence is observed. For the setup C measurements within the rim seal, this filter has not been applied since the flow above the rotor platform is not measured and hence not post-processed. Finally, missing vectors within masked areas have been interpolated from surrounding vectors. Since the masked out regions

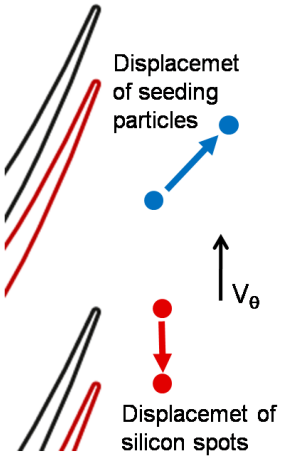

Figure 5.1: *Illustration of particle and rotor movement*

are small compared to the whole measurement area, this approach is appropriate and simplifies the visual examination of the results.
Exemplarily Fig. 5.2 shows a processed image for different post-processing settings. On the left hand side, the default settings of the DaVis software are applied, whereas on the right hand side all pre- and post-processing schemes described above are used. For a better orientation the trailing edges of the first rotor row are visualised on the left hand side and a leading edge of the second stator row is visualised on the right hand side. In both pictures the in-plane velocity $V_{x\theta}$ is presented. In the left picture, the spurious vectors pointing in rotor rotational direction are clearly visible. In addition, the poor correlation right on top of the gaps between single blades is obvious. On the right picture, the processing of the data is significantly improved and allows to study the different flow features. As it has already been explained in Chapter 3.3.2, several measurements at different stator positions need to be assembled to gather the flow field of a full stator passage. For this purpose, the area indicated by the dashed rectangle in Fig. 5.2 b is used for each stator position. Since the light sheet is inserted from the bottom of the picture, this lower area features a higher intensity of laser light and thus offers a better signal to noise ratio.

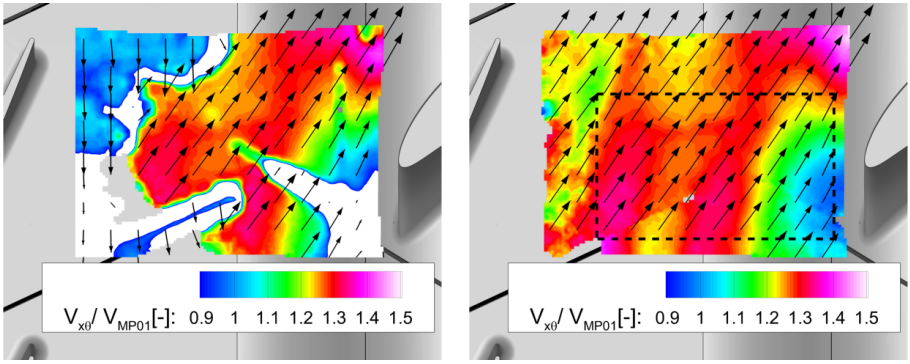

(a) PIV result with default settings *(b) PIV result with improved settings*

Figure 5.2: *Processing of a single PIV image with different settings*

The measurement error of the PIV system is in general made up of two components. Within the main flow, where flow normal to the laser light sheet is small, the error depends basically on the resolution of the minimum detectable particle shift. Assuming sub pixel accuracy, this resolution is in accordance to Westerweel [111] assessed to approximately 0.3 pixel, leading to a measurement error of 3-4% for the

setup C measurements, which feature a particle shift of 8-10 pixels. For the setup R measurements this measurement error is 4-15% since the obtainable particle shift is smaller, whereas the larger errors occur within the rim seal.
At regions of pronounced secondary flows or in the rim seal, flow normal to the laser light sheet is not negligible. This leads in addition to the measurement error described above to a significant influence of the perspective error which has been described in Chapter 3.3.2. This error is hard to assess since the exact velocity normal to the light sheet is unknown. Considering geometrical constraints and the gathered results, this error is expected to rise up to 30% at the edges of the measurement frames. In this thesis, the perspective error is not corrected because of the following two reasons: On the one hand, the correction would not change the general effects assessed in this thesis and thus, there is no additional knowledge acquisition expected from it. On the other hand, there is only a limited number of radial measurement planes available which yield the velocity normal to the measurement plane. This would make a correction coarse and error sensitive. Furthermore, these radial measurement planes also suffer a perspective error, falsifying the correction itself.

5.5 Determination of Mixing Losses

As it has already been mentioned during the literature review in Chapter 2.2.3, mixing losses occur if purge flow is injected into the main flow. An equation to quantify mixing losses is provided by Denton [19] in terms of entropy creation Δs.

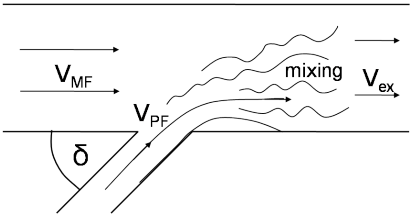

$$\Delta s = \frac{\dot{m}_{PF}}{\dot{m}_{MF}\, T_t} \left((V_{MF})^2 - V_{MF} V_{PF} cos\delta \right) \tag{5.10}$$

Figure 5.3: *Mixing of two streams; adapted from Denton [19]*

In this equation, it is assumed that the stagnation temperature of the main flow and the mixed flow is equal, as it is approximately the case in the current configuration. It is further assumed that the coolant flow is small compared to the main flow and that it is injected under a constant angle δ as illustrated in Fig.5.3.

6 Results

In this chapter the results obtained from the measurements at the LSTR are presented. For this purpose, first the results from the efficiency measurements are shown which determine the global influence of the purge flow injection. Afterwards, a detailed investigation of the flow field at several locations in the turbine is presented. The latter one provides on the one hand reasons for the measured efficiency decrease. On the other hand, it yields a detailed insight into the flow phenomena caused by the purge flow injection. All these results will first be shown for the baseline configuration, using the drive arm hole diameter of 8.5mm.
In order to study whether there is any difference between the purge flow injection upstream of a rotor row and upstream of a stator row, the results are compared wherever applicable with results found in the open literature. Afterwards, aspects that are similar or contrary to the purge flow injection upstream of a rotor row will be highlighted and discussed.
In addition, effects that have not been presented in the literature so far are further examined. This is for instance the influence of the drive arm hole jets on the flow field within the rim seal and main flow. For this purpose, also results from the measurements with the larger drive arm hole diameter will be presented and discussed.
Some of the presented results have already been published in Schrewe et al. [96], [97], Pueblas et al. [81], Linker [55] and Schmid et al. [95], but will be shown again in this work in order to get a complete overview of the effects observed.

6.1 Results for Baseline Drive Arm Hole Configuration

6.1.1 Influence of Purge Flow on Turbine Efficiency

To assess the influence of the purge flow on turbine efficiency, measurements have been carried out for seven purge flow rates. The results are shown in Fig. 6.1 a. The efficiency is calculated according to Equation 5.3 given in Chapter 5.1 and presented relative to the case with the lowest purge flow rate. Data sets from five different measurement days as well as the arithmetic mean line are shown. Overall,

a good repeatability between the different measurement days is obtained which is in the range of 0.1%.

Examining the efficiency at different purge flow rates, it shows in general a decreasing characteristic. As the injection rate *IR* is increased from -0.28% to 1.5%, the efficiency decreases by 0.6%. In parallel to this efficiency drop, a slight shift in the operating point of the turbine is observed due to the additional mass flow delivered by the purge flow. For instance, the area averaged total pressure ratio across the turbine has been increased by 0.6% if the purge flow is increased from -0.3% to 1.5%. To evaluate if this shift in the operating point has any influence on the turbine efficiency, additional measurements have been carried out with a variation of the main annulus flow only. Figure 6.1 b shows the results of these measurements. Since only a variation is observed which is within the repeatability of the efficiency measurements, it can be concluded that the efficiency drop originates primarily from the purge flow injection and not from the changed operating point.

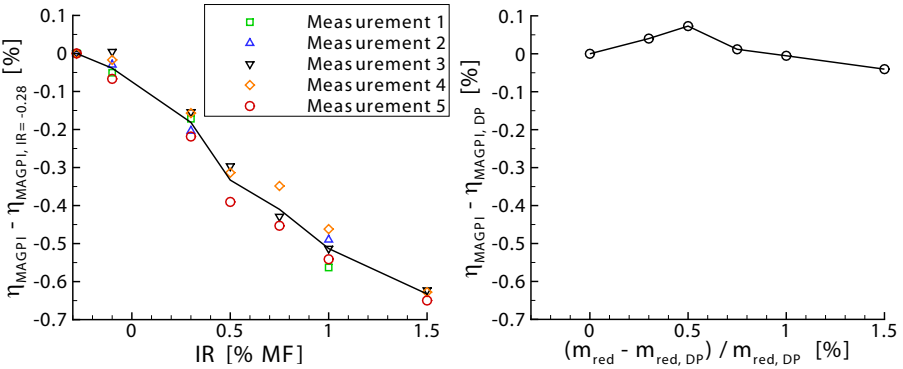

(a) Turbine efficiency for different IR *(b) Turbine efficiency for a varied OP*

Figure 6.1: *Efficiency measurements; Design Point.*

To identify the reasons for the efficiency decrease, detailed results from the flow field measurements will be presented in the following sections. This improves the general understanding of the purge flow induced effects. Furthermore, it allows to detect several possible loss sources, which will be highlighted during the discussion of the results.

6.1.2 Influence of Purge Flow Injection on the Main Annulus and the Rim Seal Flow

In this section the influence of purge flow injection on the flow field at different locations in the turbine is investigated. First, the results upstream of the rim seal at MP03 are presented. Thereafter, the flow field downstream of the second stator row at MP04 is examined. Finally, the flow field at and within the rim seal is analysed, followed by the one within the stator 2 passage.

Flow Field Upstream of the Rim Seal Region

To study if the purge flow has any effect on the main flow upstream of the rim seal region, 5-hole-probe measurements have been carried out at MP03, which is located slightly upstream of the rotor platform trailing edge (see illustration in Fig. 6.2). Circumferentially averaged values of the Mach number, the yaw and radial angle are presented in Fig. 6.2 for four different purge flow rates. Observing the Mach number distribution, a deceleration of the flow is examined between 0% and 20% channel height in case the purge flow is increased. In contrast, the fluid is accelerated slightly in the outer part of the channel. This suggests that the seal air acts as a blockage in the main flow. This provokes a redistribution of the main flow towards the outer casing of the turbine as it can be seen by the radial angle γ, which yields larger values at increased purge flow over the entire channel height.

The blockage and the redistribution of the flow has also been observed by e.g. Schuepbach et al. [100] and Paniagua et al. [69] for configurations where the purge flow is injected upstream of a rotor row. Both effects can lead to additional shear forces since the flow is driven out of its original equilibrium condition. Hence, this is the first possible source of losses identified from the measurements.

In the distribution of the yaw angle α there are regions of under- and overturning visible within the lower 40% channel height. These can be attributed to the development of the secondary flow structures in the upstream rotor row (see e.g. Linker [55]). If the purge is varied, the turning is slightly increased close to the hub and slightly decreased at approximately 40% channel height. However, the general distribution of the yaw angle is almost unchanged at this measurement plane, showing that the purge flow injection has only a minor influence on the general turning in the upstream blade row.

The latter observation of an almost unchanged yaw angle leads to a beneficial side effect. This is the possibility to verify the SPAN model, which is used to assess

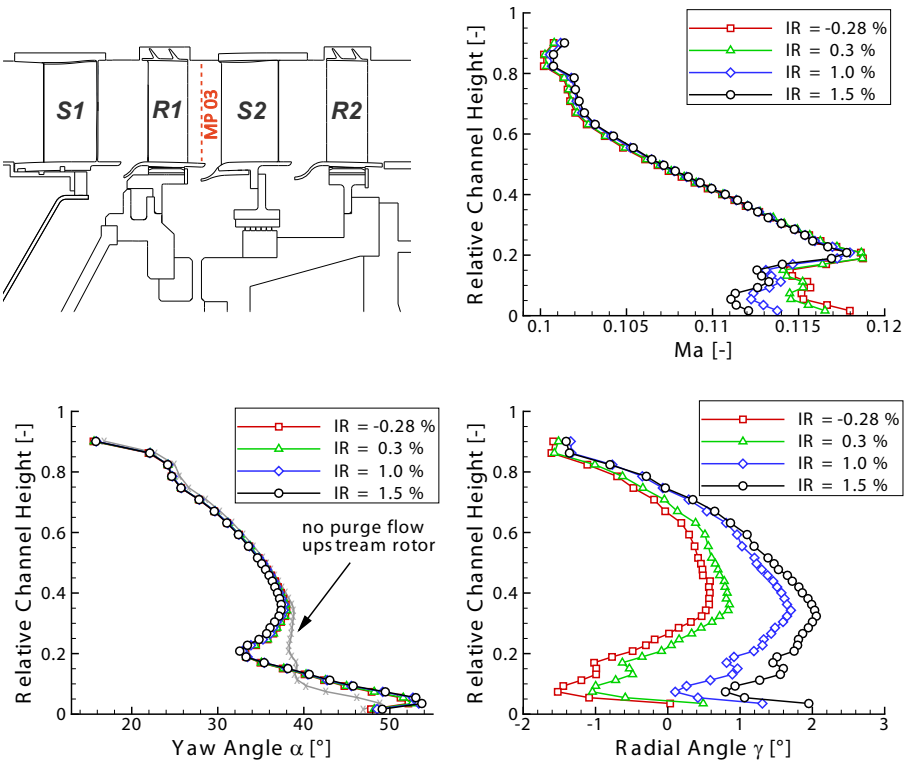

Figure 6.2: *Distribution of Mach number and radial angle at MP03, upstream of rim seal.*

the flow across the labyrinth seals (see Chapter 3.1). As it has been shown by Linker [55], the yaw angle at MP03 is significantly influenced by the purge flow injection upstream of the first rotor row. This is illustrated exemplarily by the grey line in the results of the yaw angle in Fig. 6.2. This case is identical to IR = -0.28%, but represents in contrast to the actual measurements the case of no purge flow injection upstream of the first rotor row. As this S1R1 purge flow has a significant influence, a variation of this purge flow rate would be visible by an altered yaw angle distribution at MP03. Since this is not the case, it can be concluded that the purge flow through this rim seal is constant. This in turn shows that the flow through the first labyrinth seal, which contributes significantly to the S1R1 purge flow, is well estimated by the SPAN model.

Flow Field Downstream of the Second Stator Row

To investigate the influence of purge flow on the main flow in more detail, the flow field downstream of the second stator row at MP04 is examined in the next step (for position of MP04 see Fig. 3.6). The primary interest at this location is on the one hand the influence of purge flow on the development of secondary flow structures and losses across the stator row. On the other hand, the propagation and trajectory of the purge flow within the main annulus shall be examined. Therefore, results from 5-hole-probe and gas-concentration measurements are presented. In order to get familiar with the flow field, a given purge flow rate is examined first. Afterwards the influence of different purge flow rates is elaborated. Since the results from the 5-hole-probe and gas-concentration measurements are time averaged values, no instationary effect of the upstream rotor row or the drive arm hole jets is expected from these measurements.

The general flow field at MP04, measured over two passages, is presented in terms of the total pressure distribution in Fig. 6.3 a, whereas the view is in downstream direction. In addition to the total pressure distribution, the vector field of the secondary flow structures is presented. These vectors show the flow perpendicular to the trailing edge metal angle of the vane, which is constant in span direction. The injection rate of 1.0% is presented since the flow features are well distinguished for this rate. Observing the flow field, the well-known secondary flow features which have been presented in Chapter 2.1 can be examined. Within the upper part of the channel the passage vortex, labelled with **A** and the trailing edge vortex, labelled with **B** are clearly visible by the vector field. The most intense decrease of total pressure is located within the region of the trailing edge vortex, which is associated with increased losses in this area.

Within the lower part of the channel, similarly the hub side passage and trailing edge vortices are visible, whereas the passage vortex is marked with **D** and the trailing edge vortex is marked with **C**. The most intense decrease in total pressure is not located exactly in the centre of the passage vortex, but slightly on the right hand side in an area which possesses high gradients in the secondary velocities [1]. These shear layers make the increased losses in this area reasonable.

In addition to the vortices that are visible by means of secondary flow structures, a region of increased losses is visible close to the hub side endwall. This region,

[1] This has also been assessed by the use of more complex vortex identification criterions, which are independent of a chosen reference system respectively metal angle of the vanes. Exemplarily, also the λ_2 criterion proposed by Jeong and Hussain [39] shows the passage vortex to be left handed of the minimum in total pressure

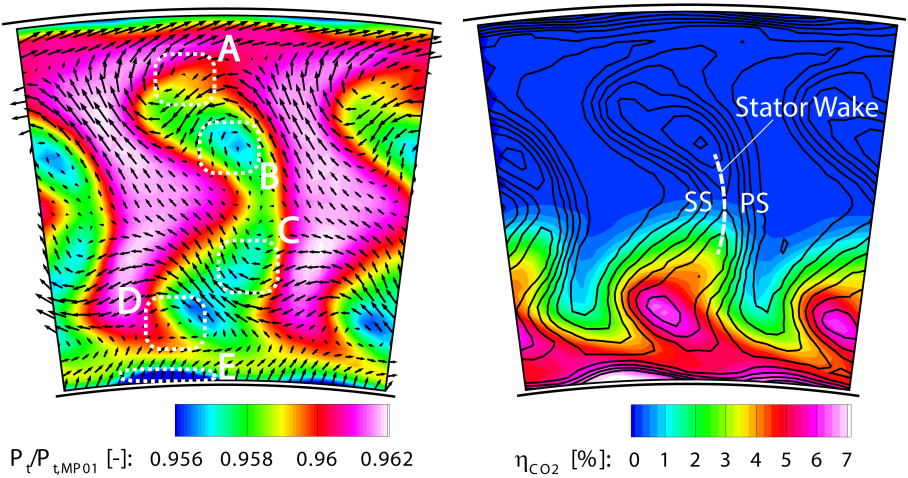

(a) Total pressure distribution and vector field

(b) CO_2 *concentration*

Figure 6.3: *General flow field at MP04, IR = 1.0%*

labelled with **E** in Fig. 6.3 a, might be caused by the suction side corner vortex. However, a discrete vortex structure is not resolved in this area by means of secondary flow structures. For this reason, other effects may be the reason of the decreased pressure. For instance, also flow through the S2R2 rim seal may influence the flow close to the hub and therefore may cause these zones of decreased pressure.

The wake of the stator vane is less pronounced since the hub- and tip-side secondary flow structures have already propagated far away from the end walls, thus reducing the radial extent of the wake. Between the two measured passages slight differences are visible which are probably caused by manufacturing and assembly tolerances. Nevertheless, the general flow features are identical for both passages.

To examine the propagation of the purge flow, the results from the gas concentration measurements are shown in Fig. 6.3 b. The CO_2 concentration is presented as the non-dimensional mixing concentration η_{CO_2} which has been defined in Chapter 3.3.3, but is presented here and in the following as a percentage value. In addition, iso-contours of the total pressure distribution are presented by black lines. Examining the results, it is obvious that the purge flow enters into the lower 50% of the channel. This is concluded from structures of increased CO_2 in this region.

These structures show a vane periodic behaviour and correlate well with the total pressure distribution, whereas the peak concentrations are found in the regions of increased losses and secondary flow structures. All in all it seems that the main part of the purge flow travels along with the secondary flows towards the suction side and finally ends up in the region of the passage vortex, as it has already been observed by Erickson et al. [23], Pau et al. [71] and Paniagua et al. [69]. This assumption is further supported by the fact that the lowest concentration is found at the pressure side of the wakes (right hand side of the wake).
However, it needs to be mentioned that the highest CO_2 concentration is not exactly in the centre of the passage vortex, but rather slightly on the right hand side in the region of increased losses. As it will be shown later in Chapter 6.1.2 with the help of PIV, the velocity within the rim seal is several times smaller than the one of the main fluid (see e.g. Fig. 6.22). Presuming this knowledge, the question arises whether the decreased total pressure is caused by secondary flows, or if just some less energetic fluid from the rim seal penetrates into this region, which is not completely mixed out. This question will be discussed later in this chapter.

After the general flow features and the propagation of the purge flow within the main annulus are known, the influence of different purge flow rates is studied in the next step. Therefore, Fig. 6.4 shows the pressure loss coefficient across the second stator row, which has been defined in Chapter 5.2.2. In the figure four different purge flow rates are shown. For each injection rate a single passage is

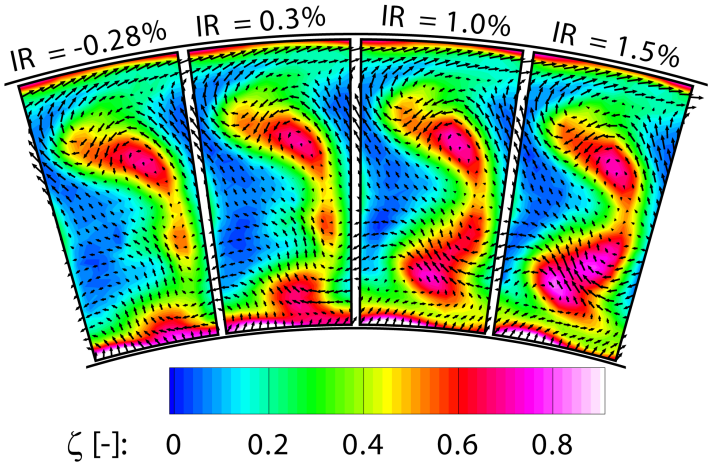

Figure 6.4: *Pressure loss across stator row 2*

presented, whereas the injection rate increases from the left hand side to the right hand side. Pink to white colour indicates the highest losses, whereas blue colour indicates the undisturbed main flow. In general, the influence of the purge flow on the flow structures within the main annulus is limited to the lower 50% channel height. In this region a loss core develops, which increases in size and magnitude if the purge flow is increased. Furthermore, this loss core is shifted radially outwards and completely detaches from the hub side endwall at the highest purge flow rates. Overall the area-averaged pressure loss coefficient increases by 43% if the injection rate is increased from -0.28% to 1.5%. In addition to the increased losses, the secondary flows intensify and move radially outwards, whereas this gets even more clear using circumferentially averaged values, which will be shown later in this section in Fig. 6.7.

The radial migration of the secondary flow structures and losses as well as their intensification has also been observed by many other authors for configurations in which the purge flow is injected upstream of a rotor row, as it has been mentioned in Chapter 2.2.3. However, it looks like as the radial migration of the loss core and secondary flows is more pronounced in the actual configuration. This observation is also made if the results are compared with the ones from Schuler et al. [102], [101], who investigate the influence of the purge flow injection upstream of a stator row with a similar vane profile in a linear cascade. A possible explanation for this will be provided in Chapter 6.2. So far, the amplified secondary flow structures and the related losses are found to be the second source of losses caused by the purge flow injection.

Observing the lowest purge flow rate, it is interesting that the well-known secondary flow structures are hardly visible in terms of the presented vector field. A possible reason for this is a partial removal and thus weakening of the hub side boundary layer downstream of the rim seal, which will be shown later in this chapter by the use of PIV. Furthermore, it will be shown that the purge flow enters with a more favourable direction into the vane passage at the lowest purge flow rate. This influences the crossflow within the passage and may additionally weaken the development of secondary flow structures.

As a next step, the CO_2 concentration is shown for different purge flow rates in Figure 6.5. The concentration is presented again by the colour map, whereas iso-contours of the pressure loss coefficient are presented by black lines. The injection rate of -0.28% which has been shown before can not be measured with the gas concentration system because no external fluid, which could have been seeded, is injected into the wheelspace. Instead, the injection rate of -0.1% is presented. Anyhow, a comparison between the IR of -0.28% and -0.1% has revealed no detectable

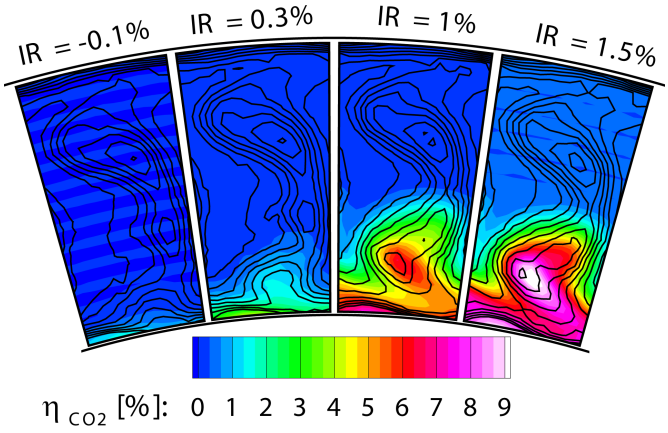

Figure 6.5: *CO_2 concentration at MP04, downstream of the stator row 2*

difference among the flow field at MP04 (see Schrewe et al. [96]). Observing the results an increase of the CO_2 concentration is detected with increasing purge flow. This is expected, since the overall injected mass flow of CO_2 increases. However, in addition to the overall increase of the CO_2 concentration, its distribution changes. Similar to the losses, a definite area of increased concentration develops, which migrates radially outwards. This peak in the CO_2 concentration coincides for all injection rates with the region of increased losses. Furthermore, it is located in the area of increased secondary flows. This strengthens on the one hand the assumption that the purge flow is transported by the secondary flows through the stator passage. However, on the other hand this observation does not help to solve the question whether the decreased total pressure results from the intensified secondary flows or from less energetic fluid leaving the wheelspace. Since the peak in CO_2 coincides at all ingestion ratios with the peak in pressure loss, both alternatives are still possible. To answer this question, a numerical simulation of the geometry has been performed by Schmid et al. [95]. They show in terms of entropy distribution an area of increased losses in the same area of the increased pressure loss coefficient visible in the experiments. This area of increased entropy can be traced back into the rim seal where the entropy is already at an elevated value. This in turn suggests that at least a part of the losses result rather from low pressure or low momentum fluid leaving the rim seal than from the intensified secondary flows. Unfortunately, an experimental validation of this observation is not possible with the current measurement planes.

However, the intensified secondary flow structures are still of relevance since they determine the inflow conditions of the subsequent rotor row in terms of Mach number, yaw- and radial angle. To examine the influence of the purge flow on these inflow conditions of the second rotor row, contour plots and circumferentially averaged values of Mach number and yaw angle will be provided next.

Figure 6.6 shows the Mach number distribution at MP04 for the four different purge flow rates. On the left hand side contour plots are shown, whereas the right hand side shows circumferentially averaged data. Examining the results, a uniform increase of the Mach number is observed in the upper 50% channel height. This is caused by the overall increase of massflow within the main annulus. In the lower 50% there are distinct zones of decreased velocity visible, which coincide in their position with the regions of increased losses and CO_2 concentration. Close to the hub the velocity is increased more than average. This is probably caused by an increased overturning in this area which will be shown below.

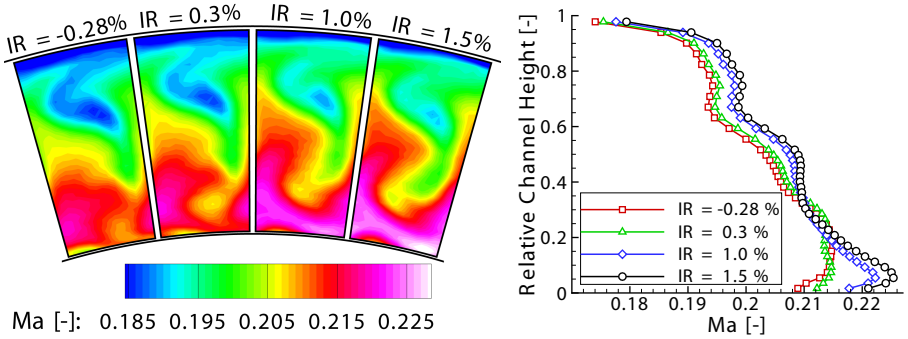

(a) Mach number distribution at MP04 *(b) Circumferentially averaged values*

Figure 6.6: *Mach number distribution at MP04 for different purge flow rates*

Figure 6.7 a shows the yaw angle distribution at the four different purge flow rates. There are distinct regions of under- and overturning visible at the hub and the tip, which are representative of the secondary flow structures examined before. For the lowest purge flow rate no over-turning (indicated by green to blue colour) is visible within the lower 50% channel height. However, if the purge flow is increased to IR = 1.5% the magnitude of the over- and under turning increases by 4° respectively 2.5°. In addition, the region of peak underturning is shifted radially outwards from 6% channel height for IR = -0.28% to 25% channel height for IR = 1.5%. This is

even better visible in circumferentially averaged values presented in Fig. 6.7 b. In addition to the radial movement, this figure clearly shows the growth of under- and over-turning regions and hence the intensification of the secondary flow structures. Comparing the variation of over- and underturning with the values observed by other authors for configurations where the purge flow is injected upstream of a rotor row, similar values are assessed. However, the radial movement of the secondary flow structures seems to be larger in the present configuration as is has already been stated before.

Overall, the changed Mach number and yaw angle at MP04 influence the inflow conditions for the second rotor row. With increasing purge flow the rotor row experiences a positive incidence at the hub and a negative incidence at 25% channel height. In addition, the velocity distribution is altered. Even though the influence of the changed inflow conditions on losses is not known, in general detrimental effects are expected if the blades run out of their design point. Especially in low pressure turbines, the leading edges have a smaller radius and are therefore more sensitive to a changed incidence situation. Thus, the changed inflow condition for the subsequent rotor row is the third possible reason of losses identified from the measurements.

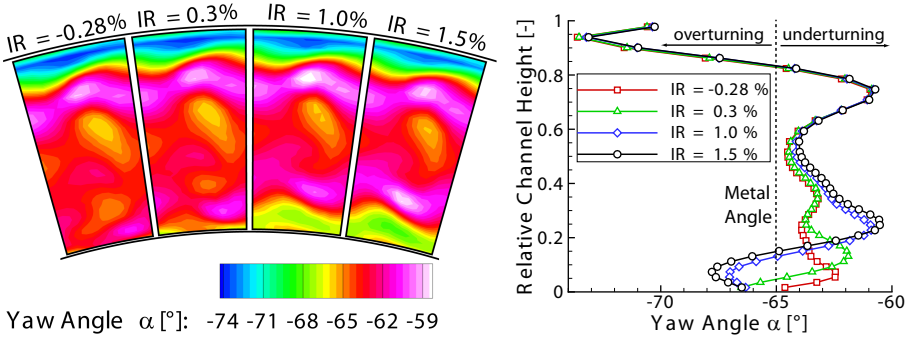

(a) Yaw distribution at MP04 *(b) Circumferentially averaged values*

Figure 6.7: *Yaw angle distribution at MP04 for different purge flow rates*

Summarising the results obtained at MP04, a strong influence of purge flow on secondary flow structures downstream of the stator row is determined. This leads to increased losses and spoils the inflow conditions of the subsequent rotor row.

Furthermore the propagation of the purge flow trough the stator passage is related to the secondary flows in the vane.

Flow Field at and within the Rim Seal

In this section, the flow field at and within the rim seal is analysed. A detailed understanding of the flow phenomena in this region is of great interest, since it provides new insights into the interaction between purge and main annulus flow, which in turn may help to understand the previous results. For this purpose the results from PIV measurements are presented. In addition, the pressure distribution and adiabatic cooling effectiveness on the stator platform is examined.

First, the stator 2 platform pressure distribution is investigated. For this purpose Fig. 6.8 shows the measured static pressure 4% C_x upstream of the stator 2 leading edge, where 8 taps are located in circumferential direction (see Fig. 3.6). The pressure distribution is plotted in terms of k_p, which is defined by Equation 5.9 and allows to assess the amplitude as well as the phase angle of the pressure variation.

At 4% C_x upstream of the leading edge a periodic pressure variation is visible which corresponds to the stator pitch. The pressure peak is located at the leading edge of the vane and is probably caused by its potential field. According to the model presented by Johnson et al. [41], this increased pressure may lead to a reduced outflow of purge flow or even ingestion of main flow at this position. In the centre of the passage the pressure is in contrast decreased below its average value. This leads, compared to the location at the leading edge, to a weaker ingestion or a more intense outflow of fluid. If the purge flow is increased, a slight variation of the amplitude can be observed. But the more interesting observation is that the curves tend to move a bit towards the suction side of the stator with exception of the highest purge flow rate. This suggests that the stagnation point is shifted towards the suction side of the vane, which is probably caused by a negative incidence at the stator as it will be shown later by the help of PIV.

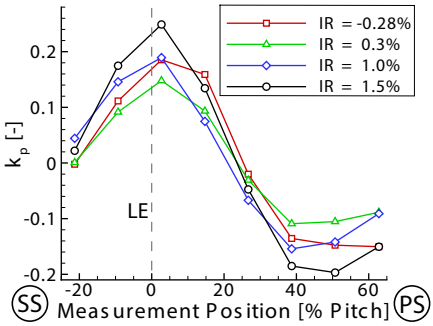

***Figure 6.8:** Stator 2 platform pressure distribution; 4% C_x*

To correlate the pressure distribution with regions of ingress and egress and hence to validate the assumptions given above, gas concentration measurements have been conducted. This allows on the one hand to assess the adiabatic cooling effectiveness and hence the propagation of the purge flow at the stator platform. On the other hand, a comparison of the pressure distribution and the cooling effectiveness is feasible. Figure 6.9 shows the adiabatic cooling effectiveness at 4% C_x and at 10% C_x upstream of the stator 2 leading edge. For both situations the additional injection rates of 0.5% and 0.75% are included to assess the distribution of the cooling effectiveness in more detail.

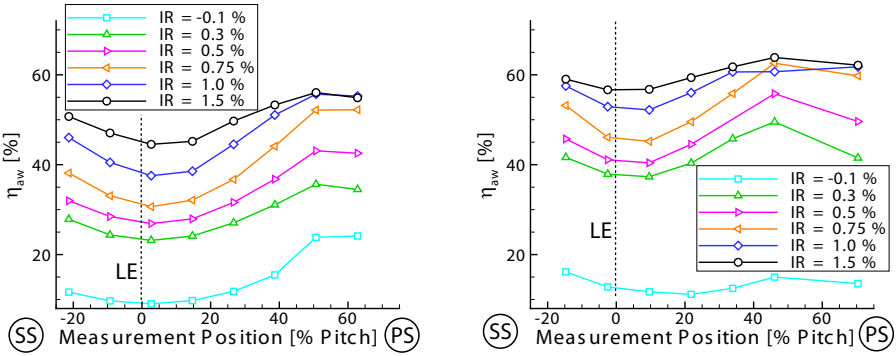

(a) 4 % axial chord upstream stator 2. *(b) 10 % axial chord upstream stator 2.*

Figure 6.9: *Distribution of adiabatic cooling effectiveness at the hub of stator 2*

Observing the distribution of the cooling effectiveness at 4% C_x upstream of the leading edge, a good correlation with the pressure measurements is determined. The lowest cooling effectiveness is examined at the position of the leading edge, where the highest static pressure is examined. Within the passage, an increased cooling effectiveness corresponds to the reduced static pressure in this area. This observation is valid for all injection rates.

Examining the different purge flow rates, a rise in cooling effectiveness is observed in general. This rise in cooling effectiveness is first very sharp, but reduces for high purge flow rates. This yields for the engine representative purge flow rate of IR = 0.3% a cooling effectiveness of 23% to 35%, which is already half the cooling effectiveness gained at the much higher purge flow rate of 1.5%. In addition to the rise, a flattening of the cooling effectiveness distribution is observed at the highest

purge flow rates. This leads to a more uniform distribution of the coolant flow at the endwall.

Another interesting observation is that even for the lowest of the studied purge flow rates a remarkable CO_2 concentration is detected at the stator lip, even though the integral mass flow through the rim seal is assessed to be negative by the SPAN model. This shows that a part of purge flow which is delivered through the drive arm holes into the wheelspace propagates up to the rim seal region and does not directly flow through the stator 2 labyrinth seal. The latter case is assumed to be possible since the mass flow through the rim seal is larger than the one delivered through the drive arm holes.

At 10% C_x upstream of the leading edge, the general effects are similar to the ones at 4% C_x, showing a lower cooling effectiveness at the vanes leading edge and a higher one in the passage. However, except for the lowest injection rate, the cooling effectiveness is elevated at this position, leading to values of 37%-50% for the engine representative IR and 57%-64% for IR = 1.5%. A possible reason for this increase is the ingestion of less main annulus fluid into this region of the rim seal, as it will be shown later by the use of PIV. Comparing the adiabatic cooling effectiveness with the one measured by Feiereisen et al. [25] at the hub of a rotor blade, lower values are determined. For instance, Feiereisen et al. measured cooling effectiveness values of 75%-96% at the hubside endwall at 20% C_x upstream of the leading edge for an IR of 1.5%.

To gather a more detailed picture of the flow field in the area of the rim seal, results from PIV are presented on the following pages. In addition to a detailed measurement of the flow field at and within the rim seal, this measurement technique allows to present phase-locked results. This allows in contrast to the previously shown results from time averaged measurement techniques to assess the effects of the rotor wakes or the influence of the drive arm hole jets.

To get familiar with the presentation of the results and the basic flow features, first the flow field within the main annulus, measured at 13% relative channel height with a light sheet in circumferential direction (setup C) is presented in Fig. 6.10. In this figure the in-plane velocity $V_{x\theta}$ is shown at the engine representative purge flow rate of IR = 0.3%, which will be called the reference case in this section. The measured area covers two stator pitches, three rotor pitches, one drive arm hole and is assembled from 6 single pictures. The rotor-stator relative position was chosen to be the one where the velocity deficit at the leading edge of the middle stator vane is highest, assuming that this is the position where the wake of the rotor hits the leading edge of the stator. If not stated otherwise, this rotor-stator relative position is used in all subsequent figures to discuss the examined flow features.

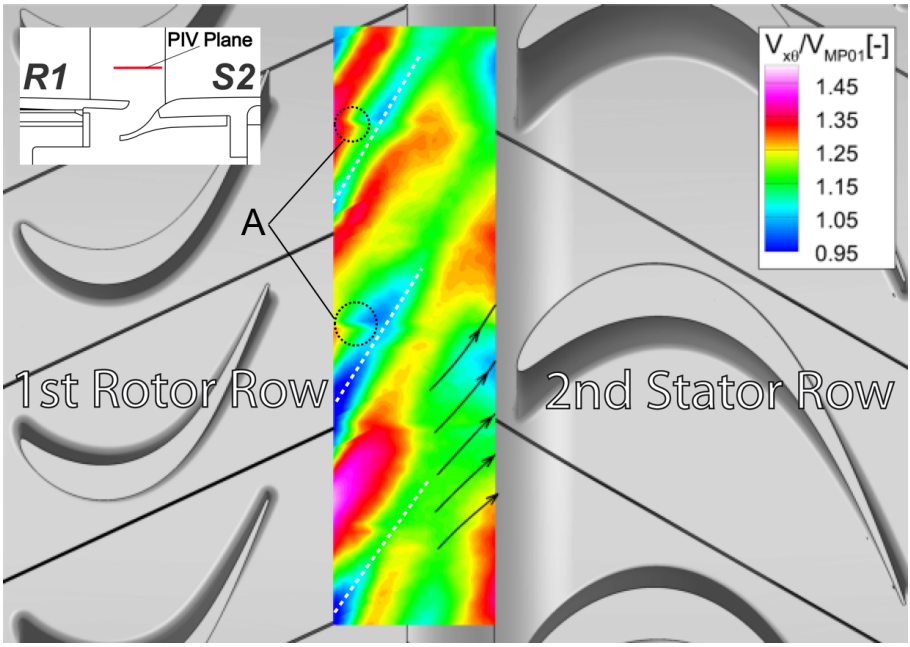

Figure 6.10: *In plane velocity $V_{x\theta}$ at 13% channel heigt; IR = 0.3%*

Examining the distribution of the in-plane velocity, the wakes of the rotor are clearly visible by means of a lower velocity magnitude. For a better visualisation the wakes are marked with dashed lines of white colour representing their qualitative location and trajectory. Close to the leading edges of the vanes the flow gets decelerated due to the presence of the vane. Furthermore, the flow is divided at the leading edge into a stream along the suction side and one along the pressure side. This leads to an increased turning at the suction side and a decreased turning at the pressure side, which can be seen by the in-plane streamlines, indicated in black colour. The decrease in velocity close to the leading edge is more pronounced at the middle vane as this one is aligned with the rotor wake which features an already reduced velocity. The upper vane is in contrast aligned to the passage flow of the rotor, since three rotor blades and two stator vanes form one periodic sector. Thus, the velocity deficit there is less pronounced.

In some areas there are abrupt changes in the velocity visible. These discontinuities, exemplarily labelled with **A** in Fig. 6.10, are particularly present in the regions of

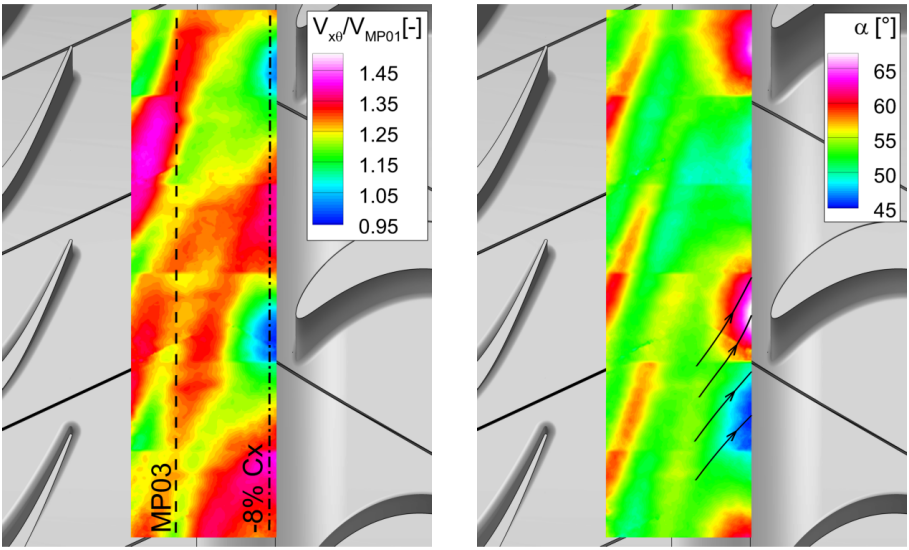

(a) In plane velocity at 3.3% channel height *(b) Yaw angle at 3.3% channel height*

Figure 6.11: *In plane velocity and yaw angle at 3.3% channel height; IR = 0.3%*

the rotor wakes and arise from the assembly of different pictures to present the whole periodic sector. Towards the edges of the single pictures the perspective error described in Chapter 3.3.2 increases and thus leads to the observed discontinuities. Nevertheless the general flow field is well presented and not changed significantly by these discontinuities.

In the next step, the flow field close to the hubside endwall is examined. Therefore, Fig. 6.11 shows on the left hand side the in-plane velocity $V_{x\theta}$ and on the right hand side the yaw angle at 3.3% channel height. Again the injection rate of 0.3% is shown.

In general, the flow field is similar to the one obtained at 13% channel height, showing the decreased velocity at the leading edges of the stator vanes as well as the wakes of the rotor. Again the velocity deficit is more pronounced at the middle stator vane, even though the position of the wake structure is shifted for some reason by approximately half of the rotor pitch in circumferential position. However, in addition to the relocation of the wake structure there are further differences distinguishable. Overall, the velocity magnitude is increased at 3.3% channel height.

Furthermore, the rotor wakes are less pronounced in terms of the pitch-wise velocity variation. For a better visualisation of the latter fact, the velocity variation at the axial position of MP03, illustrated by the dashed line in Fig. 6.11 a, is extracted and shown in Figure 6.12 a. To allow for a comparison, the values are plotted together with the corresponding values at 13% channel height. It is observed that the variation of the in-plane velocity is less intense at 3.3% channel height. The three wakes of the rotor that are present in the velocity distribution at 13% channel height are hardly visible at 3.3% channel height.

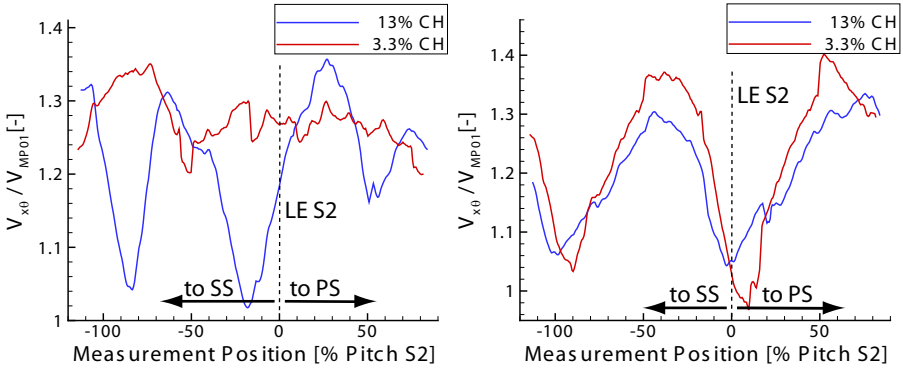

(a) In plane velocity at MP03 *(b) In plane velocity close to the LE*

Figure 6.12: *Comparison of depicted data at 3.3% and 13% channel height; IR = 0.3%.*

The pitch-wise velocity variation close to the leading edge of the stator is shown in Fig. 6.12 b again for both channel heights. It is taken at 8% C_x upstream of the stator 2 leading edge, which is illustrated by the dash-dotted line in Figure 6.11 a. In contrast to the previous results, an increase of the velocity fluctuation is observed close to the hubside endwall at this position. A comparison of the different positions shows that the velocity fluctuations at 3.3% channel height are almost 3 times higher upstream of the vanes leading edge compared to the ones caused by the rotor wakes slightly upstream of the rim seal. From this it is assumed that the flow field in the rim seal is rather influenced by the potential field of the stator than by the wake of the rotor. In addition to the dominant effect of the stator, it is observed from Fig. 6.12 b, that the point of the lowest velocity is shifted towards the pressure side at 3.3% channel height. This is presumably caused by the geometry of the vane which is bended towards the pressure side at the hub (as described in Chapter 3.2).

If in addition to the in-plane velocity, the yaw angle in Figure 6.11 b is examined, the split of the flow around the vanes leading edge gets clearly visible by means of diverse flow directions. This leads to a strong increase of the yaw angle at the suction side area of the leading edge. Similarly the yaw angle decreases at the pressure side area of the vane.

After the basic flow field in the main annulus is examined, the flow field within the rim seal is analysed in the next step. Therefore, Figure 6.13 shows the measured in-plane velocity $V_{x\theta}$ and yaw angle α at -2% channel height. This time also the decomposition of the velocity into the axial velocity V_x and the tangential velocity V_θ is shown to explain the flow features in more detail.

First of all it is visible that the flow field at this channel height shows a vane periodic behaviour even though a fixed rotor-stator relative position is shown. This shows that the flow within the rim seal is rather affected by the potential field of the stator vanes than by the wakes of the rotor. This can most probably be related to the effects described above, which have shown a less pronounced effect of the rotor wake close to the hub side endwall. Furthermore, the vane periodic behaviour indicates that there is no influence of the drive arm hole jets existing within the rim seal at this purge flow rate. Since these holes are present only once in the presented sector, neither a rotor nor a stator periodic structure would be expected if these jets have a significant influence.

Another important finding is that the in-plane velocity $V_{x\theta}$ is several times smaller than the one in the main flow, especially downstream of the rotor platform. This shows that the purge flow features a significantly reduced velocity in comparison to the main annulus flow. Furthermore, it is examined that $V_{x\theta}$ is not reduced anymore upstream of the vane's leading edge, as it has been the case in the main flow. Instead it is increased at this position and in the region towards the suction side, which is marked by **A** in Fig. 6.13 a. A first hint for the origin of this initially confusing result can be found in the distribution of the tangential velocity component V_θ, presented in Fig. 6.13 c, which shows significantly increased values in the same region. This increase in tangential velocity results probably from ingested main fluid in this area, which owns a higher velocity magnitude. This assumption will be fortified below in this section by results from PIV with a radial light sheet which shows the ingestion of main fluid to be most severe in this region (see Fig. 6.14).

Analysing the yaw angle distribution in Fig. 6.13 d, an increase of about 15° compared to the value at 3% channel height is observed upstream of the vanes leading edge. A possible reason for this is that the ingested main fluid is decelerated in axial direction if it approaches the platform but keeps its tangential velocity component. This in turn increases the yaw angle.

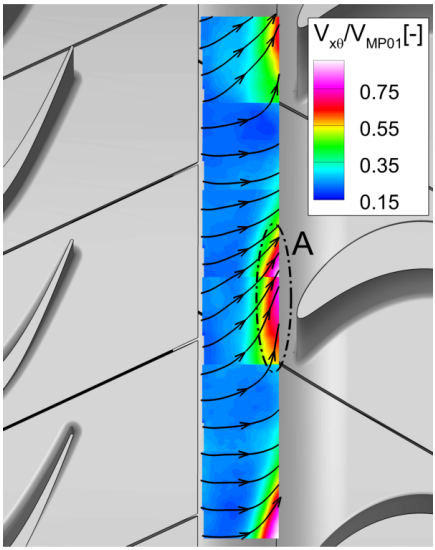

(a) In plane velocity $V_{x\theta}$

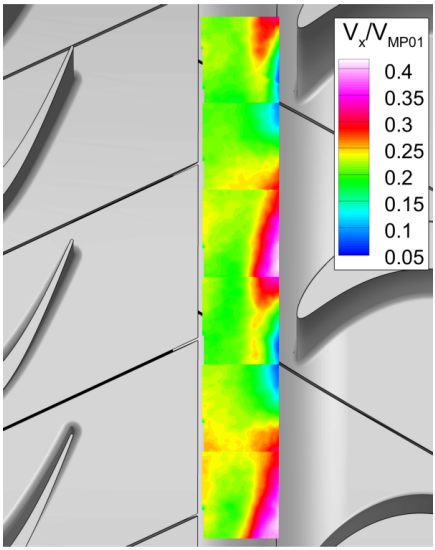

(b) Axial velocity V_x

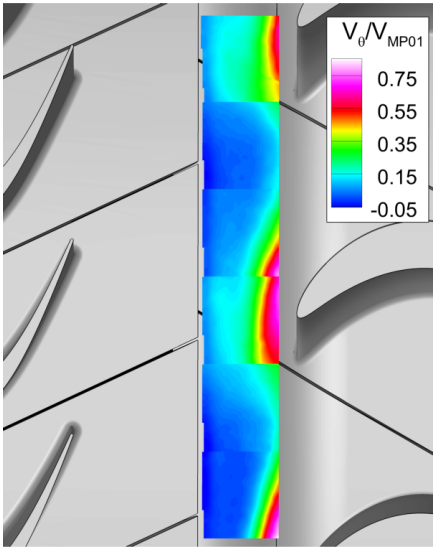

(c) Tangential velocity V_θ

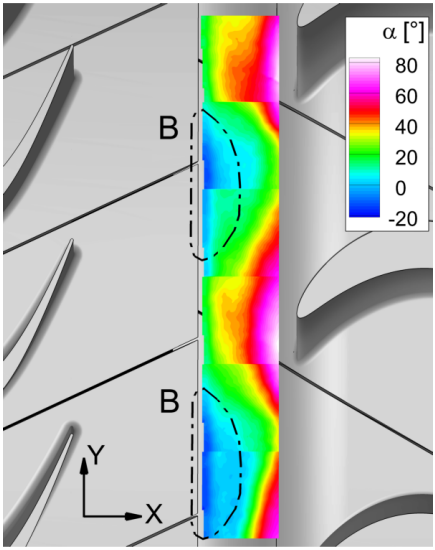

(d) Yaw angle α

Figure 6.13: *Flow field at -2% channel height; IR = 0.3%*

In contrast to the region upstream of the leading edge, the flow is turned in negative Y direction just downstream of the rotor platform in the region labelled with **B** in Fig. 6.13 d. This turning in negative Y and thus rotor rotational direction is caused by fluid that leaves the rotor-stator wheelspace underneath the rotor platform. This fluid carries a tangential velocity component in rotor rotational direction, which is applied by friction at the rotating walls and the delivery of the purge flow through rotating drive arm holes into the wheelspace. Thus, a negative yaw angle is supposed to be an indicator for egress of purge flow. Using this indicator it is examined that the purge flow leaves the rim seal in the area labelled with **B**, which is located between the leading edges of the stator vanes. This is in agreement with the results obtained from the CO_2 measurement shown previously in this section and results obtained from radial light sheets, which will be presented below. Moving downstream, the expelled purge flow mixes with main annulus flow which carries a tangential velocity in opposite direction. This continuously changes the flow direction within the rim seal.

To get additional information of the flow field within the rim seal, PIV measurements with a light sheet in radial-axial direction (setup R) have been carried out. In total, 12 pitch-wise locations have been measured as indicated by the dashed grey and solid black lines in Fig. 6.14 a. Four of them will be investigated in more detail in this section and are marked by the black lines. Figure 6.14 b - e shows the radial velocity component and the in-plane streamlines at these positions. For orientation the rotor platform, the stator platform as well as the stator vane's leading edge is illustrated in the figures. Investigating the distribution of the radial velocity at the depicted planes it gets obvious that fluid is discharged out of the rim seal underneath the rotor platform, whereas at the stator platform fluid enters into the rim seal. This leads to a recirculation zone within the rim seal which is clearly visible by the in-plane streamlines. Due to this recirculation zone the major part of fluid which is expelled at the trailing edge of the rotor platform is driven back into the rim seal shortly downstream. In addition, it appears that a part of the main fluid is ingested into the rim seal, even though the in-plane streamlines do not physically show the movement of a fluid particle.

Analysing the different pitch-wise planes one after another, it gets visible that the ingestion of fluid into the rim seal is most pronounced upstream of the vane's leading edge (position **I** in Fig. 6.14 a). This becomes apparent by the highest negative radial velocities in this area, which are indicated by blue colour and are most probably caused by the increased pressure upstream of the vanes leading edge. The increased ingestion upstream of the leading edge displaces main flow, which has a higher velocity magnitude than the purge flow, into the rim seal. As previously

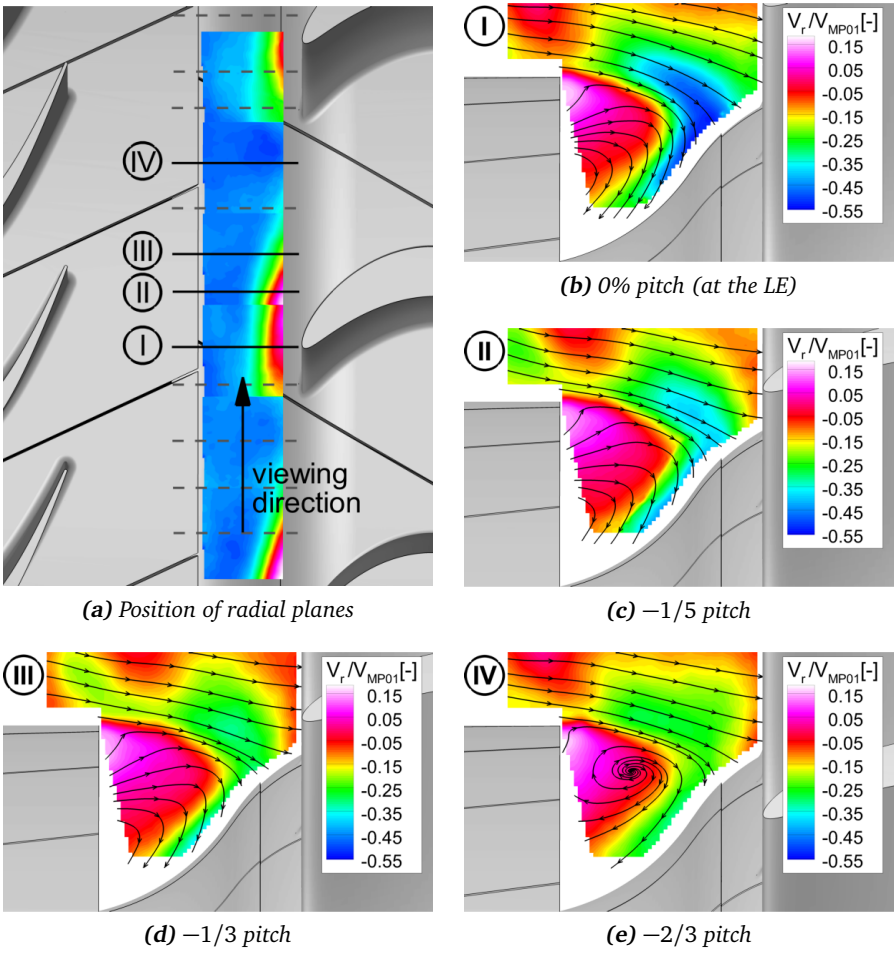

(a) *Position of radial planes*

(b) *0% pitch (at the LE)*

(c) $-1/5$ *pitch*

(d) $-1/3$ *pitch*

(e) $-2/3$ *pitch*

Figure 6.14: *Radial velocity component within the rim seal at different pitch-wise locations; IR = 0.3%.*

mentioned this explains the regions of increased in-plane velocity $V_{X\theta}$ upstream of the stator 2 leading edge, which has been observed at -2% channel height.

Examining the flow field at planes which are located towards the suction side at -1/5 and -1/3 pitch (position **II** and **III** in Fig.6.14 a), the ingestion of fluid

decreases continuously, whereas some ingestion still occurs. Simultaneously the area of positive radial velocity increases in size, leading to an increased egress of purge flow in this area. However, in general the structure of the flow field remains unchanged and forms the already mentioned recirculation zone, whose centre is not located in the area accessible by the PIV system. This changes if the plane located at -2/3 pitch is investigated. At this plane, labelled with **IV** in Fig. 6.14, the centre of the recirculation zone is visible within the accessible area of the rim seal.

To examine the recirculation zone within the rim seal in more detail, Fig. 6.15 presents the in-plane streamlines at all radial measurement planes. To improve the clarity of the figure only the streamlines that belong to the recirculation zone are shown. Examining the qualitative formation of the recirculation zones at the different planes, it looks like as they form a continuous vortex. This vortex is located within the rim seal and propagates in circumferential direction. A deflection of this vortex into the passage, as observed by Popovic and Hodson [78], is not observed from the measurements at this purge flow rate. Instead, the vortex features a vane periodic structure with a visible vortex centre located at the pressure side of the vanes. However, towards the suction side of the vanes the centre of the vortex is not detectable in the area accessible with the PIV system. Since both vanes experience a different rotor-stator relative position but feature a similar flow structure, it can be concluded that in addition to the flow field, also the recirculation zone is mainly driven by the existence of the stator vanes. The rotor wakes, however, seem to have less influence on the formation of this vortex.

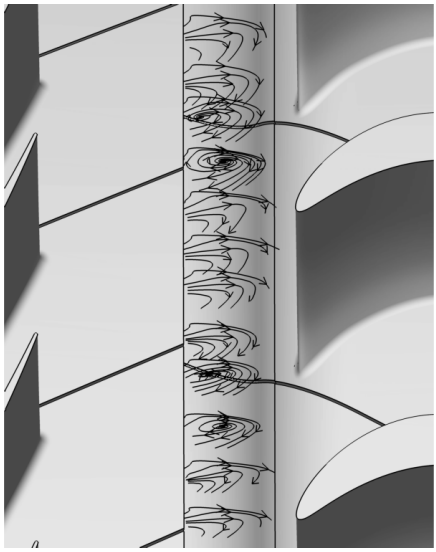

Figure 6.15: *In-plane streamlines within the rim seal, IR = 0.3%*

If the values at a constant channel height are extracted from each radial measurement plane, the resulting slices can be used to generate a circumferential plane, showing the radial velocities V_r at the selected channel height. For this an interpolation is used between the discrete slices. The advantage of this interpolation is that the regions of ingress and egress can be visualized for the whole periodic

sector in a single figure. This omits the necessity to analyse all radial planes step by step. In addition, a comparison with the measurements at a constant channel height shown before is simplified. However, it should be kept in mind that effects which may occur between single measurement planes are not detected. Figure 6.16 shows the radial velocity at -2% channel height generated this way, using all of the 12 radial planes. To highlight the border between in and outflow the dashed line represents $V_r = 0$.

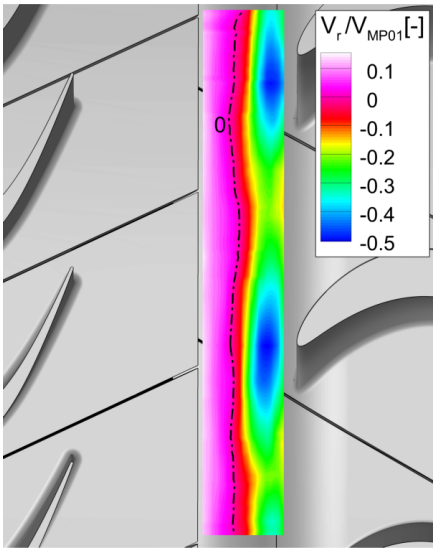

Figure 6.16: *Radial velocity at -2% channel height, IR = 0.3%*

Observing Fig. 6.16 the already described effects are apparent. The strongest ingress is located upstream of the leading edge of the vanes and the outflow of fluid is increased within the passage. In addition to these results it becomes clear that the ingress at both vanes is almost equal and that the whole flow structure is vane periodic for IR = 0.3%. This finally shows that in addition to the flow field within the rim seal also the ingestion of main flow is primarily driven by the vanes and not by the rotor wakes.

Results from PIV for Different Purge Flow Rates

On the previous pages, the general flow field in the rim seal has been investigated in detail with the help of PIV for the engine representative purge flow rate. These results have shown that the flow field and ingestion mechanisms are dominated by the influence of the stator vane at this purge flow rate. An influence of the drive arm hole jets is however not determined. Furthermore a negative yaw angle has been identified to be an indicator for the egress of purge flow.

In the next step, the influence of different purge flow rates on the flow field within the rim seal is assessed. For this purpose, the flow field at -2% and 3.3% channel height is investigated. In addition, results obtained from the radial planes are examined. First, Fig. 6.17 shows the distribution of the yaw angle measured at -2%

channel height. In total four different purge flow rates are shown in this figure, whereas the same scale of the colourbar is used for each purge flow rate. As it has been mentioned in Chapter 4.2, a full periodic sector is measured only for IR = 0.3% and IR = 1.5% with the PIV system. For the other IRs only one passage is measured. This explains why the results are presented for one stator passage only in Fig. 6.17 a and c.

Analysing the results, a tremendous change in the yaw angle is observed due to the different purge flow rates. For the maximum ingestion case with IR = -0.28% (Fig. 6.17 a), the distribution of the yaw angle is in general similar to the previously discussed case of IR = 0.3%, but showing a significantly increased yaw angle downstream of the rotor platform. This can be explained by the higher amount of main annulus flow which is ingested at this purge flow rate. As already mentioned the ingested fluid carries a high tangential velocity opposite to the rotor rotational direction. If the amount of ingested fluid increases, more fluid of high tangential velocity is transferred into the rim seal. This fluid mixes with the one in the rim seal and thus increases the swirl.

If the seal air mass flow is increased to IR = 1% or 1.5%, the yaw angle decreases and reveals in large areas negative values, facing almost in opposite direction compared to the case of the lowest purge flow rate. The reason for this is on the one hand that less fluid which owns the high tangential velocity of the main flow is drawn into the rim seal. On the other hand, the purge flow delivered into the rim seal is increased. This fluid possessed a tangential component in rotor rotational direction which is applied by friction at the rotating walls and by the delivery of the purge flow through the rotating drive arm holes. Since these holes rotate at the speed of the rotor, also the fluid which is delivered through these holes enters into the wheelspace with approximately the rotor rotational speed at the same radial height. If the fraction of the delivered to the ingested fluid increases, also the swirl of the purge flow in rotor rotational direction increases, as it is observed in the measurements. Overall, the measured variation of the yaw angle at -2% channel height is approximately 130° if the injection rate is increased from -0.28% to 1.5%.

In addition to this tremendous change in yaw angle, a structure that is neither rotor nor stator periodic is observed for the highest purge flow rate. Particularly in the upper region of Fig. 6.17 d, a distinct region of increased negative yaw angle is visible, which is not in such a pronounced manner visible in the lower part of the periodic sector. If the negative yaw angle is used as an indicator for egress, it can be concluded that in this area increased egress of purge flow occurs. Since there is only one drive arm hole present within the shown periodic sector, it seems reasonable that the unperiodic structure is caused by the drive arm hole jets. To examine this in

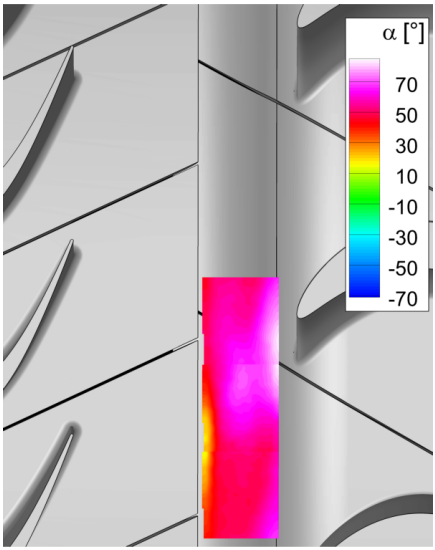

(a) IR = -0.28%

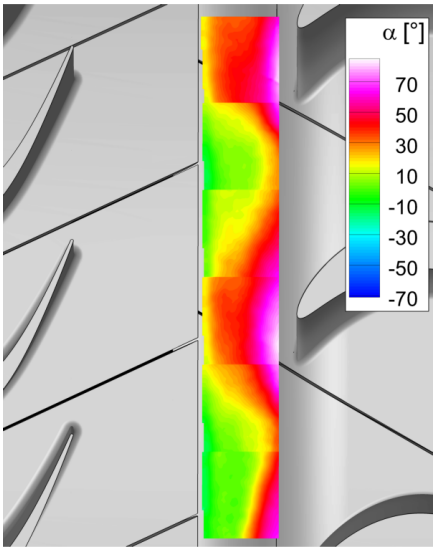

(b) IR = 0.3%

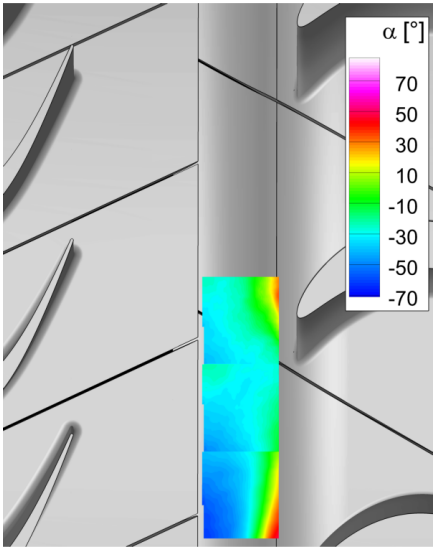

(c) IR = 1.0%

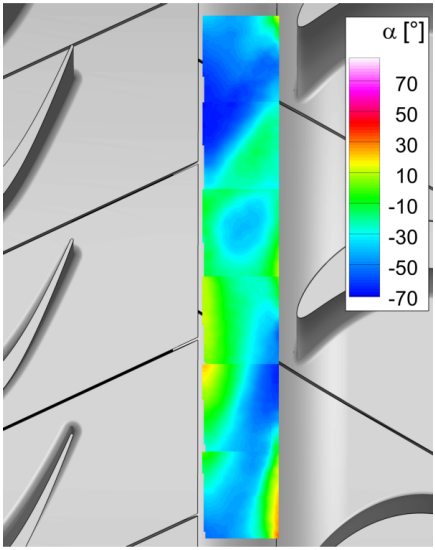

(d) IR = 1.5%

Figure 6.17: *Distribution of yaw angle upstream S2 at -2% channel height*

more detail, the velocity distribution at the same channel height is presented in the next step in Fig. 6.18 for the different purge flow rates. In this figure the unperiodic structure is even better visible at IR = 1.5%. In the upper region of Fig. 6.18 d there is a distinct region of increased in-plane velocity visible. This region coincides with the position of the increased yaw angle shown in Fig. 6.17 and is followed by a wake-like structure which disappears continuously. This wake-like structure leaves the figure at the upper edge but is continued in the lower part of the figure. Thus it is existent once in a periodic sector made up of two vanes, three blades and one drive arm hole. All this supports the assumption that the structure is indeed caused by the drive am hole jets, whereas the region of increased velocity is most probably caused by the fact that the jet impinges on the rotor platform in this area. Since this jet leaves the drive arm hole with a tangential velocity in rotor rotational direction, this also explains the distinct zone of negative yaw angle.

Nevertheless, before the unperiodic structure and thus the effect of the drive arm hole jets is investigated in more detail, further results from the in-plane velocity shown in Fig. 6.18 shall be examined first. This velocity increases if the purge flow rate is reduced from the reference case of IR = 0.3% to the case of IR = -0.28%. The reason for this is again supposed to be the increased ingestion of main fluid, which features a higher velocity than the one expelled underneath the rotor platform. The ingested fluid mixes with the fluid in the rim seal and thus increases the velocity within the rim seal, whereas the tangential component is the major contributor to this effect. If the injection rate is increased from 0.3% to values of 1% or even 1.5%, the in-plane velocity increases again, whereas it is still below the main annulus velocity for the most part of the shown rim seal sector . This increase of the in-plane velocity can most probably be explained by the increased amount of purge flow which is expelled underneath the rotor platform. In addition to the in average elevated in-plane velocities, the increased velocity upstream of the vanes' leading edges, which has been observed for the low purge flow rates, is not visible anymore for the high purge flow rates. A reason for this could be that less or almost no fluid is displaced towards the hub which had previously increased the velocity in this area.

After the general influence of the injection rate on the flow field has been studied at -2% channel height, in the next step the flow field is investigated at 3.3% channel height for the different purge flow rates. The main purpose of this is to figure out whether the tremendous change of the flow field within the rim seal is also present within the main flow.

First, the distribution of the yaw angle is presented in Fig. 6.19. Still a significant variation of the yaw angle can be observed between the different purge flow rates,

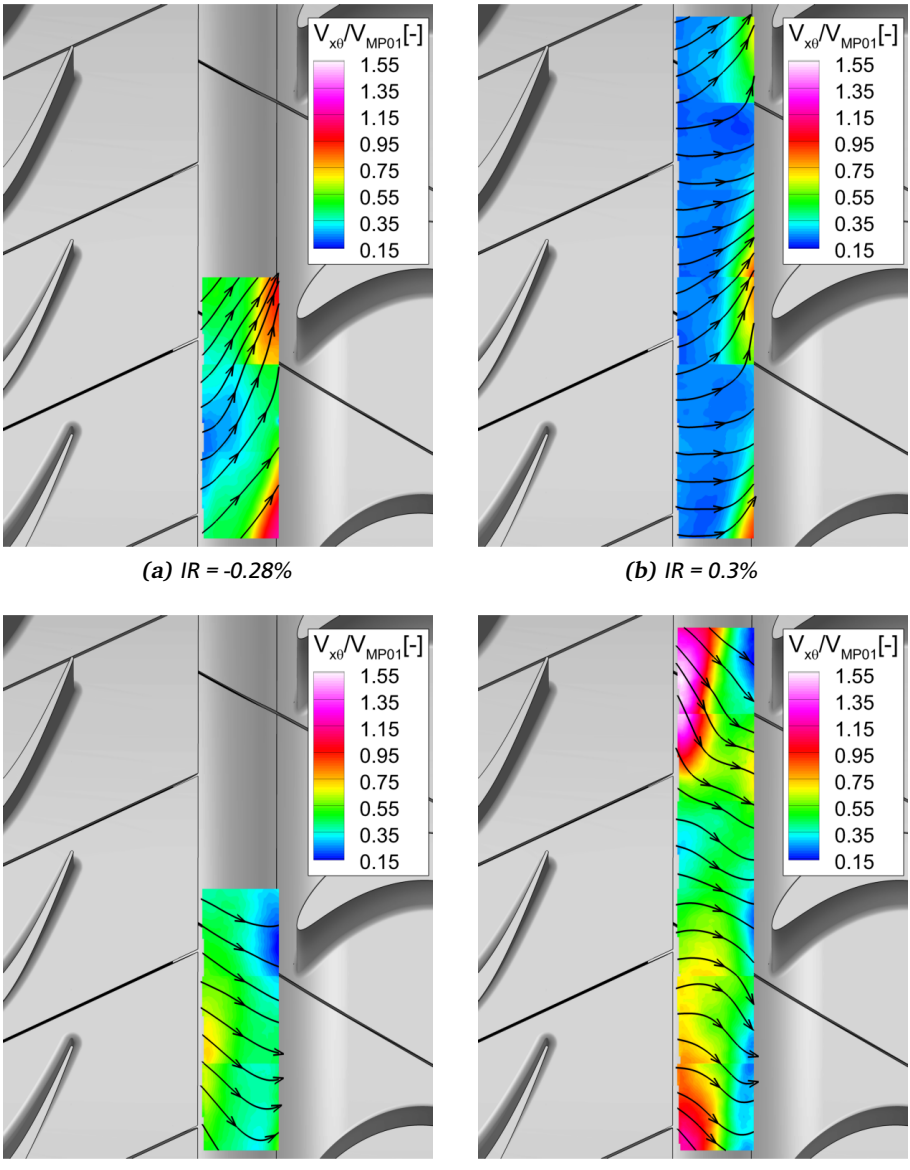

(a) IR = -0.28%

(b) IR = 0.3%

(c) IR = 1.0%

(d) IR = 1.5%

Figure 6.18: *In plane velocity distribution upstream S2 at -2% channel height*

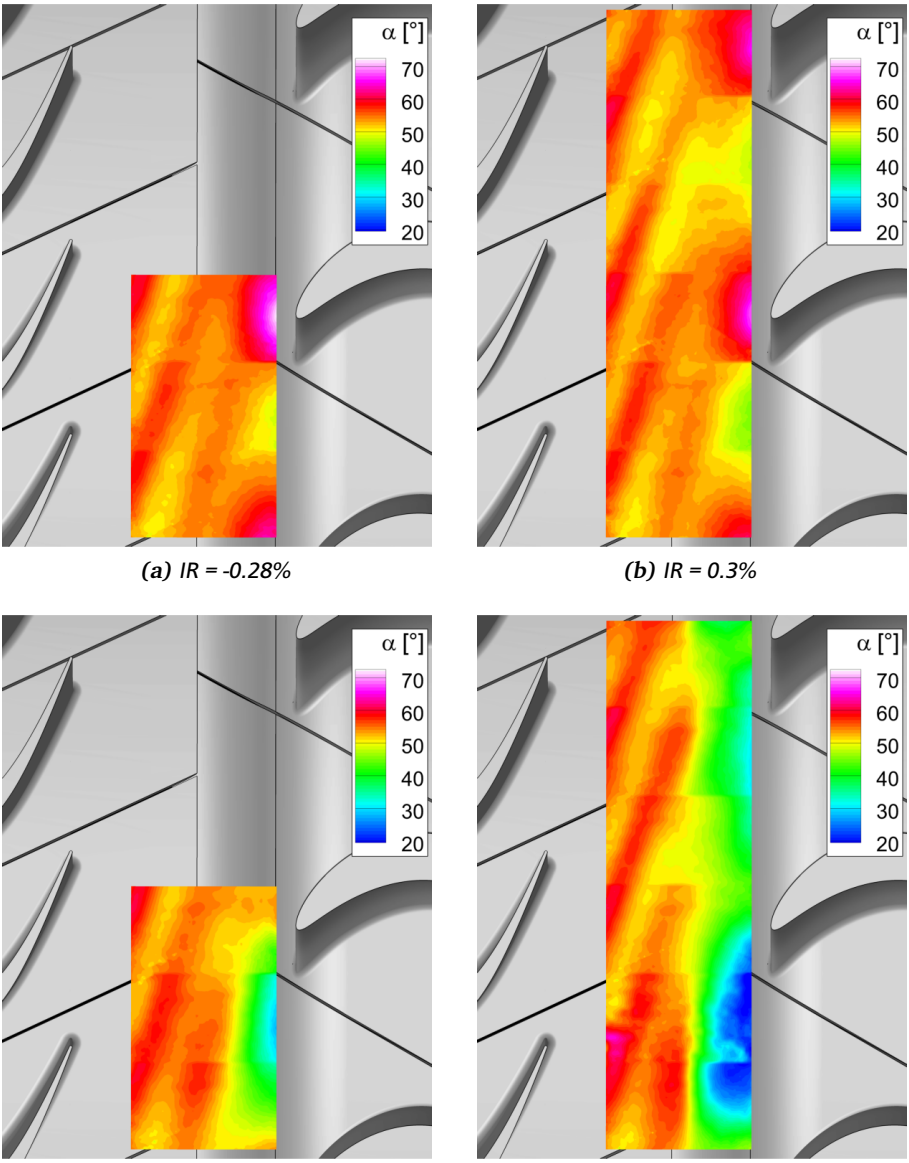

(a) IR = -0.28% *(b) IR = 0.3%*

(c) IR = 1.0% *(d) IR = 1.5%*

Figure 6.19: *Distribution of yaw angle upstream S2 at 3.3% channel height*

but less intense with a maximum decrease of 30°-40° if the purge flow is increased from its minimum to its maximum. At the highest purge flow rate the yaw angle decreases over the whole sector shortly downstream of the trailing edge of the rotor platform. Hence, a significant negative incidence situation results from the increased purge flow at the stator row. This is in agreement with the results gathered from the platform pressure distribution shown previously in Fig. 6.8, which show the stagnation point to move towards the suction side of the vane. The negative incidence angle which is induced by the purge flow has also been found by authors who studied a configuration where purge flow enters upstream of a rotor row. For instance, Reid et al. [88] examined upstream of the rotor at 3% channel height a value of approximately 10-35 degrees, whereas this value depends on the pre-swirl of the purge flow. Caused by the negative incidence, the flow around the vane changes in the current configuration. As it is shown in Fig. 6.19 d, this particularly eliminates the increased turning towards the suction side at the vanes leading edge.

In addition to the general reduction of the yaw angle, there is again a structure visible in the lower part of Fig. 6.19 d which is neither rotor nor stator periodic. This structure reveals that the influence of the drive arm hole jets is still existing at this channel height. As the structure possesses a decreased yaw angle, it is probably caused by an increased amount of purge flow in this area.

If lastly the lowest purge flow rate of -0.28% is compared with the engine representative case of IR = 0.3%, a slightly increased yaw angle is observed. This would probably yield a slightly positive incidence situation at the vanes leading edge. However, since the vane has been designed without purge flow, this statement should be treated with caution.

To identify the main contributor to the negative incidence in the main flow at high purge flow rates, Fig. 6.20 shows the axial and tangential velocity component in the next step. These results are obtained at 3.3% channel height and are shown for IR = 1.5%. Examining the tangential velocity component V_θ, a clear correlation with the yaw angle shown previously in Fig. 6.19 d is detected. From this it can be concluded that the reduced tangential velocity is the main reason for the negative incidence in the main flow.

If the axial velocity component V_x is assessed, a distinct zone of increased velocity is determined in the lower part of the Fig. 6.20 b. This zone coincides with the region of the most reduced yaw angle, which has previously been shown in Fig. 6.19 d. Since this zone is also present once in a periodic sector, it is related to the drive arm hole jets and is probably caused by an increased outflow of purge flow in this area. The increased axial velocity in this area reduces the yaw angle even further and

thus additionally promotes the negative incidence in this area [2]. However, also the tangential velocity component V_θ has a peak in this area. Along the entire periodic section, the reduced tangential velocity V_θ is the main contributor to the reduced yaw angle and hence negative incidence situation.

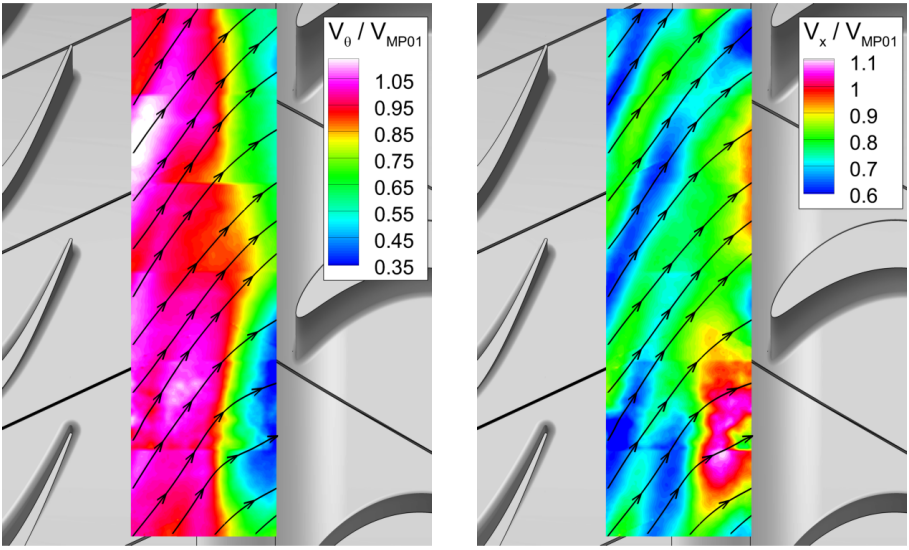

(a) Tangential velocity component *(b) Axial velocity component*

Figure 6.20: *Distribution of axial and circumferential velocity at 3.3% channel height; IR = 1.5%*

To assess the incidence situation between the measurement planes at -2% and 3.3% channel height, Fig. 6.21 illustrates the circumferentially averaged flow situation at the hub-side platform upstream of the stator 2 leading edge. These results are obtained by Schmid et al. [95] using numerical simulations. At this position, there is still a variation of the yaw angle by almost 90° visible. In addition, this figure illustrates well the detrimental flow situation at the stator vane at IR = 1% or IR = 1.5%.

[2] This statement seems to be in contrast to the explanation provided in Chapter 2.3, where it was assessed that an increased axial velocity of the purge flow reduces the negative incidence. However, in that case only the purge flow vector was observed, which is directed in negative y direction. As the main flow still is oriented in positive Y direction at 3% channel height, the increased axial velocity yields a negative incidence in the current situation

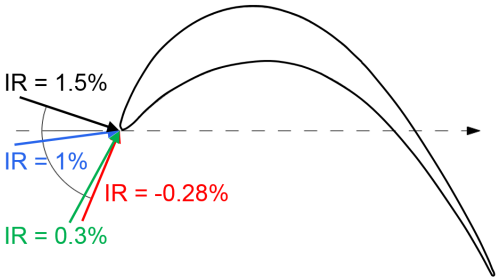

Figure 6.21: *Stator 2 leading edge incidence situation at the radial position of the platform surface; adapted from Schmid et al. [95]*

Comparing finally the flow field within the rim seal and the one in the main annulus a significant difference between the flow direction and the velocity of both streams is apparent. This yields mixing losses which are caused by shear layers between the two flows. According to Denton [19], the mixing losses primarily depend on the fraction of injected fluid and the difference in velocity and flow direction of the mixed flows (see Equation 5.10 in Chapter 5.5). As it has been shown, the divergence in flow direction increases with increasing purge flow. In contrast, the difference in velocity decreases if the purge flow increases to values exceeding an IR of 0.3%. If the flow field measured at -2% channel height is used as a representative value for the purge flow and the data from the 5HP at MP03 are used as representative values for the main flow, it can be shown that the mixing losses increase all in all with increased purge flow. For this purpose Denton's simplified equation to assess mixing losses which is provided in Chapter 5.5 has been used. However, an exact quantification of the rise in mixing losses from the existing measurements is delicate since it is sensitive to the choice of the control volume and boundary conditions. Especially the recirculation zone within the rim seal makes the definition of boundary conditions for the calculation very error-prone. Thus only the trend of increased mixing losses, which is assessed from the available experimental data is given here, but not an exact number. Nevertheless the increased mixing losses are the fourth source of loss identified from the measurements.

In the next step, the flow field obtained from the radial measurement planes is presented for the four different purge flow rates. For this purpose, first the axial velocity V_x at a plane located upstream of the leading edge (Position **I** in Fig. 6.14) is shown in Figure 6.22. Examining this velocity component, the main flow and the purge flow can be differentiated easily from each other due to the different velocity

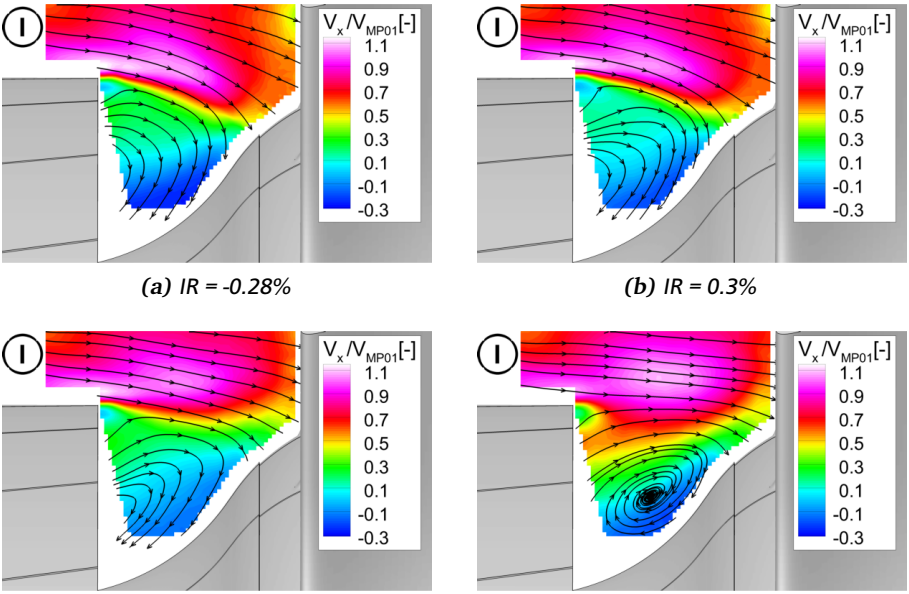

(a) IR = -0.28% *(b) IR = 0.3%*

(c) IR = 1.0% *(d) IR = 1.5%*

Figure 6.22: *Distribution of the axial velocity V_x at a plane located upstream of the leading edge of stator 2 (position indicated by I in Fig. 6.14)*

magnitudes. For the low purge flow rates up to 0.3% it is in addition revealed that the main flow is displaced towards the hub side endwall. This displacement and the partial ingestion (thus removal) of main annulus flow, which can be seen from the in-plane streamlines, leads to a thin boundary layer at the hubside endwall. This coincides with the observations from Popovic and Hodson [78], who state that a part of the boundary layer is removed in the region of hot gas ingestion.

If the purge flow is increased to values exceeding 1%, the displacement of main flow towards the hubside endwall is reduced. Instead, a layer of fluid with reduced velocity is shifted between the main flow and the endwall. Even though it will be shown below in this chapter that the flow field is significantly altered in circumferential direction for IR = 1.5%, this behaviour is observed at all radial planes. It finally thickens the boundary layer upstream of the vane row.

To investigate the in- and outflow of fluid at different purge flow rates, Fig. 6.23 presents next the radial velocity component. Observing the four different purge flow

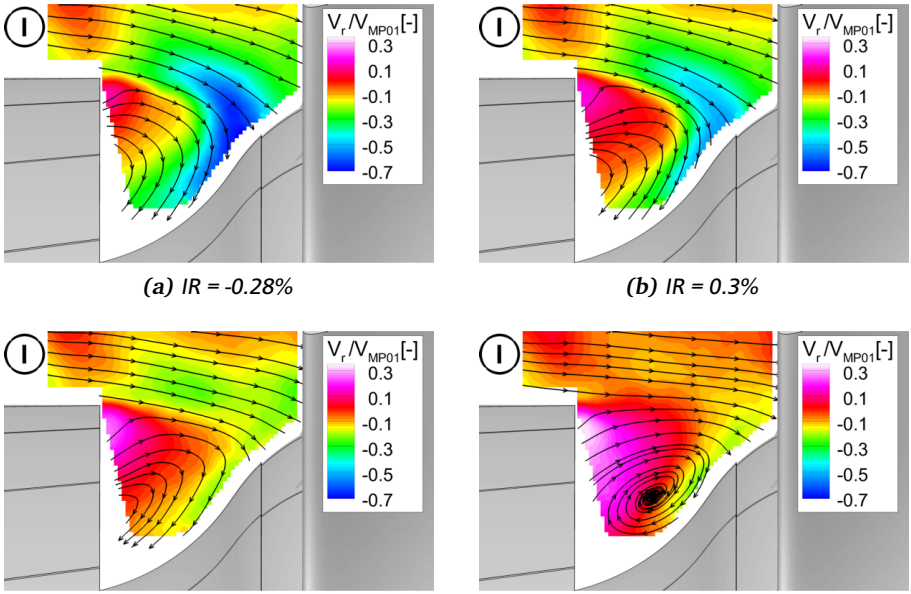

(a) IR = -0.28% *(b) IR = 0.3%*

(c) IR = 1.0% *(d) IR = 1.5%*

Figure 6.23: *Distribution of the radial velocity V_r at a plane located upstream of the leading edge of stator 2 (position indicated by I in Fig. 6.14)*

rates, it is clearly visible that the egress increases with increased purge flow rates downstream of the rotor platform. Simultaneously, the region of negative radial velocity decreases in size and magnitude upstream of the stator vane. This imposes that the ingestion of main flow into the rim seal is reduced. For the highest injection rate a significant reduction of ingress is observed, even though the most critical plane located upstream of the vanes leading edge is presented. It seems that only fluid is ingested into the rim seal which has previously been ejected underneath the rotor platform. In addition to this, a change of the flow structure is observed for the highest purge flow rate. The centre of the recirculation zone changes its position and is now located in the area accessible by the PIV system.

To compare the in- and outflow of fluid at the whole periodic sector for the different purge flow rates, Fig. 6.24 shows next the values at -2% channel height interpolated from all radial measurement planes. The dashed line represents the value of zero, indicating the border between inflow and outflow.

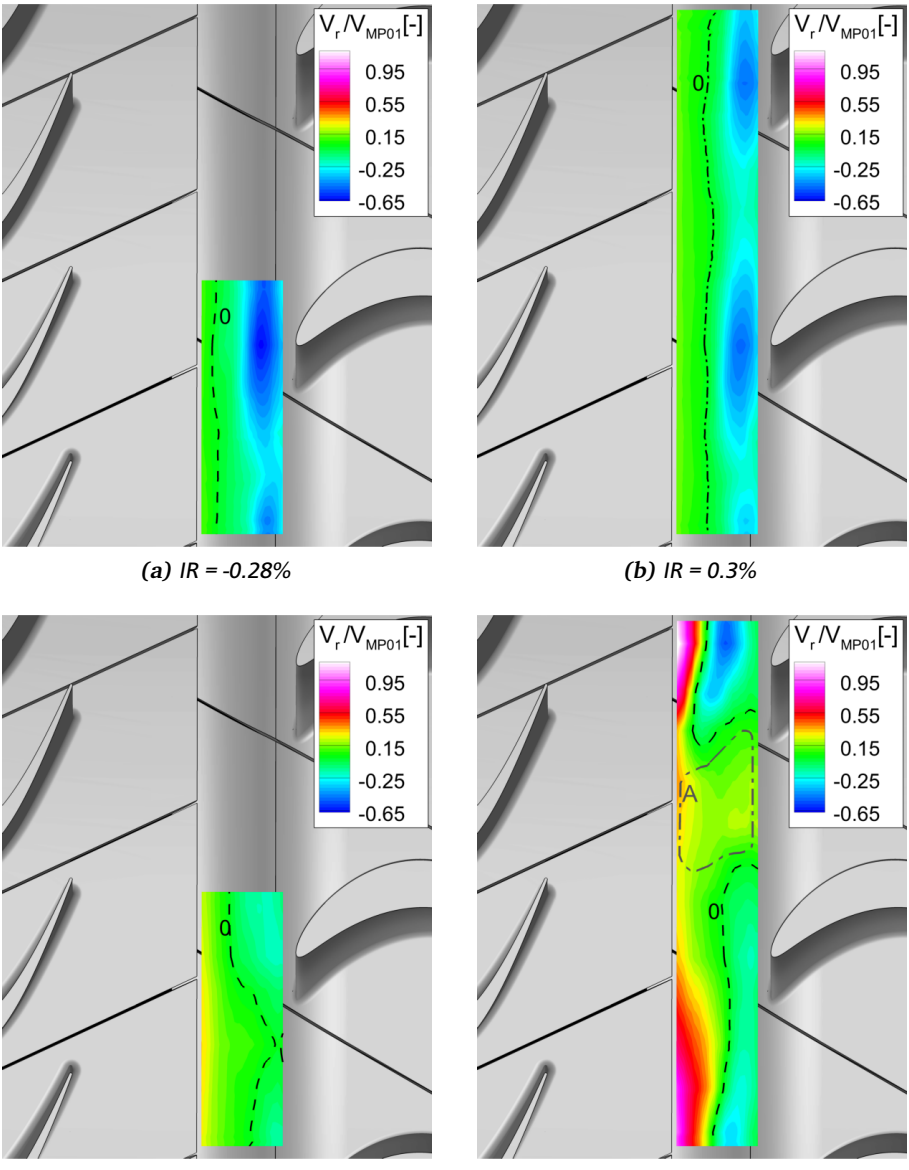

(a) IR = -0.28%

(b) IR = 0.3%

(c) IR = 1.0%

(d) IR = 1.5%

Figure 6.24: *Distribution of the radial velocity V_r at -2% channel height, interpolated from the radial measurement planes*

From this figure it gets obvious that the regions of ingress decrease, both in magnitude and in size, if the purge flow is increased. Simultaneously, the regions of egress increase. Observing the flow structure in detail, a distinct zone of ingress is visible upstream of the vanes leading edges for IR = -0.28% and 0.3%. Yet, if the purge flow increases to IR = 1.5% this typical flow structure disappears. Instead there is again the structure visible, which is neither rotor nor stator periodic and is related to the drive arm hole jets. In this structure, there is still a region of negative velocity visible in a large part of the flow field. However, taking into account the results shown before in e.g. Fig. 6.23, it seems that this negative velocity results rather from the recirculation zone in the rim seal than from the ingestion of main annulus fluid. Between the zones of negative radial velocity there is also a zone visible which features purely outflow of fluid (labelled with **A** in Fig. 6.24 d).

To study the unperiodic structure and thereby the influence of the drive arm hole jets in more detail, Fig. 6.25 shows the recirculation zone in terms of in-plane streamlines at all measured radial planes for IR = 1.5%. At the planes where a recirculation zone respectively vortex is identified, only the streamlines that belong to the vortex are shown. At the planes where no discrete vortex is identified, the general flow field within the rim seal is illustrated.

For simplicity the identification of the vortices is done by visual examination of the in-plane streamlines. Since the vortices are clearly visible, this method gives qualitatively satisfactory results. To provide some information about the radial position of the vortex cores they are marked with circles. The colour of these circles indicates the radial position in percent of the relative channel height, whereas 0% channel height is located at the hub side endwall of the rotor platform. In addition to the vortices, a line that runs through the vortex centres is shown in pink colour in Fig. 6.25.

Observing the different planes it gets obvious that a vortex develops in the upper part of the figure. This location coincides with the region of increased velocity and negative yaw angle which has been ob-

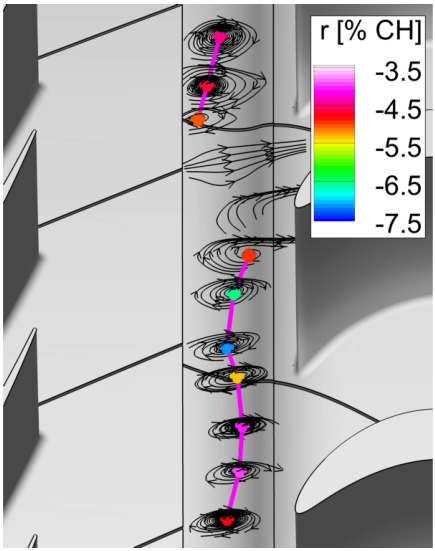

Figure 6.25: *In-plane streamlines within the rim seal; IR = 1.5%*

served previously at -2% channel height in Fig. 6.17 and 6.18. In the rotor relative frame of reference, this vortex moves in direction opposite to the rotor rotation through the rim seal by about one and a half stator pitches. Afterwards, the vortex seems to be bended into the main flow where it possibly interacts with the secondary flow structures. Unfortunately, a detailed study of this process is not possible with the used measurement techniques due to restricted accessibility.

During its propagation through the rim seal the vortex core gets shifted in radial and axial position. Especially upstream of the leading edge of the middle vane the vortex core is moved upstream and radially inwards. In the lower passage the vortex core is shifted in contrast radially outwards. Between the region where the vortex disappears and the origin of the next one, a considerable change in the flow structure is visible. In this area almost no recirculation of the flow is visible but rather a uniform outflow of fluid which covers the whole rim seal cross section area. This region coincides with the zone labelled with A in Fig. 6.24 d. All in all, it looks like the continuous vortex within the rim seal, which has been observed for IR = 0.3%, is splitted in single discrete vortices due to the drive arm hole jets. Furthermore it seems that the vortex in the upper part of Fig. 6.25 is caused by one drive arm hole jet and that the vortex in the lower part is caused by the next jet in rotor rotational direction. This assumption will be substantiated later in Chapter 6.3, where it is shown that the discrete vortex observed in Fig. 6.25 is shifted together with the rotor and hence the drive arm hole position. This finally also proves that the unperiodic structure observed before is caused by the drive arm hole jets and not by any other effect such as the interaction between rotor and stator rows.

If the trajectory of the vortex is compared with the distribution of the yaw angle at -2% channel height, which has been shown in Fig. 6.19, a clear correlation gets obvious. On the one hand, a peak in negative yaw angle is observed at the location where the vortex appears the first time. On the other hand, the negative yaw angle is elevated in regions where the vortex is located radially outwards, cutting the plane at -2% channel height. Simultaneously, the negative yaw angle is less intense in the region where the vortex descends radially inwards. Finally a small region of elevated negative yaw angle is visible in the region where the vortex dissappears and probably enters into the main flow. From this correlation it can be concluded that the vortex contains fluid with a negative yaw angle. As it has been shown previously, a negative yaw angle is an indicator for the presence of purge flow. From this it can be concluded that the vortex is fed by purge flow and transports a part of the purge flow through the rim seal.

The latter fact might explain to some extent the zone of a significantly decreased yaw angle, which has been observed in the lower part of Fig. 6.19 d. In this

area the “purge flow filled vortex” is positioned radially outwards. Thus, in this area the main flow is probably more influenced by this vortex, which owns fluids of a reduced yaw angle. However, as is has been shown in Fig. 6.20 b, there is also an increased axial velocity visible in this area. From this it can be concluded that an increased amount of purge flow enters from the rim seal into the main flow in this area. Even though not shown here, this can be proved by the radial measurements. Overall it is assumed that both effects, the position of the vortex and the increased outflow of purge flow contribute to the zone of significantly decreased yaw angle in this area. As this zone is only present once per drive arm hole, it may finally explain the regions of increased underturning that have been assessed downstream of the stator row by Linker [55] (see Fig. 2.13). That is, the reduced yaw angle probably increases the crossflow within the passage and thus the secondary flow structures. As a result, zones of increased underturning may develop due to intensified secondary flows. Yet, this assumption has not been verified in this thesis and may be part of future research.

Another effect which can be explained by the “purge flow filled vortex” is the reduced fluctuation of the adiabatic cooling effectiveness at the stator platform, which has been derived from Fig. 6.9. Caused by the “purge flow filled vortex”, the typical structure of increased purge flow egress in the passage and reduced egress upstream of the leading edge of a vane disappears. Instead a large part of the rim seal surface is covered by purge flow, leading to a more uniform distribution of the adiabatic cooling effectiveness.

Summarising the influence of different purge flow rates on the flow field within the rim seal, the following most pronounced effects are observed. On the one hand the purge flow injection causes a negative incidence situation at the subsequent stator row. On the other hand a significant influence of the drive arm hole jets has been revealed for the highest purge flow rates.

Flow within the Stator 2 Passage

In this section the flow field within the second stator row is investigated. The primary purpose of this investigation is to relate the effects obtained within the rim seal to the ones obtained downstream of the stator row at MP04. For this purpose the pressure distribution and the adiabatic cooling effectiveness at the profile of the vane is presented.

The profile pressure distribution is obtained from the static pressure taps at 5%, 20% and 50% channel height and presented in form of the pressure coefficient

C_p, defined in Chapter 5.2.3. Figure 6.26 a shows the pressure coefficient at 5% channel height. Comparing the different purge flow rates, a decrease in pressure close to the leading and trailing edge is observed at the pressure side of the vane in case the purge flow rate is increased. At the suction side the pressure is in contrast increased over almost the entire part of the vane, whereas the increase is most intense in the front part. The only exception for this is the injection rate of 0.3%, which shows a decreased pressure in the rear part of the vane.

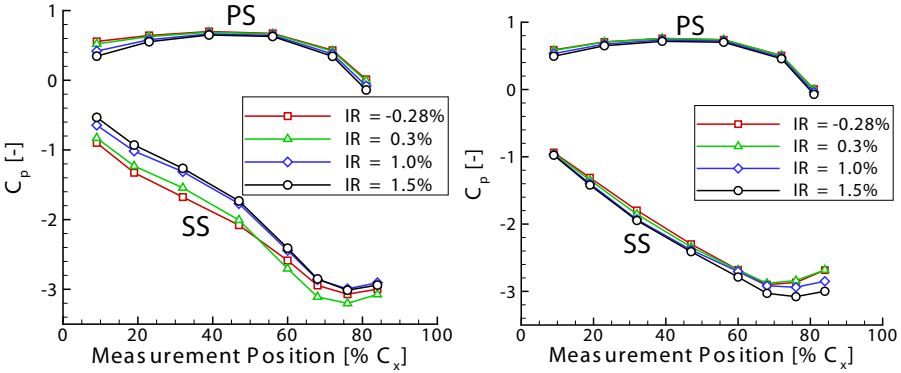

(a) *5% channel height* ***(b)*** *20% channel height*

Figure 6.26: *Profile pressure distribution at 5% and 20% channel height*

The elevated pressure at the suction side of the vane can be explained by the increased negative incidence at the stator 2 leading edge, which has been observed by the use of PIV and the pressure measurements at the platform. Caused by the negative incidence the stagnation point moves towards the suction side. This in turn reduces the acceleration along the suction side and hence yields an increased pressure. In addition, the flow might "hit" the suction side surface and thus additionally increases the pressure. The decrease of pressure in the rear part of the vane at IR = 0.3% might be explained by the passage vortex, which possibly attaches at this purge flow rate in the region of the pressure taps located in this area. There it decreases possibly the pressure due to increased losses or intensified velocities within the vortex. For the higher seal air rates the passage vortex is supposed to be shifted to higher channel heights and thus does not influence the rear part of the vane such pronouncedly close to the hub. This can be seen by means of the profile pressure distribution at 20% channel height, shown in Figure 6.26 b.

At this channel height there is almost no influence of the purge flow visible close to the leading edge, both at the suction as well as at the pressure side of the vane. However, close to the trailing edge the pressure drops at purge flow rates exceeding an IR of 1%. This pressure drop might again be explained by the passage vortex which is shifted radially outwards with increased purge flow.
Overall, the loading of the vane is decreased at 5% channel height and increased at 20% channel height. At 50% channel height there are almost no changes observed. Therefore, this channel height is not presented here.
The decreased loading of the vane at 5% channel height is somehow contradictory to the increased secondary flow structures which have been observed at MP04 (see Chapter 6.1.2). According to e.g. Perdichizzi and Dosenna [73], a decreased loading leads to a reduced pressure gradient between the suction and the pressure side. This in turn reduces the crossflow and hence the secondary flow structures. However, as shown by Popovic and Hodson [78], the negative incidence originating from the purge flow upstream of a blade can promote the crossflow within the passage. This probably overcompensates the decreased pressure gradient between the pressure and the suction side. Hence, the strong negative incidence at the vanes leading edge is supposed to be the main reason for the intensified secondary flow structures downstream of the vane.
To examine this in more detail the adiabatic cooling effectiveness η_{aw} has been obtained from CO_2 measurements at the profile. The results are shown at 5% and 20% channel height in Fig. 6.27 and 6.28. The adiabatic cooling effectiveness provides on the one hand an information about the potential cooling which can be achieved using purge flow. On the other hand it allows to track respectively "visualise" the purge flow, which is in the current case of primary concern.
At 5% channel height an increase of the cooling effectiveness up to an axial position of 60% C_x is observed at the suction side of the vane for low purge flow rates. Further downstream the cooling effectiveness decreases again. If the injection rate is increased to 1.5% the overall level of η_{aw} increases continuously to a maximum value of 38%. This implies a better cooling of the suction side surface for increased purge flow rates in terms of less mixed out coolant flow at the endwall. But the more interesting observation is that the peak value of the curves moves about 20% C_x axially upstream. Assuming that the purge flow mainly enters the pressure side leg of the horseshoe vortex and the passage crossflow, this suggests that the location where the pressure side leg of the horseshoe vortex attaches at the suctions side of the vane is shifted upstream. This is in analogy to the observations obtained by Popovic and Hodson [78] in a linear cascade. Furthermore Pueblas et al. [81] confirm this behaviour for the current configuration using numerical simulations.

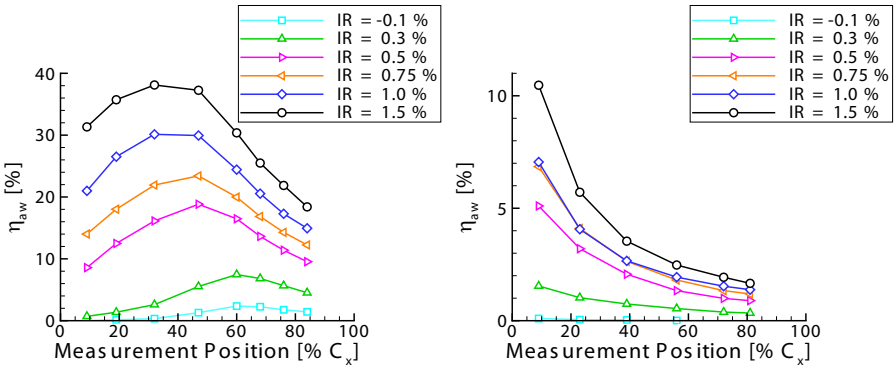

(a) *suction side* **(b)** *pressure side*

Figure 6.27: *Adiabatic cooling effectiveness at 5 % channel height*

At the pressure side the adiabatic cooling effectiveness is considerably lower compared to the suction side surface. In addition, only the front part of the vane experiences an increased cooling effectiveness. This confirms the assumption that most of the purge flow is guided by the cross flow or the pressure side leg of the horseshoe vortex from the pressure side to the suction side of the vane.

At 20% channel height the maximum in adiabatic cooling effectiveness is observed at the rear part of the vanes suction side (Figure 6.28 a). Furthermore there is almost no purge flow present at the pressure side [3]. This shows that the purge flow has completely been transferred to the suction side at this channel height. If the results at the suction side are examined in more detail, the peak region of η_{aw} is moved upstream at increased purge flow, similarly to the case at 5% channel height. In addition, η_{aw} increases with increasing purge flow, whereas its peak value is slightly above the value at 5% channel height at the same axial position for IR = 1.5%. This increased cooling effectiveness at 20% channel height and the reduced one at 5% channel height shows that the passage vortex, which mainly contains the purge flow, is already shifted radially outwards within the stator passage.

Summarizing the effects above, the radial shift of the secondary flow structures observed at MP04 in Chapter 6.1.2 may be explained as follows. As it has already been shown by PIV, the purge flow injection causes a negative incidence at the

[3] The obtained results at the pressure side at 20% channel height are within the measurement uncertainty of the CO_2 measurement system. This also explains the slightly negative values.

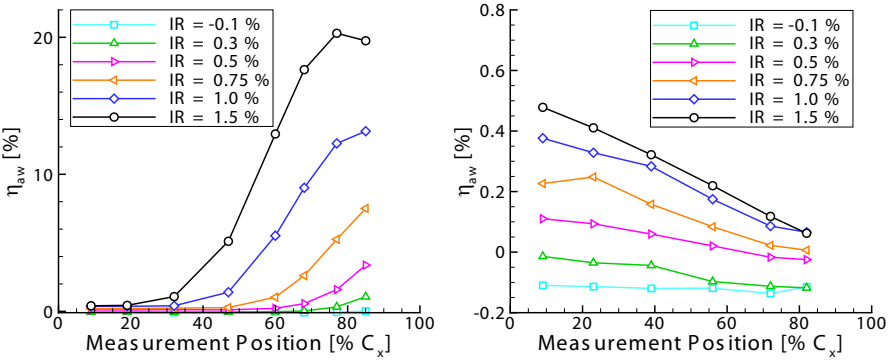

***(a)** suction side* ***(b)** pressure side*

***Figure 6.28:** Adiabatic cooling effectiveness at 20 % channel height*

leading edge of the vane which attenuates the crossflow in the passage. This in turn leads to an earlier attachment of the pressure side leg of the horseshoe vortex at the suction side of the vane as it is shown by the measurements of the adiabatic cooling effectiveness. Consequently, the passage vortex develops further upstream and experiences a longer propagation through the passage during which it migrates outwards. In addition to this mechanism, the discrete vortex in the rim seal, which is induced by the drive arm hole jets, might influence the development of the secondary flow structures when it enters into the main flow.

For the lowest purge flow rate the same explanation provided above can be used to explain the reduced secondary flows at MP04 which have been observed at this flow rate (see Fig. 6.7). For this purge flow rate a rather positive incidence has been observed. This may lead in conjunction with the partially removed boundary layer to a reduced crossflow within the passage. Thus the passage vortex develops further downstream and migrates less outwards.

Overall, the flow around the vane is changed, leading to flow conditions the vane was originally not designed for. This might lead to additional losses such as increased profile losses or even separation zones and is hence the fifth possible source of losses identified from the measurements. However, these losses can not be quantified separately since they merge with the secondary flow losses at the downstream measurement plane.

6.1.3 Sealing Effectiveness and Pressure Distribution within the R1S2 Wheelspace

To quantify the ingestion of main annulus flow into the inner rotor-stator wheelspace the sealing effectiveness η_s, which has been described in Chapter 2.2.1, is measured within the wheelspace and presented in Fig. 6.29 a. Two different positions have been chosen for this and are illustrated in Fig. 6.29 b. One is located underneath the stator lip, the other one at the stator disc which attaches the labyrinth seal to the stator platform. For each radial position the sealing effectiveness has been measured at three circumferential positions to check the uniformity of the results in circumferential direction.

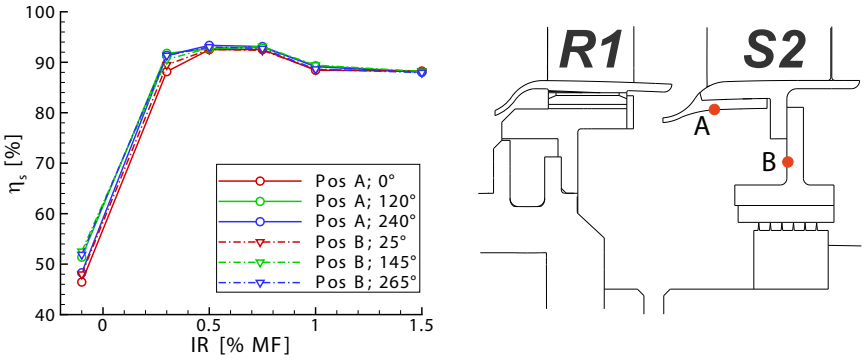

***(a)** Sealing Effectiveness* ***(b)** Measurement Positions*

***Figure 6.29:** Sealing Effectiveness of the R1S2 wheelspace for various purge flow rates*

Examining the results, a sealing effectiveness of 46-52% is already achieved for IR = -0.1%. If the injection rate is increased to 0.3% the sealing effectiveness rises very sharp to values of about 88% - 91%. However, a further increase of the purge flow leads only to a moderate increase of η_s to maximum values of up to 93%, whereas this peak value is reached at an IR of 0.5%. If the purge flow is increased even further to values of up to IR = 1.0% or 1.5%, the sealing effectiveness decreases slightly to values of 88%. Thus, the sealing effectiveness does not reach a value of 100%, which implies that the wheelspace is not fully sealed. This is the case for both measurement points, which show all in all the same values.
The decrease of the sealing effectiveness with increasing purge flow is a crucial detection, as the additional use of costly compressor bleed air as purge flow has

rather detrimental than beneficial effects. In addition, all the models to assess the rate of hot gas ingestion presented in Chapter 2.2.2 yield a rise of the sealing effectiveness with increased purge flow.

In addition to the decreasing sealing effectiveness at high purge flow rates, another interesting observation is gathered from the pressure measurements in the wheelspace. Therefore, Fig. 6.30 shows the pressure distribution above and underneath the stator platform. The pressure at the stator lip is taken from the pitch-wise instrumentation 4% C_x upstream of the stator leading edge, which has already been shown in Chapter 6.1.2. The pressure within the wheelspace is taken at point **A** which is illustrated in Fig. 6.30 b. Since only one pressure tap is available every 120 degrees at this position, a constant pressure is displayed in circumferential direction. Examining the results it gets obvious, that the pressure in the wheelspace decreases if the purge flow rate is increased above 0.3%. The pressure at the stator platform stays in contrast almost at the same level. Thus, the pressure difference between the platform and the wheelspace increases with increasing purge flow, featuring a lower pressure in the cavity. Even though not shown here, the same trend is observed if the static pressure close to the hub at MP03 is taken as the main annulus pressure or if the point **B** in Fig. 6.30 b is used as the wheelspace pressure. This proves that the location where the static pressure is gathered from does not change the general trend of an increased pressure drop across the seal. The reason for the decreased pressure is assumed to be the increased swirl in the wheelspace which has been derived from the results of the PIV measurements in Chapter 6.1.2 (see page 84). This increases the tangential velocity and thus reduces the static pressure.

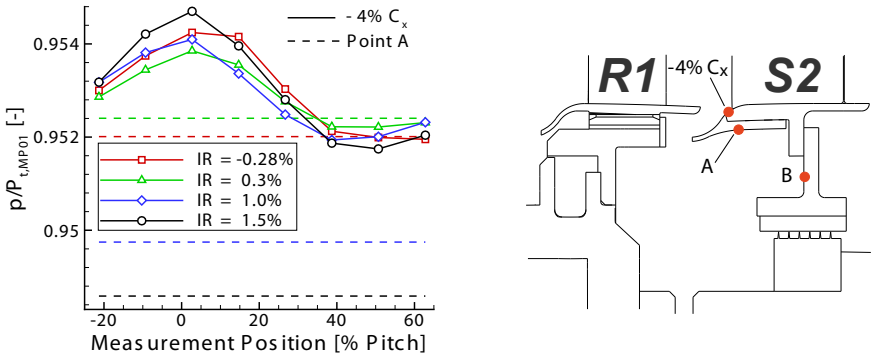

***(a)** Pressure distribution* ***(b)** Measurement Position*

***Figure 6.30:** Pressure at the stator platform and within the rim seal*

This decreased pressure in the cavity is another crucial observation from the measurements. In several publications the pressure difference between the main flow and the wheelspace is used to assess the flow across the rim seal. For instance Bayley and Owen [4], Phadke and Owen [74], Dadkah et al. [16] and Chew et al. [13] apply a pressure criterion to assess if any hot gas ingestion is present, assuming that the wheelspace is fully sealed if the wall pressure in the wheelspace is above the static pressure in the main annulus. This pressure criterion would certainly lead to confusable results in the current configuration. That is, the criterion might reveal correctly that the wheelspace is never fully sealed, since the wheelspace pressure at point **A** and point **B** is always below the peak pressure at the stator platform. However, it will also suggest that there is a higher ingestion for IR = 1.5% than for IR = -0.1%, what is truly not the case.

In addition to the use of a pressure criterion, several simple orifice models are described in the literature (see Chapter 2.2.2). These use the static pressure difference across the rim seal to assess the velocity and hence the mass flow through it. If these models neglect the swirl within the wheelspace as e.g. the one described by Johnson et al. [41], they will predict an inflow of fluid, which is proportional to the decreased pressure within the wheelspace. Thus, they will also fail to correctly estimate the rate of ingestion. Models that consider the swirl within the wheelspace, as e.g. the one from Owen [64], show that an increase of the swirl in rotational direction of the rotor decreases the ingestion and thus compensates to some extend the increased pressure drop measured across the seal. Thus, these models seem, if at all, more appropriate for the current configuration. However, since the tangential velocity component within the wheelspace has not been measured an application and verification of these models is not feasible in this thesis.

6.2 Summary and Discussion of Results for the Baseline Configuration

Summarizing the results obtained from the baseline drive arm hole configuration the following most important effects are obtained:

- The efficiency of the turbine decreases with increasing purge flow.
- The purge flow acts as a blockage to the main annulus flow, decelerating and redistributing it towards the outer casing.
- Caused by the purge flow injection a negative incidence situation develops at the vane row downstream of the rim seal.

- The boundary layer at the hub side endwall is thickened with increasing purge flow.
- The crossflow within the stator passage attaches further upstream at the vanes suction side at raised purge flow rates.
- The secondary flow structures within the stator passage are intensified and shifted radially outwards if the purge flow increases.
- The purge flow enters mainly into the area of the passage vortex, but is not located exactly in its centre.
- The inflow conditions for the subsequent rotor row are changed.
- The divergence in flow direction between the main flow and the purge flow increases with increasing purge flow, leading to increased mixing losses.
- At moderate purge flow rates, the ingestion of main annulus fluid is most intense upstream of the vanes leading edge.
- At high purge flow rates a drive arm hole periodic structure develops within the rim seal, which features one discrete vortex per drive arm hole.
- The sealing effectiveness decreases slightly if the purge flow is increased above a certain value.
- The pressure difference across the rim seal increases with purge flow, featuring a lower pressure in the wheelspace.

As it has already been mentioned during the presentation of the results, most of these effects have already been found in the literature for configurations where the purge flow enters into the mainflow upstream of a rotor row. This is especially the case for the basic influence of the purge flow on the main annulus flow, even though quantitative values as the radial migration of the secondary flows or their intensification might be different. Thus, one main conclusion from the baseline measurements is that the observed effects are in principle the same whether the purge flow is injected upstream of a rotor or upstream of a stator row (at least for the configuration studied here).
However, as it will be explained here, the driving mechanisms for some of the effects are different in the current configuration. If for instance the incidence situation upstream of the stator vane is investigated in detail, in the first instance it seems to match well with the observations obtained upstream of a rotor row by other authors. In both configurations an increased purge flow leads to an increased negative incidence upstream of the subsequent blade or vane row. Howsoever, upstream of a rotor row the increased negative incidence is caused in general by a

reduced tangential velocity in rotor rotational direction and/or by an increased axial velocity [4]. While the increased axial velocity might be caused by purge flow that is fed into the main flow with a high velocity, the reduced tangential velocity is caused by a reduced swirl of the purge flow. The latter fact is shown by e.g. Vaugham [107], who shows that an increased coolant flow delivery reduces the swirl in a rotor-stator system (for unswirled purge flow delivery). As the axial velocity of the purge flow is in general below the main flow velocity, the reduced swirl seems to be the main contributor for the negative incidence. This is in agreement with observations from Reid et al. [88], who show that a reduced tangential velocity at the hub is the primary reason for the purge flow induced negative incidence at the rotor row of the turbine he investigated.

Upstream of a stator row the intensified negative incidence at raised purge flow rates is in contrast caused by an increased tangential velocity component in rotor rotational direction and/or an increased axial velocity component. As it has been shown by PIV, this increased tangential velocity of the purge flow in rotor rotational direction is the primary reason for the increased negative incidence in the actual configuration. This increase in tangential velocity is primarily caused by the increased swirl of the purge flow within the rim seal and wheelspace. The reason for this increased swirl is assumed to be the delivery of the purge flow through holes which are located within the rotational frame of reference. Due to this, the purge flow gets injected into the wheelspace with a tangential velocity component similar to the one of the rotor disc at the same radial position. If now the purge flow rate increases, also the mass flow of "preswirled air" increases. Thus, the tangential velocity in rotor rotational direction in the wheelspace is increased. This effect is amplified by the drive arm hole jets which penetrate deeper into the wheelspace at increased injection rates and thus, transport the preswirled air into the outer regions of the wheelspace and the rim seal. Furthermore, a reduced amount of main annulus flow, which possesses a tangential velocity in opposite direction, is ingested at high purge flow rates. This previously had reduced the tangential velocity in rotor rotational direction at low purge flow rates.

Overall, the increased swirl of the purge flow and the correlated negative incidence upstream of the stator is the main reason for the similar influence of the purge flow on the main flow aerodynamics in the actual configuration.

[4] Strictly speaking also a reduced axial velocity can cause a negative incidence, as it has been shown in Chapter 2.3. However, this is only the case if the influence of the purge flow is that pronounced that the flow changes its general direction from a positive to a negative yaw angle or vice versa. This might happen very close to the hub at significant purge flow rates. Thus the statement depends on the observed channel height.

Since the variation of the swirl and the resulting negative incidence is very strong in the investigated configuration it may possibly also explain why the radial migration of the secondary flows is more pronounced compared to other research data. However, this might not be the only reason for the increased radial migration. There are also geometrical differences existent between the actual and the other geometries. These might additionally influence the radial migration because similar, but less intense variations have also been obtained for different configurations in which the purge flow is injected solely upstream of a rotor row.

In addition, the strong variation of the swirl may explain why the results obtained in this work differ quite significantly from the ones obtained by Schuler et al. [102], [101] even though the geometry is similar. The investigations from Schuler et al. are carried out in a linear cascade where the purge flow is provided without the existence of rotating parts, but at a fixed angle into the wheelspace. Thus the swirl in the rim seal is less influenced by the different purge flow rates.

If the purge flow would be delivered in the actual configuration through ports in the stationary frame of reference without any preswirl, its detrimental effects are assumed to be less pronounced. Yet, in a low pressure turbine this is if at all only possible if the purge flow is fed through the stator vanes into the wheelspace. But this in turn would increase its temperature due to the hot gases surrounding the vanes. In addition, structural constraints need to be considered since especially the last airfoils of a low pressure turbine are usually uncooled and thus are originally not designed for any internal gas paths.

Upstream of a rotor row the preswirled delivery of purge flow is in contrast beneficial as it has been demonstrated by Ong et al. [63] and Reid et al. [88]. As already mentioned in Chapter 2.2.3 it reduces not only the negative incidence and mixing losses but also the total temperature at the rotor disc.

Thus, in summary there is probably not the question whether there is any difference between the purge flow injection upstream of a rotor or a stator row, but rather how the purge flow should be delivered into the wheelspace. There are considerable differences possible and one needs to choose the most appropriate one. In general, it seems beneficial from the aerodynamic point of view to deliver the purge flow preswirled upstream of a rotor row but if possible unswirled upstream of a stator row. This shows that the findings from Ong et al. [63] and Reid et al. [88], who show that an increased swirl of the purge flow in rotor rotational direction has beneficial effects, needs special attention upstream of a stator row. In this case their conclusions are probably not valid.

In addition to the effects which are similar to the purge flow injection upstream of a rotor row, there are also effects detected, which to the author's knowledge have not been presented or studied in detail in the literature so far.

For instance, it has been shown that the flow field within the rim seal is significantly influenced by the drive arm hole jets at a sufficiently high purge flow rate respectively drive arm hole velocity ratio. That is, a purge flow filled discrete vortex appears in the rim seal once per drive arm hole. This vortex suppresses the typical flow structure in the rim seal, which originally shows zones of increased ingestion upstream of the vane's leading edge and zones of increased outflow in the passage of the vane. Instead, the flow field is dominated by the drive arm hole jets, which lead to zones of a significantly negative yaw angle. From this influence of the drive arm hole jets the following important question arises: How do these jets influence the flow field within the main annulus and the generated losses? To answer this question measurements have been carried out at the same purge flow rates but with a different diameter of the drive arm holes. This allows to study the flow field at different drive arm hole velocity ratios, but maintained purge flow rates. The results of these measurements are presented separately in Chapter 6.4.

Another unexpected result is the decreasing sealing effectiveness at increased purge flow rates. Even though Gentilhomme et al. [29] have also observed a slight decrease of the sealing effectiveness by 4-5% if the purge flow is increased above a certain value, all other publications known to the author show a continuous rise of the sealing effectiveness with increasing purge flow. Since a decrease of the sealing effectiveness with increasing purge flow has detrimental effects and counteracts the use of expensive coolant flow, the knowledge of the reasons is essential. Therefore, several possible reasons have been worked out and are presented in Chapter 6.5.

Finally, the question needs to be answered if the examination of the results for a single rotor-stator position is a suitable approach. Even though it looks like the flow field is influenced for low purge flow rates primarily by the stator vanes and for the high purge flow by the drive arm hole jets, it needs to be assessed if the given results are also valid for other rotor-stator relative positions. On the one hand, this allows to clarify that the unperiodic structure originates solely from the drive arm hole jets and not from other, however unlikely effects. On the other hand, it would be interesting to examine the possible influence of the rotor wake on the hot gas ingestion and the flow field within the rim seal. For this purpose the influence of different rotor-stator relative positions has been examined and is presented in Chapter 6.3 below.

6.3 Influence of the Rotor-Stator Relative Position

In this chapter the influence of different rotor-stator relative positions on the flow field within the rim seal is investigated. As it has already been shown in Chapter 6.1.2 there are two different flow regimes visible within the rim seal, which primarily depend on the purge flow rate. For low purge flow rates the flow within the rim seal seems to be dominated by the potential field of the stator vanes. In contrast, the flow field seems to be dominated by the jets that arise from the drive arm holes for the high purge flow rate of 1.5%. However, all the previous results have been obtained for one rotor-stator relative position. In this chapter the influence of different rotor positions is examined to verify whether the previous results are still valid for other rotor-stator relative positions. To account for the different flow regimes this is done separately for IR = 0.3% and IR = 1.5%.

6.3.1 Injection Rate of 0.3%

To investigate the influence of different rotor positions on the flow field within the rim seal, Fig. 6.31 shows the distribution of $V_{x\theta}$ for two different rotor positions at -2% channel height. In addition, the in-plane streamlines are displayed to indicate the flow direction. The rotor-stator position on the left hand side coincides with the one already presented in Chapter 6.1.2 and represents the condition where the middle vane is aligned with a rotor wake at 13% channel height. On the right hand side the rotor position is shifted by half a rotor pitch, leading to interchanged flow condition at the two vanes.

Examining the two different rotor positions, the same flow structure is observed in general. Also, there are only small differences visible in quantitative values. For instance, the velocity at the leading edge of the middle vane is decreased slightly if the second rotor position is considered. Simultaneously, the velocity upstream of the upper vane is increased slightly. As it has been worked out in Chapter 6.1.2, the area of increased velocity is related to an increased amount of hot gas ingestion in this area. Considering this finding, it is expected that the ingestion of main fluid decreases slightly at the middle vane but increases slightly at the upper vane if the second rotor position is observed. This is in agreement with the results obtained from Bohn et al. [5]. They have shown for a configuration where the purge flow enters upstream of a rotor row that hot gas ingestion is more intense if the rotor is exposed to the wake of a stator vane.

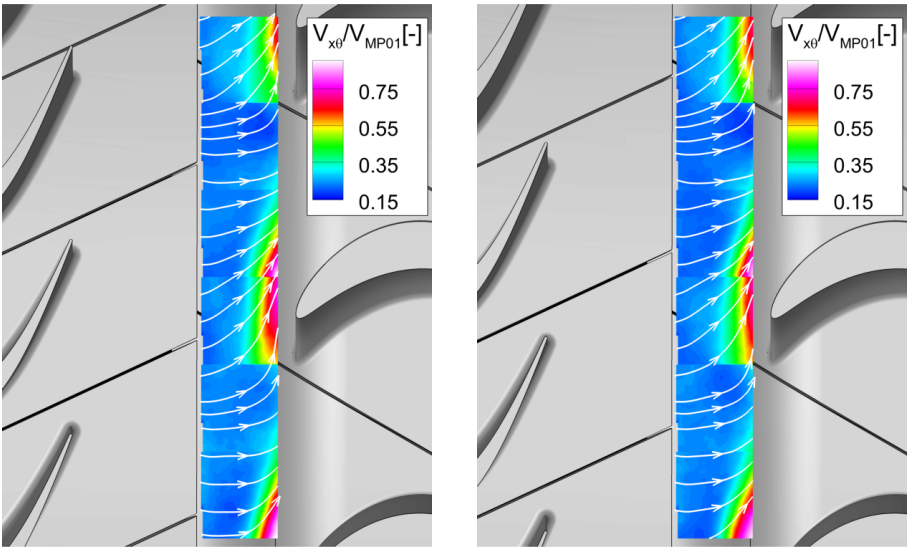

(a) *Rotor 1 reference position* ***(b)*** *Rotor 1 turned by 1/2 rotor pitch*

Figure 6.31: *In plane velocity $V_{x\theta}$ at -2% channel height for 2 different rotor positions.*

Whereas for the sake of clarity only 2 different rotor positions are shown in Fig. 6.31, in total 10 different rotor positions have been measured and investigated. Yet, a detailed examination of these additional positions does not yield significantly different results. For this reason they are not presented here. Instead, results from the radial measurement planes are presented in the next step to study the influence of the different rotor-stator positions in more detail.

For this purpose, Fig. 6.32 shows the radial velocity distribution for the same rotor positions assessed before, whereas the measurement plane is located upstream of the stator 2 leading edge (position indicated by **I** in Fig. 6.14 a). In contrast to the results from the radial measurement planes that have previously been presented, a larger part of the main annulus flow is shown in this figure.

Observing the differences in the flow field between the two rotor positions, the dominant changes are visible within the main annulus. In this area there are distinct zones of positive and negative radial velocity apparent. These regions are supposed to arise from the secondary flow structures which have developed in the upstream rotor row. As expected, these structures change their position if the rotor is turned

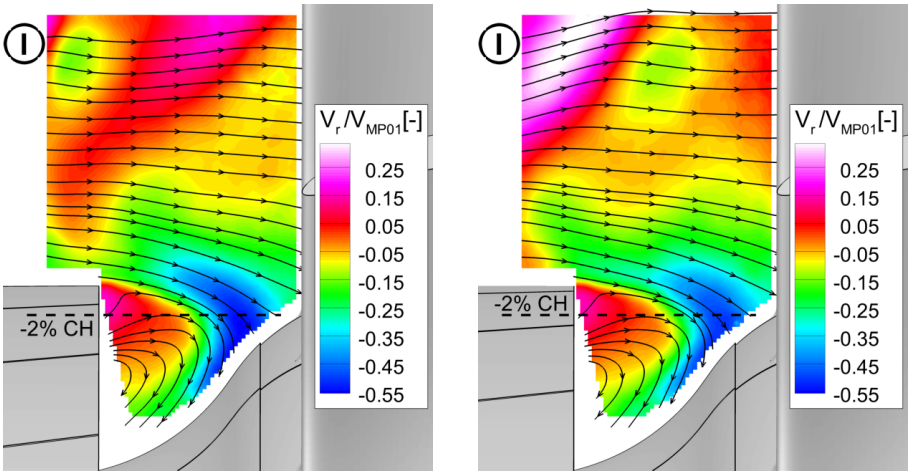

(a) *Rotor 1 reference position* ***(b)*** *Rotor 1 turned by 1/2 rotor pitch*

Figure 6.32: *Radial velocity V_r upstream of the leading edge for 2 different rotor positions*

by half a pitch, modifying also the flow close to the hubside endwall. However, within the rim seal there are only small changes visible. In general, the flow field in the rim seal is more or less unchanged, even though the ingress of fluid is slightly more intense at the reference position, as for the previous results. Thus, the main outcome from these measurements is again that the flow field within the rim seal is varied only slightly at the two rotor positions. A possible reason for this is the less pronounced influence of the wake close to the hub side endwall which has previously been elaborated in Chapter 6.1.2 (see e.g. Fig. 6.12).

As for the measurements at -2% channel height, 10 different rotor positions have been measured for the measurement plane shown in Fig. 6.32, which is located upstream of the stator 2 leading edge. Results from these 10 measurements are presented in Fig. 6.33 a in form of a time space plot. In this plot the radial velocity is extracted from the dashed line shown in Fig. 6.32 which is located at -2% channel height. The abscissa shows the distance from the rotor platform trailing edge, whereas the ordinate is representative of the different rotor positions and the colour indicates the radial velocity V_r. In total one rotor pitch is resolved, whereas the first and the last rotor position is gathered from the same measurement.

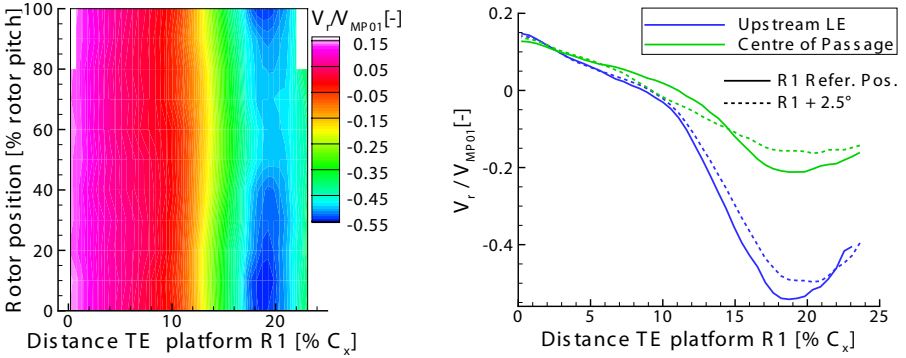

(a) *Time space plot for 10 rotor positions* ***(b)*** *Variation of V_r at different stator positions*

Figure 6.33: *Distribution of radial velocity at -2% channel height*

Examining the time space plot it gets obvious that the strongest rate of ingress is present if the rotor is moved by 10% rotor pitch, which is close to the reference position. The strongest decrease of ingress is observed if the rotor is moved by about 60% pitch. However, comparing the observed variation with the general distribution of the radial velocity in circumferential direction (see Fig. 6.16), the influence of the rotor position seems to be small.

To study this in more detail, the influence of the rotor on V_r at two circumferential positions is shown in Fig. 6.33 b. One position is located upstream of the stator's leading edge and corresponds to the measurement plane indicated by **I** in Fig. 6.14 a. The other position is located at the centre of the passage between two stator vanes. It corresponds to the measurement plane which is located between the ones indicated by **III** and **IV** in Fig. 6.14 a. Again the values are extracted at -2% channel height. The reference position of the rotor is indicated by solid lines, wheras the second position is indicated by the dashed lines. Comparing the variation caused by the two different rotor positions with the one between the different circumferential positions at the stator vane, only a small influence of the rotor is observed. The circumferential variation of V_r is approximately 5 times larger than the one caused by different rotor positions. This again shows that the ingestion is mainly driven by the stator vanes and not the rotor wakes or an interaction between both.

Summarising the results obtained for the different rotor-stator relative positions it can be stated that their influence on the flow field within the rim seal is small compared to the effects caused by the stator vanes. The general flow field is

maintained for all the studied rotor positions. This in turn shows that the results presented in Chapter 6.1.2 for IR = 0.3% are in principle also valid for other rotor positions, even though only a single rotor-stator relative position has been examined.

Regarding the results shown for different rotor positions it has to be kept in mind that the formation of the rotor wakes changes in strength and in position at different channel heights. Thus, it is not fully clear if the increased ingestion at the leading edge for the reference position is definitely caused by the fact that the vane is exposed to the rotor wake, since this could be different close to the hub. However, since the wake at 13% channel height is much more pronounced its trajectory is assumed to be dominant and has been chosen as the representative one. This assumption is supported by the fact that Bohn et al. [5] also found an increased ingestion upstream of a rotor if this one is exposed to the wake of the upstream stator vane.

Comparing finally the current results with the one from Bohn et al. [5], the influence of the rotor wake is less pronounced in the actual configuration. The main reason for this is assumed to be the fact that the axial distance between the trailing edge of the upstream blade row and the rim seal is several times larger in the actual configuration (as percentage in axial chord length).

6.3.2 Injection Rate of 1.5%

At an injection rate of 1.5% a structure is observed within the rim seal which is assumed to arise from the drive arm hole jets. To study the influence of the drive arm hole jets at different rotor respectively drive arm hole positions, results from different rotor-stator positions are examined. This shall also prove the assumption that the unperiodic structure in the rim seal is indeed caused by the drive arm hole jets and not by any other, however unlikely effects such as the rotor-stator interaction. For this purpose, Fig. 6.34 shows the in-plane velocity $V_{x\theta}$ at -2% channel height at four rotor positions, whereas the rotor is turned in total by 1.5 rotor pitches which equals one stator pitch.

Observing the four rotor positions, it is clearly visible that the region of increased velocity, which has previously been identified, is moved analogue to the rotor and thus also the drive arm hole position. In general, both the amplitude of the velocity peak as well as the flow structure are maintained but shifted step by step downwards in the direction of rotor rotation. Since Fig. 6.34 a and c show the same rotor-stator relative position, it follows that the unperiodic structure is primarily related to the

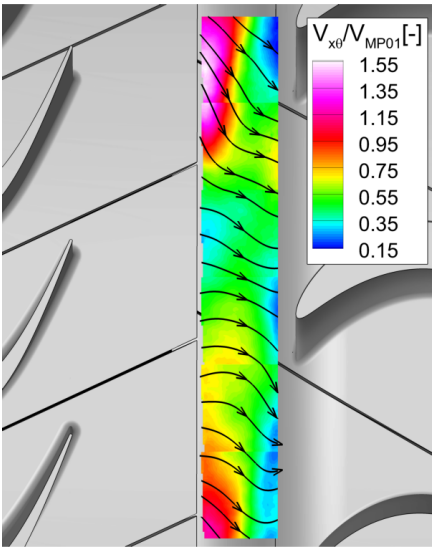

(a) *Rotor 1 reference position*

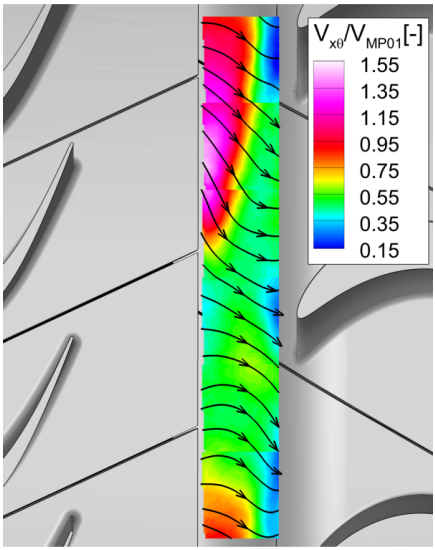

(b) *Rotor 1 turned by 1/2 rotor pitch*

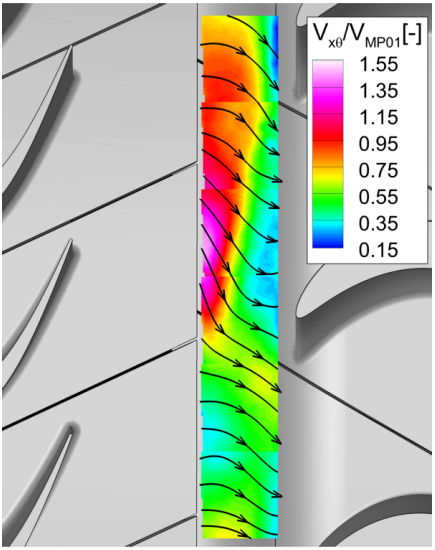

(c) *Rotor 1 turned by 1 rotor pitch*

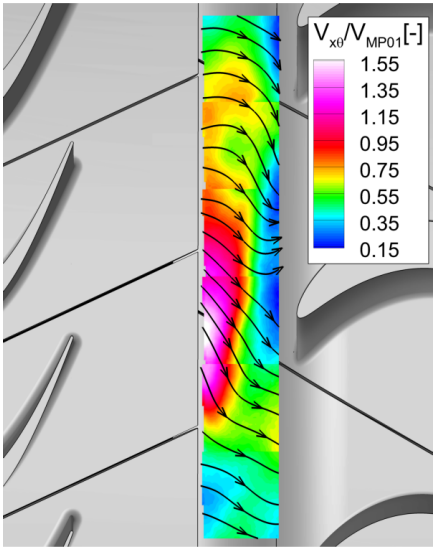

(d) *Rotor 1 turned by 1 1/2 rotor pitch*

Figure 6.34: *Velocity distribution at -2% channel height for different rotor positions*

movement of the drive arm holes, which are moved continuously downwards in Fig. 6.34. The effect of the rotor-stator position is, if at all, of minor relevance.

To examine if the different rotor-stator positions influence the development of the discrete vortex within the rim seal, Fig. 6.35 shows the development of this vortex at the four different rotor positions shown before. As in Chapter 6.1.2 the vortex is indicated qualitatively by the streamlines within the rim seal, which are derived from the radial PIV planes. Also the radial position of the vortex core is again indicated by the colour of the circles in the vortex centres.

Comparing the different rotor positions a single vortex is visible within the periodic sector for each rotor position. This vortex moves together with the drive arm hole step by step from top to the bottom of the figure. At all rotor positions the qualitative formation of the vortex is similar. The propagation of the vortex begins closely downstream of the rotor platform and moves by about one and a half stator pitches through the rim seal before it disappears respectively enters into the main flow. In addition, the vortex is located at all rotor positions radially inwards upstream of the vanes leading edge and more outwards between two vanes.

Summarising the results it is finally proved that the unperiodic structure respectively the vortex in the rim seal is indeed caused by the drive arm hole jets, as they are related to the movement of the drive arm holes. In addition, it is shown that the flow field within the rim seal is dominated at all rotor positions by the flow structure which arises from these jets. The influence of the rotor position is of minor relevance. The existence of the stator vanes, however, influences to some part the formation of the recirculation zone within the rim seal. As for IR = 0.3%, the examination of the flow field for a single rotor-stator passage in Chapter 6.1.2 seems to be an appropriate approach. Actually, it should be preferred compared to the examination of time averaged results, as the latter results would probably not show the complex flow field within the rim seal but rather a “smeared out” one.

6.4 Influence of Drive Arm Hole Diameter

A main finding from the previous sections of this thesis is that the flow field within the rim seal is significantly influenced by the existence of the drive arm hole jets. From this observation the following question arises: How do these jets influence the flow field within the main annulus and the generated losses? Furthermore, it is of interest how a changed penetration depth of the drive arm hole jets alters the results assessed within the rim seal and wheelspace. To answer these questions measurements with a different diameter of the drive arm holes have been carried

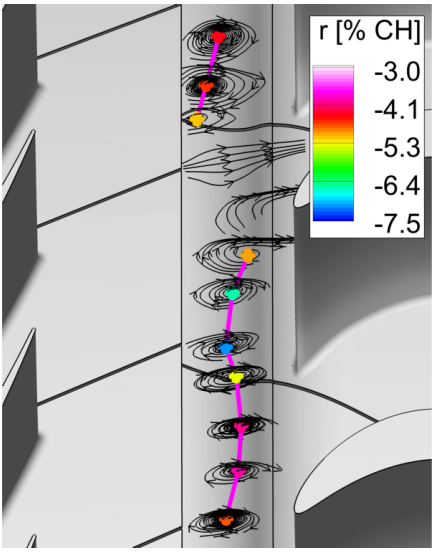

(a) *Rotor 1 reference position*

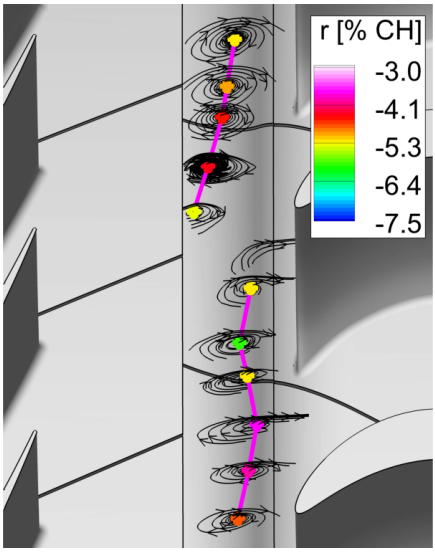

(b) *Rotor 1 turned by 1/2 rotor pitch*

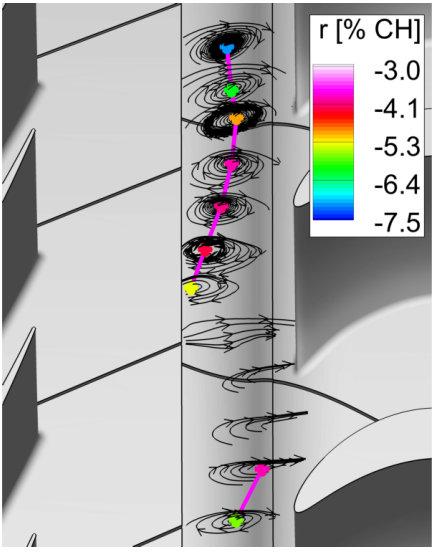

(c) *Rotor 1 turned by 1 rotor pitch*

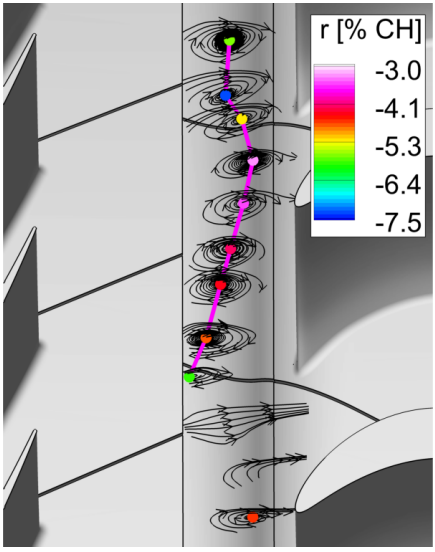

(d) *Rotor 1 turned by 1 1/2 rotor pitch*

Figure 6.35: *Flow field within the rim seal for different rotor positions*

out. As it has already been described in Chapter 4.2, these measurements have been conducted with an enlarged drive arm hole diameter of in average 11.6mm, which reduces the drive arm hole velocity ratio by approx. 40-46%. As the injection rate IR has been maintained equal to the previous values and the penetration depth of the drive arm hole jets is related to the velocity ratio, this allows to study the influence of the jets separated from the influence of a varied IR. The results from these measurements will be presented in the following in terms of the different hole diameters, whereas the larger hole represents always the lower velocity ratio.

First, the results measured at MP04 are presented. At this position a significant influence of the purge flow on the flow field within the main annulus has been examined previously. Thus, it is the most interesting measurement plane to assess the effect of the drive arm hole jets on the flow field within the main flow. Figure 6.36 shows on the left hand side the circumferentially averaged pressure loss coefficient ζ across the second stator row. The solid lines represent the results from the baseline measurements, whereas the dashed lines indicate the results from the larger drive arm holes. The purge flow rate is in both configurations indicated by the line colour. For IR = -0.28% no differences between the two configurations are visible. As there is almost no flow fed through the drive arm holes at this injection rate, this has been expected. It primarily shows that there are no changes of the flow field visible due to the rig modification itself.

Examining the data for the increased purge flow it gets clear that the losses over the second stator row are still almost unchanged. Only for IR = 1% a detectable difference is visible, featuring slightly increased losses between 10% and 30% channel height. However, comparing this difference with the one that arises between the different purge flow rates, it is small. Fig. 6.36 shows on the right hand side the yaw angle distribution at MP04 for both drive arm hole diameters. Again there is only a negligible difference visible between both configurations. The highest differences are obtained for IR = 1.0% and are within the order of 0.6 degrees. This is noticeably below the change caused by different purge flow rates and shows again that the influence of the velocity ratio is small compared to the influence of the injection rate.

To assess the effect of the different velocity ratios further, contour plots of the pressure loss coefficient ζ are shown in Fig. 6.37 for IR = 1.0% and IR = 1.5%. In contrast to the averaged losses, these plots also allow to compare the flow structure and the distribution of losses at MP04 at the different velocity ratios. In the figure iso-lines of the pressure loss coefficient are shown for both configurations. The red lines are representative of the 8.5mm holes and thus the higher velocity ratio, whereas the black lines indicate the 11.6mm diameter holes and hence the

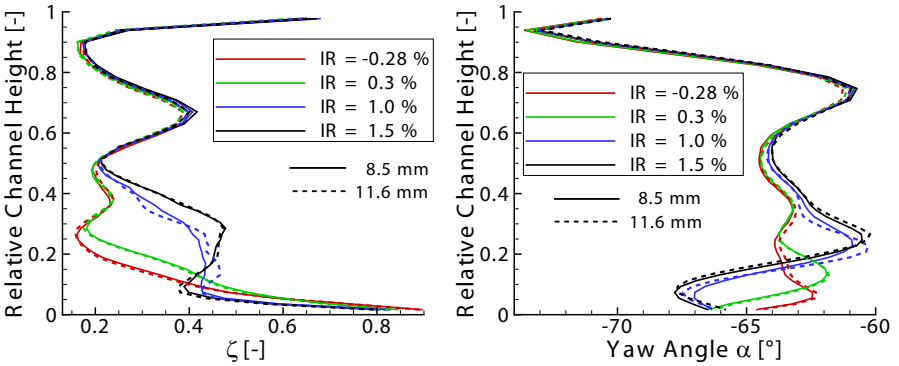

(a) Pressure loss coefficient *(b) Yaw angle distribution*

Figure 6.36: *Circumferentially averaged pressure loss coefficient and yaw angle at MP04 for two different drive arm hole diameters*

lower velocity ratio. Comparing the two configurations, only slight changes are visible. For the injection rate of 1.0% there is a slight increase of the peak pressure loss examined. However, the more important observation is that the general flow structure and distribution of losses has not been changed. For IR = 1.5% the differences are even less, showing an almost identical distribution of the losses.

Besides the distribution of losses within the passage, also the distribution of secondary flows is an indicator whether the drive arm hole jets have an influence on the interaction between the rim seal and main annulus flow. To examine this, Fig. 6.38 shows the secondary flow structures at both configurations. As for the pressure loss there are only small differences visible. These small differences do not change the general structure of secondary flows and are much smaller compared to the changes between different purge flow rates.

Nevertheless, also the propagation of the purge flow through the stator passage is of interest and depends probably on the velocity ratio of the drive arm hole jets. To investigate this, Fig. 6.39 presents the CO_2 concentration at MP04 for IR = 1.0% and IR = 1.5% for the two drive arm hole configurations. Again iso-lines of constant concentration are shown for both configurations. As for the flow field, also the propagation of the purge flow within the main flow is similar at the different velocity ratios. Only some small differences are visible, featuring an increased concentration for the baseline configuration. However, these changes are within

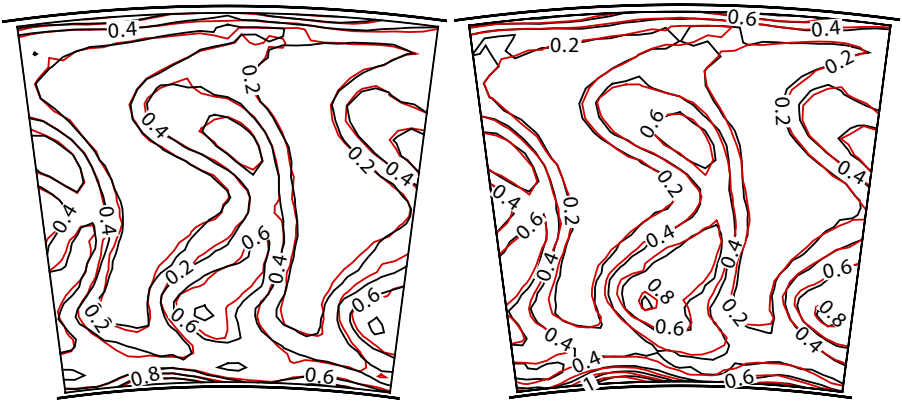

(a) Pressure loss coefficient for IR = 1.0% *(b) Pressure loss coefficient for IR = 1.5%*

Figure 6.37: *Comparison of the pressure loss coefficient across the second stator row for different drive arm hole diameters*

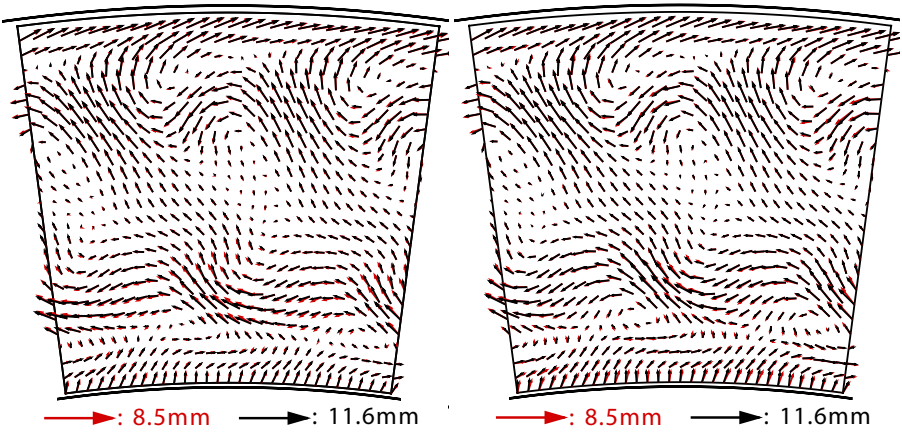

(a) Vector field for IR = 1.0% *(b) Vector field for IR = 1.5%*

Figure 6.38: *Comparison of secondary flow structures for different drive arm hole diameters at MP04*

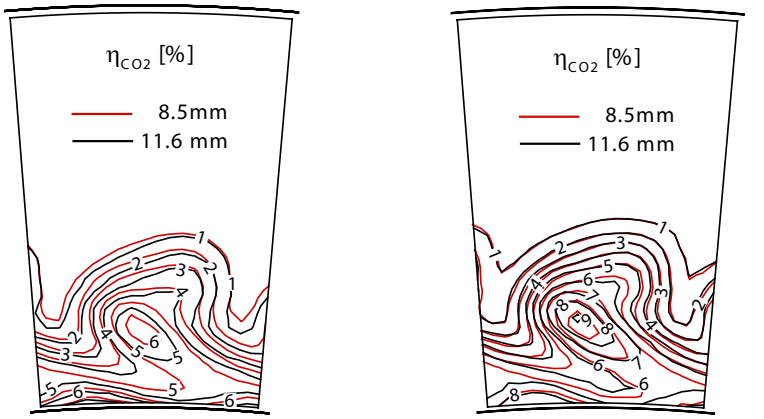

(a) *CO_2 concentration for IR = 1.0%* ***(b)*** *CO_2 concentration for IR = 1.5%*

Figure 6.39: *Propagation of purge flow within the main annulus for different drive arm hole diameters*

the measurement uncertainty and do not change the general structure of the CO_2 distribution. The regions of the highest CO_2 concentration are for both cases at the same location, showing that the propagation of the purge flow through the main annulus is probably almost unchanged.

Summarising it can be stated that only a minor influence of the tested velocity ratios is observed downstream of the vane row from the conducted measurements. This indicates that the development of the secondary flows as well as the propagation of the purge flow is rather unaffected by the drive arm hole jets and thus probably also by the vortex in the rim seal. However, it should be pointed out at this point of the investigation that the 5-hole-probe and the CO_2 data only yield time averaged results. Any instationary or phase-locked effect, which are potentially caused by the drive arm hole jets, will not be detected from these measurements. As shown by Linker [55], such phase locked effects occur at the baseline configuration (see Chapter 2.3). Thus, it is suggested by the author of this thesis to perform additional instationary or phase locked measurements using hot wire anemometry or PIV. This might yield a more profound insight into the effects that are caused by the drive arm hole jets in the main annulus. However, these measurements have not been performed during the measurement campaign of this thesis.

In the next step the results from the measurements within the rim seal and the wheelspace are examined for the different velocity ratios. This shall answer the following question: How is the flow field and the hot gas ingestion influenced by the velocity ratio of the drive arm hole jets in this area? For this purpose, Fig. 6.40 shows the sealing effectiveness in the R1S2 cavity for both configurations. The red line indicates the sealing effectiveness measured at point **A** and **B** for the baseline configuration whereas the black line represents the sealing effectiveness for the increased drive arm hole diameter. For the latter configuration only the four highest purge flow rates could have been measured. Observing the results, a significant difference is detected. For the reduced velocity ratios the sealing effectiveness rises to values of 100% at a purge flow rate of 0.75%. This is 7% above the value obtained for the baseline configuration. In addition, it reveals that a fully sealed wheelspace can be obtained with this configuration. Nevertheless, if the purge flow rate is increased to values exceeding 0.75%, the sealing effectiveness decreases similarly to the baseline configuration but at elevated values. Overall, this shows that the sealing effectiveness in the rim seal is supposed to be influenced by the drive arm hole jets (for more details see Chapter 6.5)

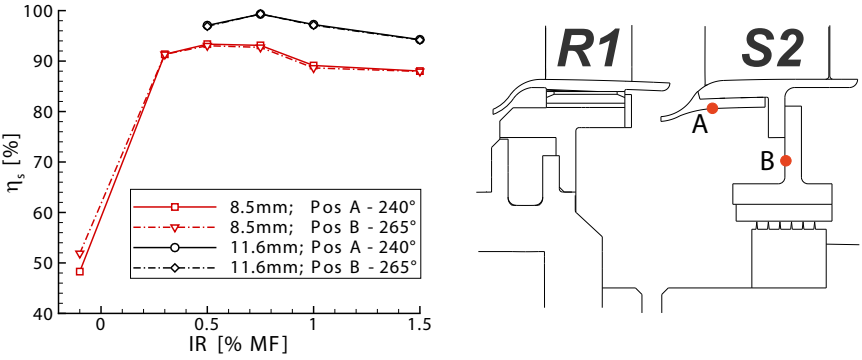

***(a)** Sealing Effectiveness* ***(b)** Measurement Location*

***Figure 6.40:** Sealing effectiveness of the R1S2 wheelspace for different drive arm hole diameters*

In addition to the sealing effectiveness, also the flow field within the rim seal might be influenced by the drive arm hole jets. To examine this Fig. 6.41 shows on the left hand side the platform pressure distribution 4% C_x upstream of the stator leading edge. The solid lines are representative of the baseline drive arm holes, whereas

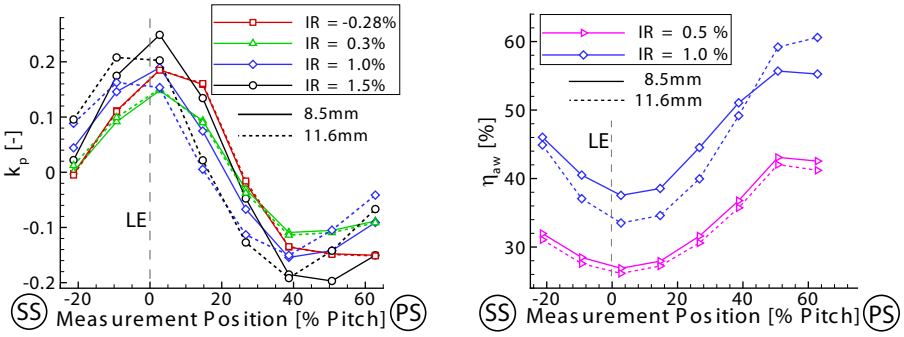

(a) *Pressure distribution 4% C_x upstream LE* ***(b)*** *Cooling effectiveness 4% C_x upstream LE*

Figure 6.41: *Pressure distribution and cooling effectiveness at the stator platform for two different drive arm hole diameters*

the dashed lines are representative of the 11.6mm diameter holes. Observing the platform pressure distribution, there are almost no differences visible between the two configurations for an injection rate of up to 0.3%. At the two highest purge flow rates, however, there is a difference detectable. For IR = 1.0% and IR = 1.5% the curves are shifted towards the suction side of the vane by approximately 5-10% of the stator pitch. From this it is supposed that the stagnation point is shifted towards the suction side and hence the negative incidence is increased. A reason is possibly that the drive arm hole induced vortex within the rim seal is less pronounced at the reduced velocity ratio. As it has been shown in Chapter 6.1.2, this vortex is filled with purge flow which owns a reduced tangential velocity. Thus, fluid with reduced tangential velocity is distributed inhomogeneously within the rim seal and affects only the area where the vortex is present. Now if the purge flow filled vortex is weakened, the purge flow enters probably more homogeneously into the rim seal and thus affects probably a larger area within the rim seal. This in turn leads probably to the increased negative incidence which has been deduced from the time averaged wall pressure measurements. Additional PIV measurements would be required within the rim seal to further assess this effect.

On the right hand side of Fig. 6.41 the adiabatic cooling effectiveness is presented for IR = 0.5% and IR = 1% at the same location where the pressure distribution has been examined before. For the lower of the two purge flow rates there is only a small difference visible between both configurations which is within the measurement uncertainty. However, for IR = 1% the second configuration shows

a larger variation of the cooling effectiveness in circumferential direction. This may again be explained by a weakening of the purge flow filled vortex in the rim seal. The development of this purge flow filled vortex prevents the formation of the typical flow field in the rim seal which features increased inflow upstream of the vane's leading edge and increased outflow within the passage. Furthermore, the vortex smears out this typical distribution of the purge flow, since it rotates together with the rotor in circumferential direction. Now, if this vortex is weakened its influence is less pronounced and the flow field will tend to its typical behaviour with an increased influence of the vanes leading edge. This results in an increased variation of the cooling effectiveness in circumferential direction, as observed by the measurements shown in Fig. 6.41 b.

After the influence of the altered velocity ratio on the flow field within the main annulus and the rim seal has been assessed, the influence on the turbine efficiency is investigated in the last step. This allows to assess the global impact of the velocity ratio. For this purpose, Fig. 6.42 shows the results from efficiency measurements for both drive arm hole diameters, whereas the efficiency is presented relative to the case of the lowest purge flow. All in all, a stronger efficiency decrease is revealed for the larger drive arm hole diameter at all purge flow rates. At IR = 1.5% the efficiency drop increases by almost 0.2%.

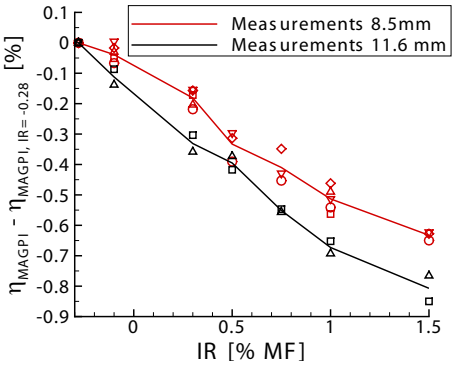

Figure 6.42: *Efficiency measurements for two different drive arm hole diameters*

This result is somehow contradictory to the results presented above, which reveal the losses and the flow field across the stator passage to be almost unchanged. This makes an explanation of the results quite delicate. A possible reason for the increased losses could be the increased negative incidence at the stator vane,

which is supposed to arise from the lowered velocity ratio. However, this is just an assumption which can not be further fortified since the additional losses that might arise from this increased incidence are not visible downstream of the vane row. Another reason for the changed efficiency result could be a modification of the instationary effects in the main flow, which have been shown by Linker [55] and are related to be drive arm hole jets. However, since these instationary effects have not been studied experimentally for the decreased velocity ratio, an investigation of these effects is not possible. Due to this lack of experimental data it was attempted to gather some reasons for the increased efficiency drop by the use of CFD calculations[5]. However, these simulations do not predict the tendency of an increased efficiency drop at the holes with a larger diameter, but rather show an reduced efficiency sensitivity.

Overall, further investigations seem to be necessary to reveal the reason for the increased efficiency drop. As long as there is no reliable explanation of these results available, these should be handled with care from the author's point of view.

Nevertheless, a confirmation of these results would not necessarily mean that the configuration with the lowered velocity ratio is inferior in comparison to the baseline configuration. As this configuration offers a better sealing of the wheelspace, less coolant flow would be needed. This in turn might overcompensate the increased efficiency drop since less coolant flow leads to a reduced efficiency deficit. In addition, the thermodynamic cycle of the engine is less affected if there is less purge flow required. Furthermore, a fully sealed rim seal could be achieved

However, if some amount of hot gas ingestion can be tolerated, the configuration with the increased velocity ratio might be beneficial since it offers a reduced efficiency decrease. Yet, this is not always possible since the pressure difference across the drive arm holes is in general limited by the pressure the coolant flow is supplied with. This available pressure depends primarily on the position respectively stage where the compressor offtake is located and depends on the general architecture of the engine. Especially in the first stage of a low pressure turbine the available pressure might not allow to provide the comparably high velocity ratios. However, towards the rear stages the pressure difference across the drive arm holes increases since the main annulus pressure is continuously reduced.

[5] Carried out by Mr. Schmid at the Institute of Gas Turbines and Aerospace Propulsion at TU Darmstadt (see Chapter 3.4)

6.5 Reasons for the Decrease of the R1-S2 Sealing Effectiveness

In Chapter 6.1.3 a decreasing sealing efficiency in the R1-S2 wheelspace has been examined for the baseline drive arm hole configuration if the purge flow rate is increased above a level of 0.75%. Even though this decrease is not very significant, it was not expected prior to the measurements. To assess the possible reason for this decrease in sealing effectiveness, additional results are presented and discussed in this chapter.

In Chapter 6.4 it has already been revealed that the sealing effectiveness depends not only on the purge flow rate but also on the velocity ratio of the drive arm hole jets. Thus, it is assumed that the influence of the drive arm hole jets is the main contributor to the decreasing sealing effectiveness.

To study the effect of the drive arm hole jets in more detail it is beneficial to gather informations of the flow field not only within the rim seal but also in the wheelspace. However this is not possible with the current measurement system. For this reason a numerical simulation of the current geometry has been performed by Schmid et al. [95] to get a better insight into the flow field within the wheelspace. Figure 6.43 shows on the left hand side the radial velocity V_r gathered from this simulation at a circumferential plane of constant radius, which is located upstream of the stator platform's leading edge (see right hand side in Fig. 6.43). A fixed rotor-stator relative position is presented in this figure over a drive arm hole periodic sector, whereas the border between inflow and outflow is marked by the black lines.

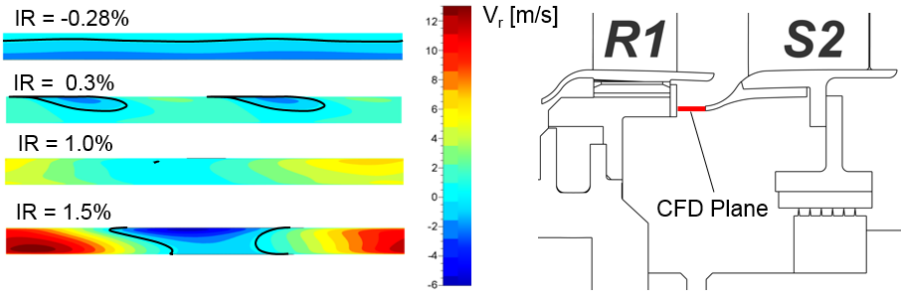

Figure 6.43: Radial velocity upstream of the stator platform's leadings edge; adapted from Schmid et al. [95]

Examining the results, there is a uniform zone of inflow and outflow visible for the lowest purge flow rate. If the purge flow rate is increased to the engine

representative rate of 0.3% the area of ingress is strongly reduced and two separated zones of inflow become visible. These zones of ingress can geometrically be related to the leading edges of the vanes and are most probably caused by their potential field. At IR = 1.0% there is almost no ingress visible anymore, leading to a high sealing effectiveness. In addition the influence of the stator vanes disapears and a structure develops which is periodic with the drive arm holes. This behaviour is even more pronounced at IR = 1.5% and shows that the influence of the drive arm hole jets is clearly present in the examined region. However, at this IR also a distinct zone of negative radial velocity develops between the zones of increased radial outflow, which is assumed to be driven by the existence of the drive arm hole jets. It probably feeds hot gases, which are present in the rim seal, into the wheelspace and therefore leads to a reduced sealing effectiveness. Thus, this zone of negative radial velocity seems to be at least one reason for the decrease in sealing effectiveness. This hypothesis is supported by the fact that this zone is connected with the main flow by a thin region of negative axial velocity V_x at the surface of the stator platform.

Another possible reason for the increased ingestion of main annulus fluid can be derived from the experimental data. According to a review from Johnson et al. [42] also the turbulent transport mechanisms play a role in the ingestion process. Therefore, the RMS value obtained from the PIV measurements is investigated in this section. This value is representative of the average fluctuation of the instantaneous results around their averaged value. Figure 6.44 shows this mean fluctuation of the velocity in radial direction V_r' at four different pitch-wise positions for IR = 1.5%. These positions are chosen to be at representative locations of the purge flow filled vortex within the rim seal. In general, it is observed that the fluctuation in radial direction is significantly increased in the area where the formation of this vortex begins. Along the length of the vortex the RMS values decrease contiuously until the vortex disappears and probably enters into the main flow, whereas at this position there are again some slightly increased fluctuations visible.

In contrast to the results obtained at the highest injection rate, Fig. 6.45 shows the RMS value for IR = 0.3% at the same pitch-wise locations. In general, the fluctuations in radial direction are significantly reduced at this purge flow rate. In addition, these are almost uniformly distributed in circumferential direction and the peak fluctuations are visible at all pitch wise positions in the region where the most distinct inflow of fluid has been observed previously (see e.g. Fig. 6.14). This shows that the high fluctuations in the rim seal at IR = 1.5% are probably caused by the formation of the drive arm hole induced vortex in the rim seal. These increased fluctuations may lead to instantaneous flow constellations in which main

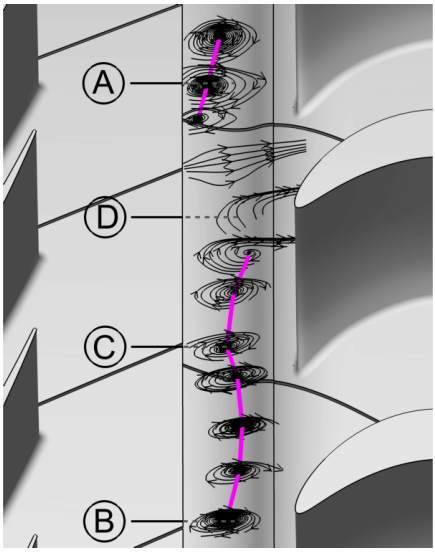

(a) Position of radial planes

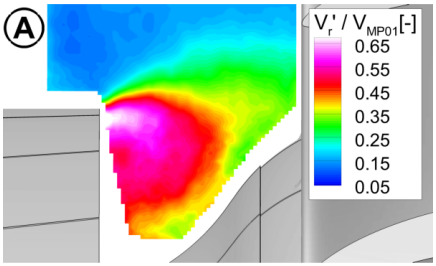

(b) −1 pitch (at LE upper vane)

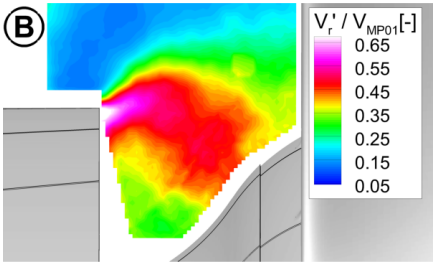

(c) +0.2/3 pitch

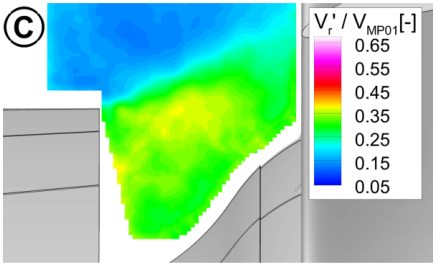

(d) 0 pitch (at LE middle vane)

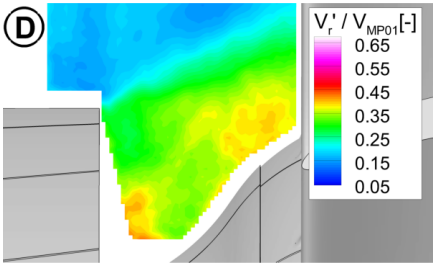

(e) −1/2 pitch

Figure 6.44: *Fluctuation of velocity in radial direction; IR = 1.5%*

annulus fluid is drawn into the rim seal. For this reason, the increased fluctuation of the flow is assumed to be at least another possible reason for the decreasing sealing effectiveness. Possibly this source of hot gas ingestion is supported by the regions of negative radial velocity, which have been examined above with the help of CFD calculations, by the following mechanism: Caused by the high fluctuations,

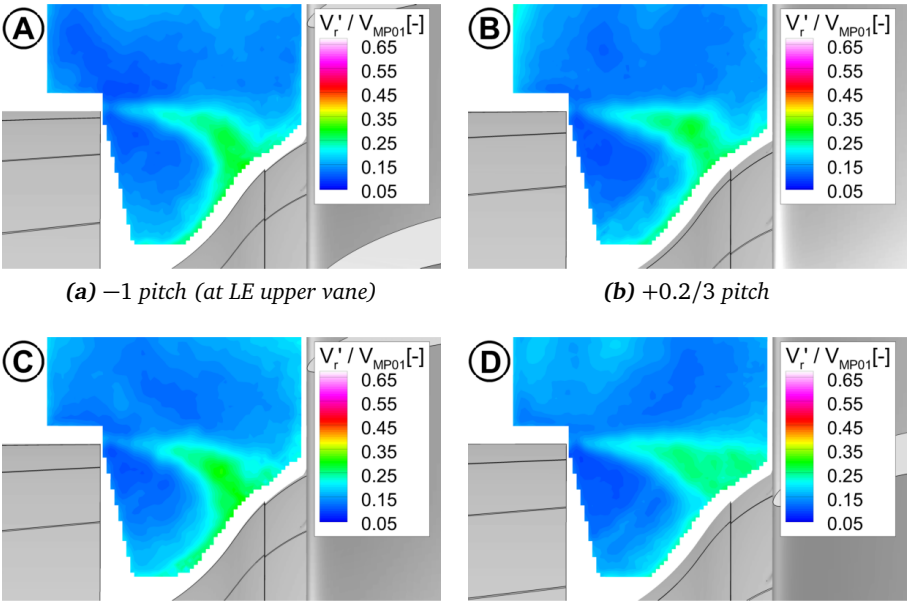

(a) -1 *pitch (at LE upper vane)* ***(b)*** $+0.2/3$ *pitch*

(c) 0 *pitch (at LE middle vane)* ***(d)*** $-1/2$ *pitch*

Figure 6.45: *Fluctuation of velocity in radial direction; IR = 0.3%*

instantaneous flow constellations occur which transport some proportion of the main annulus fluid into the rim seal. There it is afterwards transferred further into the wheelspace by the regions of negative radial velocity which are present upstream of the stator's platform leading edge.
In general, both effects are caused by the drive arm hole jets and thus confirm the influence of these jets on the sealing capability of the rim seal.

7 Summary and Suggestion of Further Research Potential

In modern gas turbines or jet engines the ingestion of hot gases into the rotor-stator wheelspace of a turbine has to be prevented to shield the rotor discs from hot temperatures. For this purpose, coolant flow is fed into the wheelspace to cool the rotor discs and purge the rim seals. This so-called purge flow has the ability to influence the development of secondary flow structures when it re-enters into the main gas path. For this reason a thorough understanding of the interaction between purge and main annulus flow is required. In addition, the driving mechanisms of hot gas ingestion and their modelling are of interest to estimate the required amount of purge flow. For this reason numerous research projects have investigated purge flow related topics. However, most of these investigations have been carried out for configurations where the purge flow enters upstream of a rotor row. To assess whether there is any principal difference between the purge flow injection upstream of a rotor row and upstream of a stator row, this thesis presents results from a configuration where the purge flow enters upstream of a stator row. In addition, the following question arises: How does the delivery of purge flow through discrete drive arm holes, which is often the case in low pressure turbines, influence the interaction between purge and main annulus flow?

To answer these questions and to broaden the general understanding of the interaction between purge and main annulus flow, extensive experiments have been carried out during the EU Project MAGPI at the LSTR, an upscaled two stage low Mach number turbine. Applying several different measurement techniques, these experiments reveal on the one hand the impact of the purge flow on the flow field within the rim seal and main annulus. On the other hand, the experiments allow the tracking of the purge flow through the stator passage and to assess the adiabatic cooling effectiveness at the stator surface. Furthermore, the sealing effectiveness in the wheelspace and the turbine efficiency are determined. Altogether, these diverse results provide a comprehensive picture of the interaction between purge and main annulus flow and the underlying mechanisms.

The results from the experiments yield an efficiency drop of about 0.6% for the baseline drive arm hole configuration if the injection rate is increased from its

lowest value of -0.28% to the highest value of 1.5%. To assess the reason for this efficiency decrease in more detail, results from the aerodynamic measurements have been examined and yield the following five possible loss sources.

- A blockage in the main flow leading to a redistribution of the flow already upstream of the purge flow injection.
- Increased secondary flows across the stator vane caused by an increased negative incidence at the vanes leading edge.
- Increased mixing losses at elevated purge flow rates.
- Changed inflow conditions at the subsequent rotor row.
- Potentially increased profile losses.

Overall, these results are similar to the ones examined at configurations where the purge flow enters upstream of a rotor row. Thus, one main outcome from the measurements is that the influence of the purge flow injection is in general similar upstream of a rotor row and upstream of a stator row.

However, even though the main conclusions are the same, some differences have been examined. These are gained primarily from highly resolved flow field measurements within the rim seal, which have been carried out by the help of an endoscopic PIV system. These measurements are unique to the knowledge of the author and in the first instance provide the opportunity to examine the flow field within the rim seal in such a detail.
For instance, it is shown by these measurements that the driving mechanism for the development of the negative incidence is different in comparison to configurations where the purge flow enters upstream of the first rotor row in the HPT. This is primarily caused by the delivery of the purge flow through the discrete drive arm holes. Since these are located in the rotational frame of reference, the purge flow enters into the wheelspace with a tangential velocity in rotor rotational direction. This in turn leads to an increased swirl and hence tangential velocity within the wheelspace at elevated purge flow rates. As it has been shown by results from PIV, this increased tangential velocity in rotor rotational direction causes the strong negative incidence. This is contrary to the situation upstream of a rotor vane, where the negative incidence is caused by a reduced tangential velocity rather than by an increased tangential velocity in the wheelspace. Thus, the preswirled delivery of purge flow, which is according to the literature beneficially upstream of a rotor row, has rather detrimental effects upstream of a stator row. Therefore, this should be avoided.

In addition to the altered development of the incidence situation, a significant influence of the drive arm hole jets has been examined with the help of PIV. It is shown that the flow field within the rim seal is dominantly influenced by the potential field of the stator vanes at low purge flow rates, whereas at the highest purge flow rate a structure is observed within the rim seal which is neither rotor nor stator periodic. This structure is made up of a purge flow filled vortex and appears once per drive arm hole. This discrete vortex suppresses the typical flow structure within the rim seal, which originally has been made up of regions of increased ingress at the leading edge of the vane and regions of more pronounced outflow between the vanes. Instead the regions of in- and outflow are primarily related to the position of the discrete vortex. As this is shifted together with the rotor, it leads to a rather smeared out distribution of the purge flow on the stator platform if time averaged values are assessed.

In conjunction with the development of the discrete vortices in the rim seal, a decrease of the sealing effectiveness in the rotor-stator wheelspace is observed at the highest purge flow rates. This unexpected result reveals that the use of additional purge flow does not necessarily yield an improved sealing of the wheelspace. The behaviour can probably be explained by intensified fluctuations of the flow field in the rim seal. Furthermore, distinct regions of negative radial velocity have been identified upstream of the stator platform leading edge which additionally support the ingestion of main flow and are caused by the drive arm hole jets at a sufficient high purge flow rate.

Overall, the drive arm hole jets are identified to have a significant influence on the flow field within the rim seal and wheelspace in the actual configuration. For this reason their effects on the main annulus and rim seal flow have been studied in more detail by additional measurements with an enlarged drive arm hole diameter. These measurements allow to study the influence of the velocity ratio between the drive arm hole jet and the wheelspace flow and thus the jets' penetration depth independent from the purge flow rate. From these measurements only a small influence of the velocity ratio on the flow field and the propagation of the purge flow within the main annulus is detected. This is minor compared to the influence of a varied purge flow rate. However, only time averaged measurements have been carried out and it is expected that a more pronounced influence is visible if results from instationary or phase locked measurements are assessed. In contrast to the main annulus, there is a more significant influence of the velocity ratio visible in the rim seal and the wheelspace. In this region, the reduced velocity ratio leads on the one hand to a more inhomogeneous distribution of the adiabatic cooling effectiveness at the stator platform at high purge flow rates. On the other

hand, the obtained sealing effectiveness is in general increased and a fully sealed wheelspace is achieved. This also fortifies the assumption that the decrease of sealing effectiveness at increased purge flow rates is indeed caused by the drive arm hole jets. In addition, a stronger sensitivity of the turbine efficiency with respect to the purge flow injection rate has been measured for the lowered velocity ratio. However, it is not fully clear where this increased sensitivity results from. Additional investigations are suggested to examine this in more detail.

Altogether the gained results may help engineers to broaden their understanding of the purge flow related mechanisms in axial turbines. On the one hand, the extensive measurements allow to examine the flow field in many areas where only restricted measurements are available in the literature; thus, they are beneficial to get a better understanding of the purge flow related mechanisms in axial turbines. On the other hand, the potential effect of the drive arm hole jets and their influence on the flow field within the rim seal and the sealing of the wheelspace are valuable, especially since these effects have, to the author's knowledge, not been examined in detail in the literature so far. However, it needs to be taken into account that the drive arm hole induced effects might be different in turbine configurations where double overlapping rim seal geometries with a multiple cavity design are present. In this case the drive arm hole jets are possibly damped out before they reach the rim seal. Thus, they probably influence the rim seal flow in a lesser extent. In addition, it needs to be mentioned that the velocity ratios of the drive arm hole jets are expected to be in excess of engine representative values for the highest purge flow rates. This leads to an amplified effect of these jets, at least if the first stage of a low pressure turbine is examined. Nevertheless, the obtained results are useful during the design phase of low pressure turbines and may lead to new design proposals. This is especially the case if a wheelspace without any double overlapping rim seals is of interest, which is beneficial in comparison to double overlapping rim seal design if it comes to weight, complexity, part number and hence costs. Exemplarily, some design proposals which might contribute to a reduction of losses and an increase of the turbine efficiency and result directly from the obtained results shall be presented below and might be the subject of further research activities.

The first design proposal aims to reduce the swirl in the wheelspace and is expected to have multiple beneficial effects[1]. On the one hand, the reduced swirl is supposed to minimise mixing losses in the area where the purge flow enters into the main annulus. On the other hand, it probably decreases the negative incidence at the

[1] A variation of the purge flow swirl has also been proposed by Linker [55]. According to him, it may improve the incidence situation at the blade. However, no design proposal has been derived by Linker

stator vane, which in turn improves the aerodynamic behaviour of the vane and reduces the crossflow and hence secondary flow structures in the passage.
In order to reduce the swirl in the wheelspace, angled drive arm holes could be used which deliver the coolant flow at a certain angle into the wheelspace[2], whereas the flow direction needs to be in opposite direction of rotor rotation in the rotor relative frame of reference. This is schematically illustrated in Fig. 7.1 and shows two different design options. The drive arm hole on the left hand side is manufactured with an angle to the surface of the rotor drum which causes a tangential velocity component. The design proposal on the right hand side uses a bended tube which delivers the purge flow with a tangential component into the wheelspace. Furthermore, welded fairings on top of the holes could be used which turn the coolant flow in a more or less tangential direction to the rotor drum.

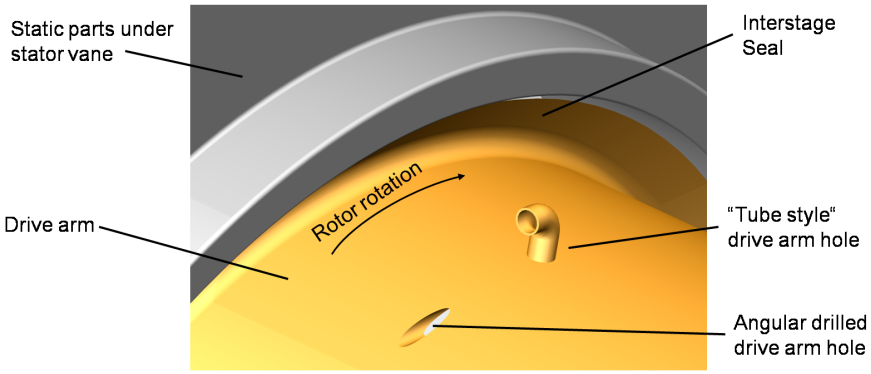

Figure 7.1: *Schematic illustration of angled drive arm holes*

As a positive side effect of this "deswirled" purge flow delivery two further benefits are predicted. On the one hand, this solution yields a longer distance between the drive arm hole's exit and the rim seal (along the jet trajectory). Thus, the effect of the drive arm hole jets is probably reduced. On the other hand, the delivery of the coolant flow through angled drive arm holes creates an additional torque around the turbine axis which will yield an increased power output and hence turbine efficiency. This effect is expected to be most pronounced if the

[2] It should be mentioned that an angling of the drive arm holes has already been studied by Andreini et al. [2]. However, the main focus of their work has been to asses the effect of these holes on the cooling effectiveness in the wheelspace. Effects on the interaction between the purge and the main flow upstream of the stator vane have not been part of this investigation.

coolant flow is fed tangentially to the rotor drum into the wheelspace. For this situation Fig. 7.2 shows exemplarily the additional torque that could be generated at the LSTR if the coolant flow is delivered into the wheelspace with the same velocity as in the non-angled case. The additional torque is presented in relation to the one at the lowest purge flow rate and thus yields the percentage increase which can theoretically be achieved. This increase is assumed to be approximately equal to the efficiency increase if all other conditions at the rig are maintained and losses due to the turning devices are neglected. It shows for the actual configurations that the additional torque may overcompensate the measured efficiency decrease due to purge flow injection and is therefore of great value. However, a part of the additional torque is probably compensated by an increased windage at the rotor discs due to increased relative velocities. In addition, the ratio between torque generated by the drive arm holes and by the turbine blades is expected to be in excess of engine representative values in the actual configuration, leading to an disproportionally rise of the shaft torque. Nevertheless, the additional torque is still a beneficial side effect of the deswirled purge flow delivery, whose main intention is the reduction of mixing losses and the negative incidence situation at the stator vane.

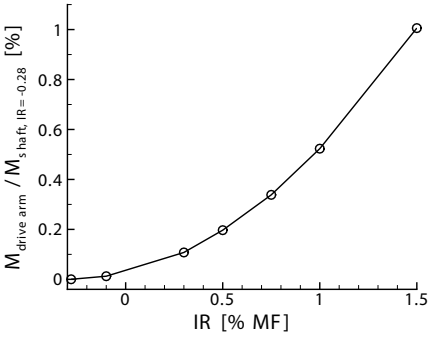

Figure 7.2: *Torque increase due to angled drive arm holes*

However, despite all these positive effects some detrimental effects can occur due to the angled drive arm hole configuration. As mentioned before, Andreini et al. [2] have examined the effect of angled drive arm holes on the adiabatic cooling effectiveness in the wheelspace by the use of numerical simulations. They show that an angled drive arm hole, which delivers the coolant fluid at an angle of 45° contrariwise to the rotor rotation leads to a reduced adiabatic cooling effectiveness at the rotor disc. Furthermore, this configuration increases the hot gas ingestion in comparison to a non-angled drive arm hole. Thus, it needs to be carefully examined if the expected aerodynamic benefits overcompensate a potentially reduced cooling of the rotor discs which might lead to an additional demand of coolant flow.

At the LSTR the angled drive arm holes could be studied by the use of inserts that turn the coolant flow into tangential direction before it exits into the wheelspace.

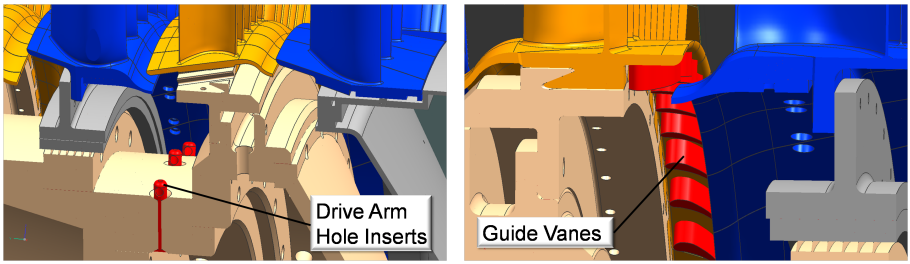

(a) Inserts with angled head *(b) Guide vanes under the rotor platform*

Figure 7.3: *Different design proposals applied at the LSTR*

Different sets of these inserts have been designed and manufactured during the preparation of this thesis, but have finally not been tested due to a limited availability of the LSTR. A schematic illustration of these inserts assembled in the drive arm holes is shown in Fig. 7.3 a, in which the main flow enters from the right hand side.

The second design proposal to reduce the detrimental effects of the purge flow injection is to apply small guide vanes under the rotor platform, as it is illustrated in Fig. 7.3 b. These guide vanes shall turn the purge flow in a way that the tangential velocity difference between the purge and the main flow is minimised. This reduces both, the mixing losses and the negative incidence that is caused by purge flow injection. Furthermore, some energy could be extracted by turning the flow in these guide vanes, which increases the torque of the rotor similarly to the angled drive arm holes. An advantage of this solution is that the swirl of the wheelspace fluid is reduced just at the point of interest, whereas the deswirled flow from the angled drive arm holes gains back some swirl from friction at the rotor disc before it enters into the rim seal. However, a disadvantage of this design is a restriction of the axial and radial movement between the rotor and the stator platforms. Since this movement needs to be taken into account during the design phase of the turbine, the guide vanes will probably lead to larger gaps between the rotor and stator platforms, promoting hot gas ingestion.
In addition to the investigation of the two presented design proposals, further measurements using the current setup of the rig are recommended by the author. These are primarily valuable to understand the effects of the drive arm hole jets in more detail and get a better insight into the interaction between purge and main annulus flow. For this it is proposed to carry out the endoscopic PIV measurements

in the rim seal for the reduced velocity ratio. This would possibly yield a further insight into the influence of the drive arm hole jets. Furthermore, instationary or phase locked measurements should be carried out downstream of the stator passage for both drive arm hole configurations. For this purpose hot wire anemometry measurements could be used as it has been done by Linker [55], but also the endoscopic PIV system used at the LSTR is adequate to assess phase locked effects. The results from these measurements are expected to provide further insight into the flow mechanisms that occur in the passage due to the existence of the vortices which are induced by the drive arm hole jets in the rim seal. Furthermore, these results might help to assess the reason for the increased efficiency sensitivity, which has been assessed for the enlarged drive arm holes.

Besides these additional measurements the gained results should be used in the future to validate numerical tools. This validation might improve the confidence in numerical simulations and allows engineers to use these models for future design optimisations. Exemplarily, parameter studies could be carried out to identify optimised geometries that reduce losses and improve the sealing effectiveness.

Even though this validation of numerical tools has been done extensively during the MAGPI project, most of the PIV results were obtained after the project end. As these results provide a detailed insight into the flow mechanisms in the rim seal, they are valuable for the further validation of numerical models. In this context, it would also be useful to correct the perspective error of the PIV measurements. This has not been done during this thesis since there was no additional knowledge acquisition expected from it. However, for a quantitative comparison with numerical results this is recommended. Furthermore, a large number of the PIV measurements at further channel heights and rotor-stator relative positions have not been post-processed so far and could be examined to have an even larger experimental data base. This additional database might in addition facilitate the correction of the perspective error.

In addition to this validation of numerical tools, the effect of a difference in temperature/density between purge and main annulus flow should be studied in future research projects. In the current work, this typical temperature/density difference of a real turbine has not been accounted for due to experimental constraints. Nevertheless, it is of interest to what extend this influences the interaction between purge flow and main annulus flow. Furthermore, results from such studies might reveal how the results of this thesis are influenced due the density difference. For this purpose the above mentioned validated numerical tools could be used as they allow a change in temperature of purge and main annulus flow quite easily.

Finally, it needs to be mentioned that the gained results are most probably only valid for subsonic turbines. Thus, one needs to be careful if the results are transferred to transonic turbine configurations where the obtained results are supposed to be influenced by trailing edge shock waves. These might have a significant influence on the flow field within the rim seal and thus the effect of the drive arm hole jets. Thus, the influence of the trailing edge shock waves on the flow field within the rim seal should be another research field in the future.

Overall, the current thesis shows several effects which are related to purge flow injection and have not been investigated or understood in detail so far. In this thesis, some of these effects like the influence of drive arm hole jets are examined and described in detail. However, while some effects are better understood now, others still need further attention.

Bibliography

[1] Airbus. Navigating the Future; Global Market Forecast 2012-2031. 2012.

[2] A. Andreini, R. Da Soghe, and B. Facchini. Turbine Stator Well CFD Studies: Effects of Coolant Supply Geometry on Cavity Sealing Performance. *Proceedings of the ASME Turbo Expo* , (GT2009-59186), 2009.

[3] J. Balasubramanian, N. Junnarkar, D. W. Zhou, R. P. Roy, Y. W. Kim, and H. K. Moon. Experiments on Aft-Disk Cavity Ingestion in a Model 1.5-Stage Axial-Flow Turbine. *Proceedings of the ASME Turbo Expo* , (GT2011-45895), 2011.

[4] F. J. Bayley and J. M. Owen. The Fluid Dynamics of a Shrouded Disk System With a Radial Outflow of Coolant. *ASME Journal of Engineering for Power*, pages 335–341, 1970.

[5] D. E. Bohn, A. Decker, H. Ma, and M. Wolf. Influence of Sealing Air Mass Flow on the Velocity Distribution in and inside the Rim Seal of the Upstream Cavity of a 1.5-Stage-Turbine. *Proceedings of the ASME Turbo Expo*, (GT2003-38459), 2003.

[6] D. E. Bohn and M. Wolf. Improved Formulation to Determine Minimum Sealing Flow for Different Sealing Configurations. *Proceedings of the ASME Turbo Expo*, (GT2003-38465), 2003.

[7] J. Boudet, N. J. Hills, and J. W. Chew. Numerical Simulation of the Flow Interaction between Turbine Main Annulus and Disc Cavities. *Proceedings of the ASME Turbo Expo*, (GT2006-90307), 2006.

[8] G. Boutet-Blais, J. Lefrancois, G. Dumas, S. Julien, R. Marini, J.-F. Caron, and J.-F. Harvey. Passive Tracer Validity for Cooling Effectiveness Through Flow Computation in a Turbine Rim Seal Environment. *Proceedings of the ASME Turbo Expo*, (GT2011-45654), 2011.

[9] W. J. G. Brauenling. *Flugzeugtriebwerke*. Springer, 2009.

[10] C. Bricaud, T. Geis, K. Dullenkopf, and H.-J. Bauer. Measurement and Analysis of Aerodynamic and Thermodynamic Losses in Pre-Swirl System Arrangements. *Proceedings of the ASME Turbo Expo*, (GT2007-27191), 2007.

[11] R. S. Bunker, G. M. Laskowski, J. C. Bailey, P. Palafox, G. M. Itzel, S. Kapetanovic, M. A. Sullivan, and T. R. Farrel. An Investigation of Turbine Wheelspace Cooling Flow Interactions With a Transonic Hot Gas Path - Part1: Experimental Measurements. *ASME Journal of Turbomachinery*, Vol. 133:021015–1–8, 2011.

[12] C. Cao, J. W. Chew, P. R. Millington, and S. I. Hogg. Interaction of Rim Seal and Annulus Flows in an Axial Flow Turbine. *ASME Journal of Engineering for Power*, 2004.

[13] J. W. Chew, S. Dakah, and A. B. Turner. Rim Sealing of Rotor-Stator Wheelspaces in the Absence of External Flow. *ASME Journal of Turbomachinery*, Vol. 114:433–438, 1992.

[14] M. Chilla, H. Hodson, and D. Newman. Unsteady Interaction between Annulus and Turbine Rim Seal Flows. *Proceedings of the ASME Turbo Expo*, (GT2012-69089), 2012.

[15] N. A. Cumpsty and J. H. Horlock. Averaging Nonuniform Flow for a Purpose. *ASME Journal of Turbomachinery*, Vol. 128:120–129, 2006.

[16] S. Dadkhah, A. B. Turner, and J. W. Chew. Performance of Radial Clearance Rim Seals in Upstream and Downstresam Rotor-Stator Wheelspaces. *ASME Journal of Turbomachinery*, Vol. 114:439–445, 1992.

[17] W. A. Daniels, B. V. Johnson, D. J. Graber, and R. J. Martin. Rim Seal Experiments and Analysis for Turbine Applications. *ASME Journal of Turbomachinery*, Vol. 114:426–432, 1992.

[18] R. Denos and G. Paniagua. Influence of the Hub Endwall Cavity Flow on the Time-Averaged and Time-Resolved Aero-Thermodynamics of an Axial HP Turbine Stage. *Proceedings of the ASME Turbo Expo*, (GT2002-30185), 2002.

[19] J. D. Denton. Loss Mechanisms in Turbomachines. *ASME Journal of Turbomachinery*, Vol. 115:621–656, 1993.

[20] J. Dixon, A. Valencia, D. Coren, D. Eastwood, and C. Long. Main Annulus Gas Path Interactions - Turbine Stator Well Heat Transfer. *Proceedings of the ASME Turbo Expo* , (GT2012-68588), 2012.

[21] E. R. G. Eckert. Analogies to Heat Transfer Processes. *AGARD Dograph No 130; Measurement Techniques in Heat Transfer*, (AGARD Report CP-534), 1970.

[22] R. D. Erickson and T. W. Simon. Effects of Stator/Rotor Leakage Flow and Axisymmetric Contouring on Endwall Adiabatic Effectiveness and Aerodynamic Loss. *Int. Symp. on Heat Transfer in Gas Turbine Systems, Antalya, Turkey*, 2009.

[23] R. D. Erickson, T. W. Simon, L. Zhang, and H.-K. Moon. Experimental Investigation of Disc Cavity Leakage Flow and Hub Endwall Contouring in a Linear Rotor Cascade. *Proceedings of the ASME Turbo Expo*, (GT2011-46700), 2011.

[24] European Commission. Main Annulus Gas Path Interactions; Contract for Specific Targeted Research Project, Sixth Framework Programme ASTC-CT 2006 030874. 2006.

[25] J. M. Feiereisen, R. E. Paolillo, and J. Wagner. UTRC Turbine Rim Seal Ingestion and Platform Cooling Experiments. *36th AIAA/ASME/SAE/ASEE Joint Propulsion Conference and Exhibit*, 2000.

[26] K. D. Gallier, P. B. Lawless, and S. Fleeter. Investigation of Seal Purge Flow Effects on the Hub Flow Field in a Turbine Stage Using Particle Image Velocimetry. *36th AIAA/ASME/SAE/ASEE Joint Propulsion Conference and Exhibit*, 2000.

[27] K. D. Gallier, P. B. Lawless, and S. Fleeter. Development of the Unsteady Flow on a Turbine Platform Downstream of a Rim Seal. *Proceedings of the ASME Turbo Expo*, (GT2004-53899), 2004.

[28] T. Geis. *Strömungs und reibungsinduzierte Leistungs und Wirkungsgradverluste in komplexen Rotor-Stator Zwischenräumen*. PhD thesis, Universität Karlsruhe, 2002.

[29] O. Gentilhomme, N. J. Hills, A. B. Turner, and J. W. Chew. Measurement and Analysis of Ingestion Through a Turbine Rim Seal. *ASME Journal of Turbomachinery*, Vol. 125:505–512, 2003.

[30] J. Gier, B. Stubert, B. Brouillet, and L. de Vito. Interaction of Shroud Leakage Flow and Main Flow in a Three-Stage LP Turbine. *ASME Journal of Turbomachinery*, Vol. 127:649–658, 2005.

[31] S. Girgis, E. Vlasic, J.-P. Lavoie, and S. Moustapha. The Effect of Secondary Air Injection on the Performance of a Transonic Turbine Stage. *Proceedings of the ASME Turbo Expo*, (GT-2002-30340), 2002.

[32] T. Green and A. B. Turner. Ingestion Into the Upstream Wheelspace of an Axial Turbine Stage. *ASME Journal of Turbomachinery*, Vol. 116:327–332, 1994.

[33] D. K. Henecke and K. Wörrlein. *Flugantriebe*. FG Gasturbinen, Luft- und Raumfahrtantriebe, 2001.

[34] IATA. Internet resource from www.iata.de, visited at the 19th .Nov. (2013).

[35] IATA. 57th Edition of the World Air Transport Statistics (WATS). 2012.

[36] R. Jakoby, T. Zierer, L. de Vito, K. Lindblad, J. Larsson, D. E. Bohn, J. Funcke, and A. Decker. Numerical Simulation of the Unsteady Flow Field in an Axial Gas Turbine Rim Seal Configuration. *Proceedings of the ASME Turbo Expo*, (GT2004-53829), 2004.

[37] P. Jenny, R. S. Abhari, M. G. Rose, M. Brettschneider, and J. Gier. A Low Pressure Turbine with Profiled End Walls and Purge Flow Operating with a Pressure Side Bubble. *Proceedings of the ASME Turbo Expo*, (GT2011-46309), 2011.

[38] P. Jenny, R. S. Abhari, M. G. Rose, M. Brettschneider, J. Gier, and K. Engel. Low-Pressure Turbine End Wall Design Optimisation and Experimental Verification in the Presence of Purge Flow. *20th International Symposium on Air Breathing Engines* , (ISABE-2011-1717), 2011.

[39] J. Jeong and F. Hussain. On the identification of a vortex. *Journal of Fluid Mechanics*, Vol. 185:69–94, 1995.

[40] M. Jischa. *Konvektiver Impuls-,Wärme- und Stoffaustausch*. Vieweg Verlag., 1982.

[41] B. V. Johnson, R. Jakoby, D. E. Bohn, and D. Cunat. A Method for Estimating the Influence of Time-Dependent Vane and Blade Pressure Fields on Turbine Rim Seal Ingestion. *ASME Journal of Turbomachinery*, Vol. 131:021005–10, 2009.

[42] B. V. Johnson, G. Mack, R. Paolillo, and W. Daniels. Turbine Rim Seal Gas Path Flow Ingestion Mechanisms. *30th AIAA/ASME/SAE/ASEE Joint Propulsion Conference*, (AIAA 94-2703), 1994.

[43] B. V. Johnson, C.-Z. Wang, and R. P. Roy. A Rim Seal Orifice Model with Two Cds and Effects of Swirl in Seals. *Proceedings of the ASME Turbo Expo*, (GT2008-50650), 2008.

[44] S. Julien, J. Lefrancois, G. Dumas, G. Boutet-Blais, R. Marini, S. Lapointe, and J.-F. Caron. Simulations of Flow Ingestion and Related Structures in a Turbine Disk Cavity. *Proceedings of the ASME Turbo Expo*, (GT2010-22729), 2010.

[45] K. H. Jung. *Mehrreihige Filmkühlung an gekrümmten Oberflächen*. PhD thesis, Technische Universität Darmstadt, 2001.

[46] T. Kawai, S. Shinoki, and T. Adachi. Secondary Flow Control and Loss Reduction in a Turbine Cascade Using Endwall Fences. *JSME International Journal*, Series II, Vol. 132:375–387, 1989.

[47] R. D. Keane and R. J. Adrian. Optimization of particle image velocimeters. Part I: Double pusled systems. *Meas. Sci. Technol.*, 1:1202–1215, 1990.

[48] M. Kegalj and H.-P. Schiffer. Endoscopic PIV measurements in a low pressure turbine rig. *Exp. Fluids*, Vol. 47:689–705, 2009.

[49] M. Klingsporn. Main Annulus Gas Path Interactions; Final Publishable Project Report, Sixth Framework Programme ASTC-CT 2006 030874. 2011.

[50] M. Klingsporn. Main Annulus Gas Path Interactions in Gas Turbines. *Presentation at the Aerodays, Madrid*, 2011.

[51] J. Kurzke. Performance Modelling Methodology: Efficiency Definitions for Cooled Single and Multistage Turbine. *Proceedings of the ASME Turbo Expo*, (GT2002-30497), 2002.

[52] L. S. Langston. Secondary Flows in Axial Turbines - A Review. *Annals of the New York Academy of Siences*, 934:11–26, 2001.

[53] J. Lefrancois, G. Boutet-Blais, G. Dumas, G. B. Yepuri, J. Felix, V. Krishnamoorthy, R. Mohammed, J.-F. Caron, and R. Marini. Prediction of Rim Seal Ingestion. *20th International Symposium on Air Breathing Engines*, (ISABE-2011-1836), 2011.

[54] A. Lerch. *Untersuchungen zum Einfluss der Zyklonkühlung in einer Turbinenschaufel auf die adiabate Filmkühleffektivität*. Urn: urn:nbn:de:tuda-tuprints-30834, Technische Universität Darmstadt, 2012.

[55] M. C. Linker. *Quantifizierung von Sperrluft-Hauptstrominteraktion in einer Turbine*. Urn:nbn:de:tuda-prints-36988, Technische Universität Darmstadt, 2014.

[56] I. Mahle. Improving the Interaction between Leakage Flows and Main Flow in a Low Pressure Turbine. *Proceedings of the ASME Turbo Expo*, (GT2010-22448), 2010.

[57] R. J. Margason. Fifty Years of Jet in Cross Flow Research. *AGARD Symposium on a Jet in Cross Flow*, (AGARD Report CP-534), 1993.

[58] C. McLean, C. Camci, and B. Glezer. Mainstream Aerodynamic Effects Due to Wheelspace Coolant Injection in a High Pressure Turbine Stage: Part I - Aerodynamic Measurements in the Stationary Frame. *ASME Journal of Turbomachinery*, Vol. 123:697–703, 2001.

[59] C. McLean, C. Camci, and B. Glezer. Mainstream Aerodynamic Effects Due to Wheelspace Coolant Injection in a High Pressure Turbine Stage: Part II - Aerodynamic Measurements in the Rotational Frame. *ASME Journal of Turbomachinery*, Vol. 123:687–696, 2001.

[60] F. Montomoli, M. Massini, N.Maceli, L. Lombardi, M. D. Ercole, R. D. Prosperis, M. Cirri, and A. Ciani. Interaction of wheelspace coolant and main flow in a new aeroderivative low pressure turbine. *ASME Journal of Turbomachinery*, Vol. 123, 2010.

[61] W. Nitsche. *Strömungsmesstechnik*. Springer, 1994.

[62] Y. Okita, M. Nishiura, S. Yamawaki, and Y. Hironaka. A Novel Cooling Method for Rotor-Stator Rim CavitiesAffected by Mainstream Ingress. *ASME Journal of Engineering for Gasturbines and Power*, Vol. 127, 2005.

[63] J. H. P. Ong, R. J. Miller, and S. Uchida. The Effect of Coolant Injection on the Endwall Flow of a High Pressure Turbine. *Proceedings of the ASME Turbo Expo*, (GT2006-91060), 2006.

[64] J. Owen. Prediction of Ingestion Through Turbine Rim Seals - Part I: Rotationally Induced Ingress. *ASME Journal of Turbomachinery*, Vol. 133, 2011.

[65] J. Owen. Prediction of Ingestion Through Turbine Rim Seals - Part2: Externally Induced and Combined Ingress. *ASME Journal of Turbomachinery*, Vol. 133, 2011.

[66] J. Owen and R. Rogers. *Flow and Heat Transfer in Rotating-Disc Systems: Volume 1 - Rotor-Stator Systems*. Research Studies Press, 1989.

[67] J. M. Owen, O. Pountney, and G. Lock. Prediction of Ingress Through Turbine Rim Seals - Part II: Combined Ingress. *ASME Journal of Turbomachinery*, Vol. 134, 2012.

[68] J. M. Owen, K. Zhou, O. Pountney, M. Wilson, and G. Lock. Prediction of Ingress Through Turbine Rim Seals - Part I: Externally Induced Ingress. *ASME Journal of Turbomachinery*, Vol. 134, 2012.

[69] G. Paniagua, R. Denos, and S. Almeida. Effect of the Hub Endwall Cavity Flow on the Flow-Field of a Transonic High-Pressure Turbine. *ASME Journal of Turbomachinery*, Vol. 126:578–586, 2004.

[70] M. Pau and G. Paniagua. Investigation of the Flow Field on a Transonic Turbine Nozzle Guide Vane With Rim Seal Cavity Flow Ejection. *ASME Journal of Fluids Engineering*, Vol. 132:111101–9, 2010.

[71] M. Pau, G. Paniagua, D. Delhaye, A. de la Loma, and P. Ginibre. Aerothermal Impact of Stator-Rim Purge Flow and Rotor-Platform Film Cooling on a Transonic Turbine Stage. *ASME Journal of Turbomachinery*, Vol. 132:021006–12, 2010.

[72] D. R. Pedersen. *Effect of Density Ratio on Film Cooling Effectiveness for Injection Through a Row of Holes and for a Porous Slot*. PhD thesis, University of Minnesota, 1972.

[73] A. Perdichizzi and V. Dossena. Incidence Angle and Pitch-Chord Effects on Secondary Flows Downstream of a Turbine Cascade. *ASME Journal of Turbomachinery*, Vol. 115:383–391, 1993.

[74] U. P. Phadke and J. M. Owen. An Investigation of Ingress for an "Air-Cooled" Shrouded Rotating Disk System With Radial-Clearance Seals. *ASME Journal of Engineering for Power*, Vol. 105:178–182, 1983.

[75] U. P. Phadke and J. M. Owen. Aerodynamic aspects of the sealing of gas-turbine rotor stator systems - Part 1: The behavior of simple shrouded rotating-disk systems in a quiescent environment . *Int. J. Heat and Fliud Flow*, Vol. 9:98–105, 1988.

[76] U. P. Phadke and J. M. Owen. Aerodynamic aspects of the sealing of gas-turbine rotor stator systems - Part 2: The performance of simple seals in a quasi axisymmetric external flow. *Int. J. Heat and Fliud Flow*, Vol. 9:103–117, 1988.

[77] U. P. Phadke and J. M. Owen. Aerodynamic aspects of the sealing of gas-turbine rotor stator systems - Part 3: The effect of nonaxisymmetric external flow on seal performance. *Int. J. Heat and Fliud Flow*, Vol. 9:106–112, 1988.

[78] I. Popovic and H. Hodson. Aerothermal Impact of the Interaction Between Hub Leakage and Mainstream Flow in Highly-Loaded HP Turbine Blades. *Proceedings of the ASME Turbo Expo*, (GT2010-22311), 2010.

[79] I. Popovic and H. Hodson. The Effect of a Parametric Variation of the Rim Seal Geometry on the Interaction between Hub Leakage and Mainstream Flows in HP Turbines. *Proceedings of the ASME Turbo Expo*, (GT2012-68025), 2012.

[80] I. Popovic and H. Hodson. Improving Turbine Stage Efficiency and Sealing Effectiveness through Modifications of the Rim Seal Geometry. *Proceedings of the ASME Turbo Expo*, (GT2012-68026), 2012.

[81] J. Pueblas, R. Corral, and S. Schrewe. Interaction of Rim Seal and Main Annulus Flow in a Low-Speed Turbine Rig. *Proceedings of the ASME Turbo Expo*, (GT2013-94109), 2013.

[82] S. Pyliouras. *Auswirkungen der Magerverbrennung auf die Turbinenaerodynamik*. PhD thesis, Technische Universität Darmstadt, 2011.

[83] M. Rabs, F.-K. Benra, H. J. Dohmen, and O. Schneider. Investigation of Flow Instabilities near the Rim Cavity of a 1.5 Stage Gas Turbine. *Proceedings of the ASME Turbo Expo*, (GT2011-59965), 2009.

[84] M. Rabs, F.-K. Benra, C. Domnick, and O. Schneider. Computational Study of Kelvin-Helmholtz Instabilities Created by Interaction of the Mainstream Flow and the Seal Flow in Gas Turbine. *Proceedings of the ASME Turbo Expo*, (GT2011-45284), 2011.

[85] M. Rabs, F.-K. Benra, and O. Schneider. Emergence of Kelvin-Helmholtz Instabilities in Gas Turbine Rim Cavities - A Parameter Study. *Proceedings of the ASME Turbo Expo*, (GT2012-68834), 2012.

[86] M. Raffel, C. WIllert, S. Werely, and J. Kompenhans. *Particle Image Velocimetry: A Practical Guide*. Springer, 2007.

[87] C. Rakenius, G. Schmid, and H.-P. Schiffer. The Unsteady Effect of Contoured Endwalls on Purge Flow and Secondary Flow System in an Axial Turbine. *21th International Symposium on Air Breathing Engines*, (ISABE-2013-1165), 2013.

[88] K. Reid, J. Denton, G. Pullam, E. Curtis, and J. Longley. The Effect of Stator-Rotor Hub Sealing Flow on the Mainstream Aerodynamics of a Turbine. *Proceedings of the ASME Turbo Expo*, (GT2006-90838), 2006.

[89] Rolls-Royce. *The Jet Engine*. Rolls-Royce plc, 2005.

[90] R. P. Roy, J. Feng, D. Narzary, and R. E. Paolillo. Experiment of Gas Ingestion Through Axial-Flow Turbine Rim Seals. *ASME Journal of Engineering for Gasturbines and Power*, 127:573–582, 2005.

[91] R. P. Roy, D. Zhou, S. Ganesan, C.-Z. Wang, R. E. Paolillo, and B. V. Johnson. The Flow Field and Main Gas Ingestion in a Rotor-Stator Cavity. *Proceedings of the ASME Turbo Expo*, (GT2007-27671), 2007.

[92] C. M. Sangan, O. J. Pountney, J. A. Scobie, M. Wilson, J. M. Owen, and G. D. Lock. Experimental Measurements of Ingestion Through Turbine Rim Seals - Part3: Single and Double Seals. *Proceedings of the ASME Turbo Expo*, (GT2012-68493), 2012.

[93] C. M. Sangan, O. J. Pountney, K. Zhou, M. Wilson, J. M. Owen, and G. D. Lock. Experimental Measurements of the Ingestion Trough Turbine Rim Seals - Part 2: Rotationally-Induced Ingress. *Proceedings of the ASME Turbo Expo*, (GT2011-45313), 2011.

[94] C. M. Sangan, K. Zhou, J. M. Owen, O. J. Pountney, M. Wilson, and G. D. Lock. Experimental Measurements of Ingestion Through Turbine Rim Seals - Part1: Externally-Induced Ingress. *Proceedings of the ASME Turbo Expo*, GT2011-45310, 2011.

[95] G. Schmid, S. Schrewe, and H.-P. Schiffer. Experimental and Numerical Investigation of the Interaction between Seal Air and Main Annuls Flow in a Two Stage Axial Turbine. *21th International Symposium on Air Breathing Engines*, (ISABE-2013-1166), 2013.

[96] S. Schrewe, C. Linker, A. Krichbaum, and H.-P. Schiffer. Measurements of Rim Seal Mixing Processes in an Axial Two Stage Turbine. *20th International Symposium on Air Breathing Engines*, (ISABE-2011-1720), 2011.

[97] S. Schrewe, H. Werschnik, and H.-P. Schiffer. Experimental Analysis of the Interaction between Rim Seal and Main Annulus Flow in a Low Pressure Two Stage Axial Turbine. *ASME Journal of Turbomachinery*, Vol. 135:051003–1–9, 2013.

[98] P. Schuepbach. *Influence of Rim Seal Purge Flow on the Performance of an End Wall Profiled Axial Turbine*. PhD thesis, ETH Zuerich, 2009.

[99] P. Schuepbach, R. S. Abhari, M. G. Rose, T. Germain, I. Raab, and J. Gier. Effects of Suction and Injection Purge-Flow on the Secondary Flow Structures of a High-Work Turbine. *ASME Journal of Turbomachinery*, Vol. 132:021021–8, 2010.

[100] P. Schuepbach, R. S. Abhari, M. G. Rose, and J. Gier. Influence of Rim Seal Purge Flow on the Performance of an Endwall-Profiled Axial Turbine. *ASME Journal of Turbomachinery*, Vol. 133:021011–10, 2011.

[101] P. Schuler, K. Dullenkopf, and H.-J. Bauer. Investigation of the Influence of Different Rim Seal Geometries in a Low Pressure Turbine. *Proceedings of the ASME Turbo Expo*, (GT2011-45682), 2011.

[102] P. Schuler, W. Kurz, K. Dullenkopf, and H.-J. Bauer. The Influence of Different Rim Seal Geometries on Hot-Gas Ingestion and Total Pressure Loss in a Low-Pressure Turbine. *Proceedings of the ASME Turbo Expo*, (GT2010-22205), 2010.

[103] C. H. Sieverding. Recent Progress in the Understanding of Basic Aspects of Secondary Flows in Turbine Blade Passages. *Proceedings of the ASME Turbo Expo*, (84-GT-78), 1984.

[104] A. Suryanarayanan, S. P. Mhetras, M. T. Schobeiri, and J. C. Han. Film-Cooling Effectiveness on a Rotating Blade Platform. *ASME Journal of Turbomachinery*, Vol. 131:011014–1–12, 2009.

[105] G. Thaler, K. Kuhn, and H. Jaberg. Sekundärströmung in Schaufel(ring)gittern mit Pfeilung and V-Stellung - eine Literaturstudie. *Forschung im Ingenieurwesen*, 65:236–246, 2000.

[106] K. Thole. *Airfoil Endwall Heat Transfer*. NETL - The Gas Turbine Handbook, 2006.

[107] C. Vaugham. *A Numerical Investigation into the Effect of an External Flow Field on the Sealing of a Rotor-Stator Cavity*. PhD thesis, University of Sussex, 1986.

[108] VDI. *VDI Wärmeatlas*. Springer, 2002.

[109] C.-Z. Wang, B. V. Johnson, S. P. Mathiyalagan, J. A. Glahn, and D. F. Cloud. Rim Seal Ingestion in a Turbine Stage from 360-Degree Time-Dependent Numerical Simulations. *Proceedings of the ASME Turbo Expo*, (GT2012-68193), 2012.

[110] H. P. Wang, S. J. Olson, R. J. Goldstein, and E. Eckert. Flow Visualisation in a Linear Turbine Cascade of High Performance Turbine Blades. *ASME Journal of Turbomachinery*, Vol. 119:1–8, 1997.

[111] J. Westerweel. Theoretical analysis of the measurement precision in particle image velocimetry. *Exp. Fluids*, Vol. 29:3–12, 2000.

[112] D. W. Zhou, R. P. Roy, C. Z. Wang, and J. A. Glahn. Main Gas Ingestion in a Turbine Stage for Three Rim Cavity Configurations. *ASME Journal of Turbomachinery*, Vol. 133:031023 –1–12, 2011.

[113] M. B. Zlatinov, C. S. Tan, M. Montgomery, T. Islam, and M. Seco-Soley. Turbine hub and shroud sealing flow loss mechanisms. *Proceedings of the ASME Turbo Expo*, (GT2011-46718), 2011.

A Appendix

A.1 Pictures of the Test Rig and the Measurement Equipment

A.1.1 The Large Scale Turbine Rig

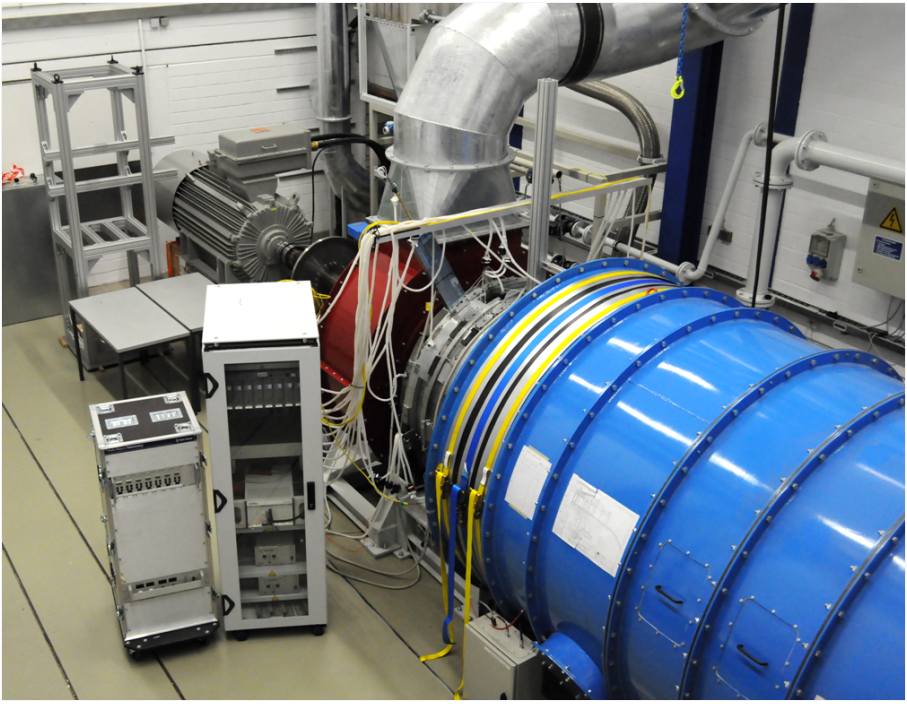

Figure A.1: *LSTR equipped with measurement system*

A.1.2 Probes and Traversing Units

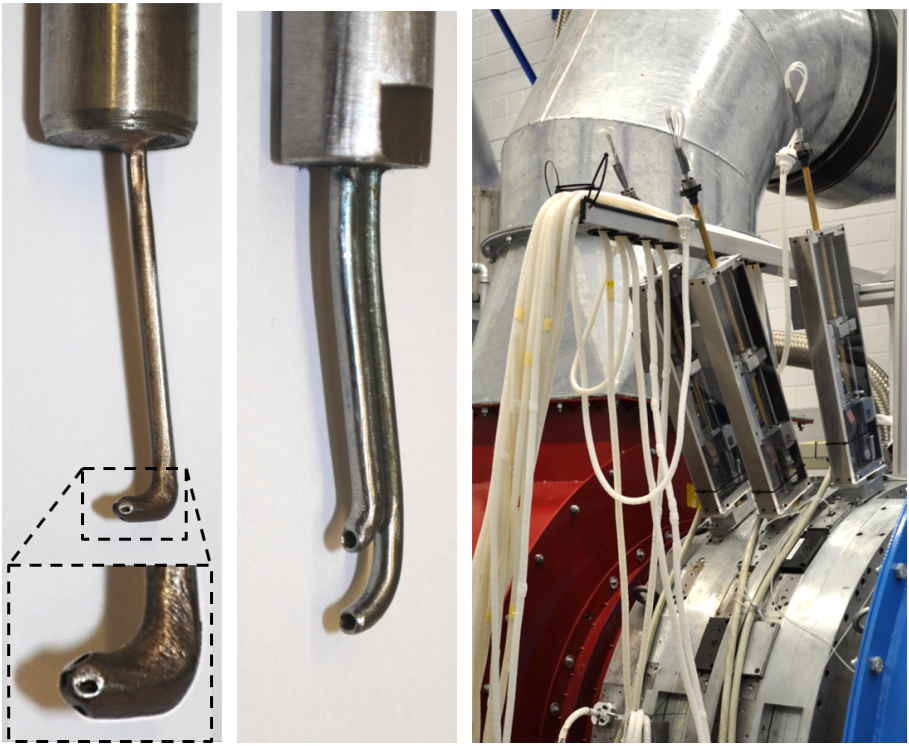

(a) Five-hole-probe *(b) CO_2 probe* *(c) Traversing units at the turbine casing*

Figure A.2: *Probes and traversing units used at the LSTR*

A.1.3 The PIV Measurement System

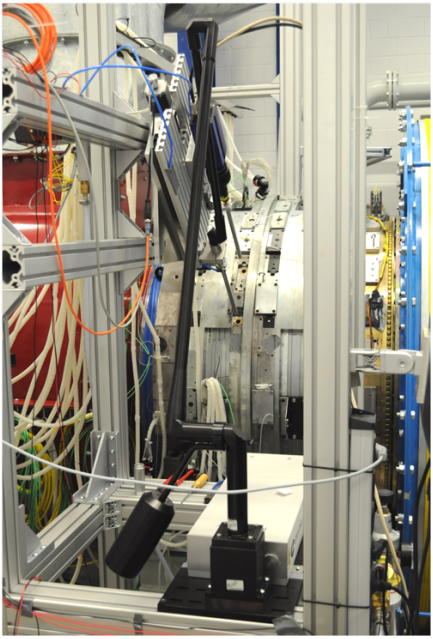

(a) *PIV measurement tower with laser*

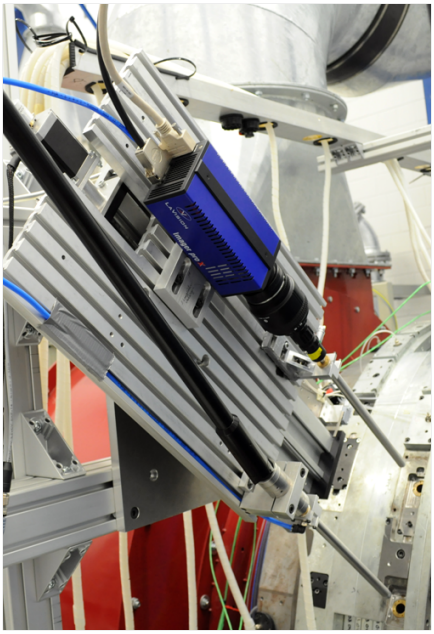

(b) *Camera, borescope, endoscope and purging devices mounted on grooved plate*

Figure A.3: *The PIV system assembled at the LSTR*

A.2 Results for Alternative Efficiency Definition

In this thesis two different efficiency definitions are proposed, whereas the one given in Equation 5.2 has been used to examine the influence of the purge flow injection on the turbine efficiency. The reason for the use of this rather simplified definition is that it omits the necessity to measure the total pressure in the rim seal region or wheelspace. However, if instead of this simplified definition the more straight forward Equation 5.4 is used, the total pressure within the cavity needs to be measured. However, due to a lack of total pressure probes in the wheelspace or rim seal, only the pressure measured at the stationary walls can be used. Figure A.4 shows on the left hand side the results for this approach.

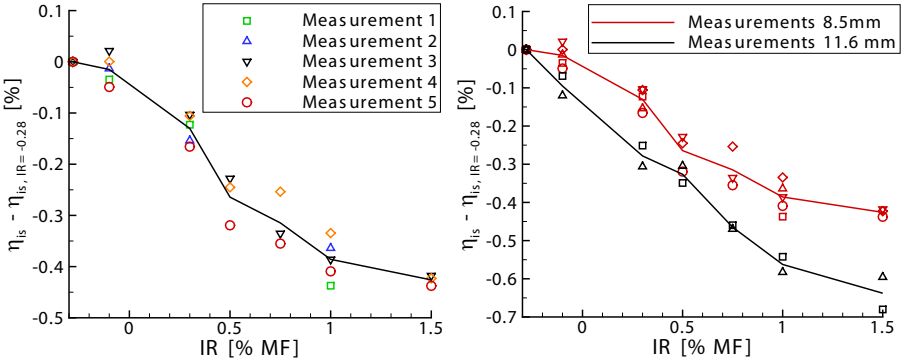

Figure A.4: *Results from efficiency measurements using the alternative efficiency definition*

In general the efficiency drop is about 0.1% reduced in comparison to the one assessed with Equation 5.2 in Chapter 6.1.1, whereas the major differences occurs only above an IR of 1%. The reason for this is that the static pressure decreases within the rim seal if the purge flow is increased, as it has been shown in Fig. 6.30. Nevertheless, the general tendency of a decreasing efficiency at increased pure flow rates stays the same. This is also valid for the comparison of the efficiency decrease at the two different drive arm hole diameters, whose results are presented on the right hand side of Fig. A.4. As already presented in Chapter 6.4, the enlarged drive arm holes feature an increased efficiency decrease. Thus it can be stated, that this result is not affected by the different efficiency definitions

A.3 Influence of Suction Rate on CO_2 Measurements

As described in Chapter 3.3.3, the adiabatic cooling effectiveness at the stator surface has been measured by the extraction of a small proportion of fluid through the static pressure taps. Using this technique there is the possibility that fluid further away from the wall is drawn into the measurement system. This would lead to the situation that the measured concentration is not representative of the one at the surface. This in turn would falsify the results. To assess this potential effect, measurements with a variation of the suction rate have been carried out at several locations at the stator surface. For this purpose the through-flow of the gas analyser has been adjusted by valves and rotameters to two different values, whereas the lower one equals approx. $3l/h$ and is the smallest one that can be adjusted. The higher flow rate equals approx. $10l/h$, which is still far below the maximum gas analyser flow rate of $60l/h$. Results from these two through-flow rates are presented in Fig. A.5 at the stator platform and at the suction side profile of the vane.

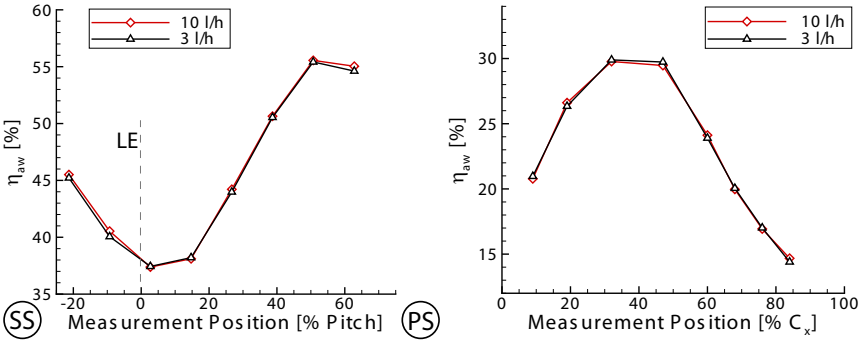

(a) 4%C_x *upstream of the LE* *(b) 5% channel height at stator 2 SS*

Figure A.5: *Adiabatic cooling effectiveness at different gas-analyser throughflows; IR = 1,0%*

Examining these results it gets clear that there are almost no differences between the two suction rates. Only a few points show minor differences, which are however within the measurement uncertainty of the system. Thus, it can be concluded that the obtained results are not affected by the used suction rate and that no fluid further away from the surface is fed into the gas analyser. Also, it seems adequate to use the higher of the tested suction rates to reduce measurement time and CO_2

consumption. This has been done, also because the gas analyser offers in addition a better accuracy for this through-flow according to the manufacturer.

Curriculum Vitae

Sebastian Schrewe

Date of birth	02. November 1982
Place of birth	Henstedt - Ulzburg

Work Experience:

Since 2013	Specialist Fluidsystems at Rolls-Royce Deutschland Ltd & Co KG
2008 - 2013	Research Assistant at the Institude of Gasturbines and Aerospace Propulsion at Technische Universität Darmstadt

University:

2002 - 2008	Studying Mechanical Engineering at Technische Universität Darmstadt
2005 - 2006	Studying at Nanyang Technological University in Singapore

School:

1993 - 2002	Abitur at Schwalmschule in Schwalmstadt
1989 - 1993	Primary school in Schwalmstadt